School of Physics and Astronomy
Queen Mary University of London

A Vlasov-Hybrid Code with Hermite Expansion of the Distribution Function for the Study of Low Growth Rate Instabilities

Francesco Boffa

2018

Submitted in partial fulfillment of the requirements of the Degree of Doctor of Philosophy

Declaration

I, Francesco Boffa, confirm that the research included within this thesis is my own work or that where it has been carried out in collaboration with, or supported by others, that this is duly acknowledged below and my contribution indicated. Previously published material is also acknowledged below.

I attest that I have exercised reasonable care to ensure that the work is original, and does not to the best of my knowledge break any UK law, infringe any third partys copyright or other Intellectual Property Right, or contain any confidential material.

I accept that the College has the right to use plagiarism detection software to check the electronic version of the thesis.

I confirm that this thesis has not been previously submitted for the award of a degree by this or any other university.

The copyright of this thesis rests with the author and no quotation from it or information derived from it may be published without the prior written consent of the author.

The work in this thesis resulted from collaborations with David Burgess and Enrico Camporeale.

The material presented in Chapter 4 and Chapter 5 have been submitted to the Journal of Computational Physics.

Francesco Boffa
Date: 21/05/2018

Abstract

Within turbulence there are many phenomena which are currently unsolved. In the solar wind temperature anisotropies and low growth rates instability have a dominant role in defining the turbulent behaviour of plasma. Due to the non linearity of the equations involved in the description of the physics of plasmas numerical simulations are a fundamental tool to study the dynamics of turbulent phenomena. In particular, hybrid codes are widely used in space plasma applications due to their ability to simulate large regions of volume maintaining some kinetic effects.

However, due to the sensitivity to the initial level of noise in the simulation, low growth rate instabilities are particularly difficult to simulate. Particle in Cell-hybrid simulations require too many particles to reduce the initial noise, while Vlasov-hybrid simulations require too many grid points to fully discretize spatial and velocity phase spaces.

We present here a Vlasov-hybrid algorithm and code implementation where the distribution function is expanded in series of Hermite functions. Thanks to the properties of these it is possible to project the Vlasov equation to find an equation for each coefficient of the expansion. These coefficients are advanced in time using a *Current Advance Method* algorithm with splitting method for the Vlasov operator. The former is treated explicitly, while the latter is treated implicitly with a *GMRES* solver. The current is advanced with a temporal ODE derived taking moments of the Vlasov equation. A 1D3V code is implemented, tested and used to study low growth rate instabilities such as a proton cyclotron instability and a ion/ion right hand resonant instability with small relative velocity drift between beam and core populations. The results are compared with existing hybrid algorithms that we implemented. A 2D3V parallelized version of the code is implemented and described here. Initial results are presented and future improvements are discussed.

Acknowledgements

First, I would really like to sincerely thank my supervisor Prof. David Burgess for being a guide through my Ph.D.. I would like to thank him for all the suggestions and the teachings he provided me during these years. Also, I would like to thank him for his patience and for always believing in me. This really helped me and pushed me going forward.

I want to thank my family who has always been supportive for me during all my studies. Magda and Roberto, my mum and dad, made possible for me to study and reach this point, helping me even when the times were hard for our family. I will never stop being thankful to them.

I want to thank all my friends who I made since I moved to London who always admired me for my studies and always tried to motivate me to do the best.

Finally I would like to thank my wonderful girlfriend Gintare, who has been close to me in the last year and a half. I want to thank her for making me happy every day also in hard moments. Her support and motivation has been fundamental for me.

This work was supported by a studentship funded by Queen Mary University of London.

Contents

List of Figures

List of Tables

1 Introduction

Plasma is the fourth state of matter after solid, liquid and gas. In particular a plasma is an ionized gas where the charges, in the form of electrons and ions, move carrying currents, therefore generating magnetic fields. Ionization can happen, for example, in conditions of very high temperatures or due to photo-dissociation. Due to their charge the particles in the plasma are subjected to electric and magnetic forces. Since they are charged, they generate electric and magnetic fields while moving, which interact with other particles influencing their movement. For this reason plasmas can show very complex and interesting behaviour.

It is often said that plasma is the most abundant state of matter in the universe. This is certainly the case if one considers that all the interstellar space is filled with plasma. Interest in planetary plasma started from the second half of the twentieth century, with the start of the space age. In 1958 Parker proposed that the hot corona produces a supersonic outflow of plasma called the solar wind [Parker, 1958]. From 1959 with the launch of the Soviet Union's Luna-1 probe there were the first satellite observations and measurements of the solar wind. Starting from 1960 we had another set of observations [Behannon and Ness, 1966, Mihalov et al., 1968, Ness, 1965, 1969] which allowed astrophysicists to describe the solar wind flowing past the Earth and stretching the magnetic field behind it forming a tail in the magnetosphere. An extremely simplified idea of the solar wind and its interaction with the Earth's magnetosphere is given in Fig. 1.1

In this introductory chapter we first describe the solar wind, then we introduce the different models for studying plasmas both theoretically and numerically. We then briefly review linear Vlasov theory for the study of plasma microinstabilities. Finally, we present the outline of this thesis, showing the motivations behind this work.

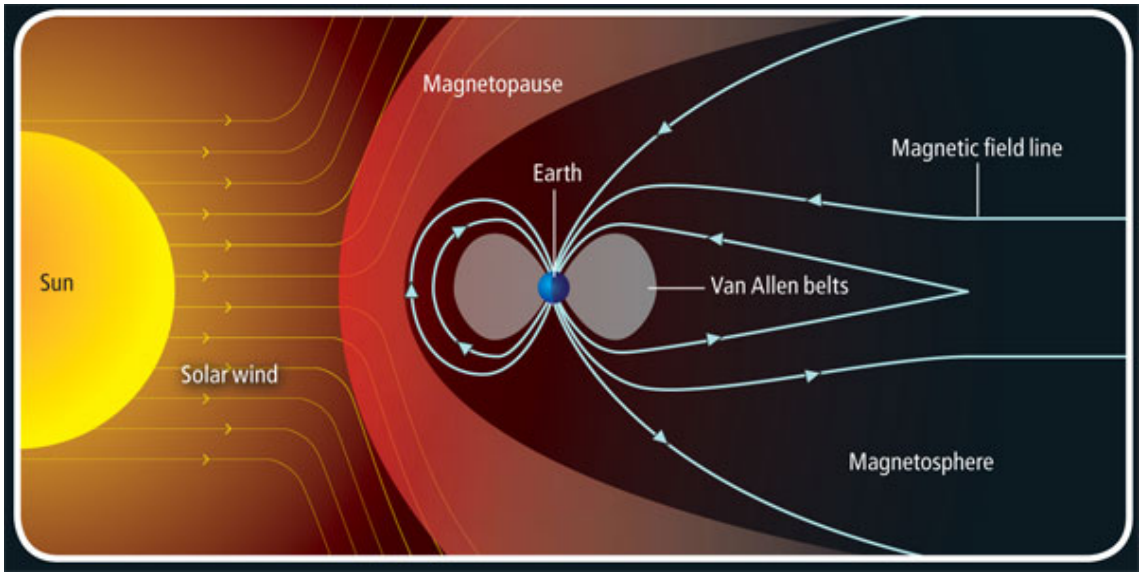

Figure 1.1: Schematic view of the solar wind and Earth's magnetosphere. The solar wind flows out of the Sun towards the Earth (and other planets). Encountering the magnetic field generated by the body, the solar wind is deviated around it. Source *https://watchers.news/data/uploads/2013/03/magneto.jpg*

1.1 The Solar Wind

The solar wind was introduced theoretically before its first direct observation. Biermann [1951] suggested that gas was streaming out from the Sun in all the directions with velocities ranging between 500 and 1500 km/sec. Parker [1958] confirmed that the plasma is continuously flowing from the Sun driven to supersonic speeds by the high coronal temperature.

Parker used the equations of hydrodynamics to derive the solar wind equation, assuming a specific temperature distribution in order to generate an expanding solution. The model contemplates the presence of a heat source, but it doesn't explain its details, leaving the coronal heat transport equation unsolved. Parker shows how the solar wind flow becomes supersonic.

Parker modified the Magnetohydrodynamics equations [Parks, 2003] to include thermal contribution and simplified them considering a star without magnetic field and viscosity. From conservation of momentum:

$$dp = -\rho_m v dv - \rho_m \frac{M_\odot G}{r^2} dr, \tag{1.1}$$

where r is the radius from the center of the Sun, G is the universal gravitational constant (Newton's constant), $M_\odot$ is the mass of the Sun, ρ_m is the mass density, v

is the flow velocity and p is the scalar pressure. The acceleration due to solar gravity is expressed by $g_\odot = \frac{M_\odot G}{r^2}$. Considering a fluid in thermodynamic equilibrium, its pressure is:

$$p = p_e + p_i = 2nkT, \tag{1.2}$$

where subscripts refer to electrons and ions, $n = n_i = n_e$ is the number density in particles per volume unit, k is the Boltzmann constant ($k \approx 1.38065 \times 10^{-23} JK^{-1}$) and T is the temperature. The sound speed C_s is given by:

$$C_s^2 = \frac{dp}{d\rho_m} = \frac{dp}{d\left(nm\right)} \approx \frac{2kT}{m_i}, \tag{1.3}$$

where m_i is the ions mass. Since for a plasma with electrons and one ion species

$$\rho_m = m_i n_i + m_e n_e \approx n m_i, \tag{1.4}$$

where m_e is the electrons mass. Using the continuity equation in spherical coordinates $r^2 nv = const$ and the equation for the pressure to eliminate n in Eq.(1.1) we obtain:

$$\left(\frac{mv^2}{2kT} - 1\right)\frac{dv}{dr} = -\frac{vr^2}{T}\frac{d}{dr}\left(\frac{T}{r^2}\right) - \frac{GM_\odot mv}{2kTr^2} \tag{1.5}$$

Assuming that we are solving an isothermal problem, i.e. T is constant varying r, we obtain Parker's solar wind equation:

$$\left(v - \frac{C_s^2}{v}\right)\frac{dv}{dr} = \frac{2C_s^2}{r} - \frac{GM_\odot}{r^2}. \tag{1.6}$$

The assumption of constant temperature does not affect the demonstration that the solar wind flow becomes supersonic. Defining r_c, critical radius, as radius where the solar wind velocity v is equal to the sound speed C_s we have:

$$r_c = \frac{GM_\odot}{2C_s^2}, \tag{1.7}$$

which can be used to rewrite the previous equation as:

$$\left(v - \frac{C_s^2}{v}\right)\frac{dv}{dr} = \frac{2C_s^2}{r^2}\left(r - r_c\right). \tag{1.8}$$

This equation can be solved using different boundary conditions. The solutions to this equation are shown in Fig 1.2. Parker suggested as solution to the solar wind equation the grey line. In fact Eq.(1.8) has four different classes of solution:

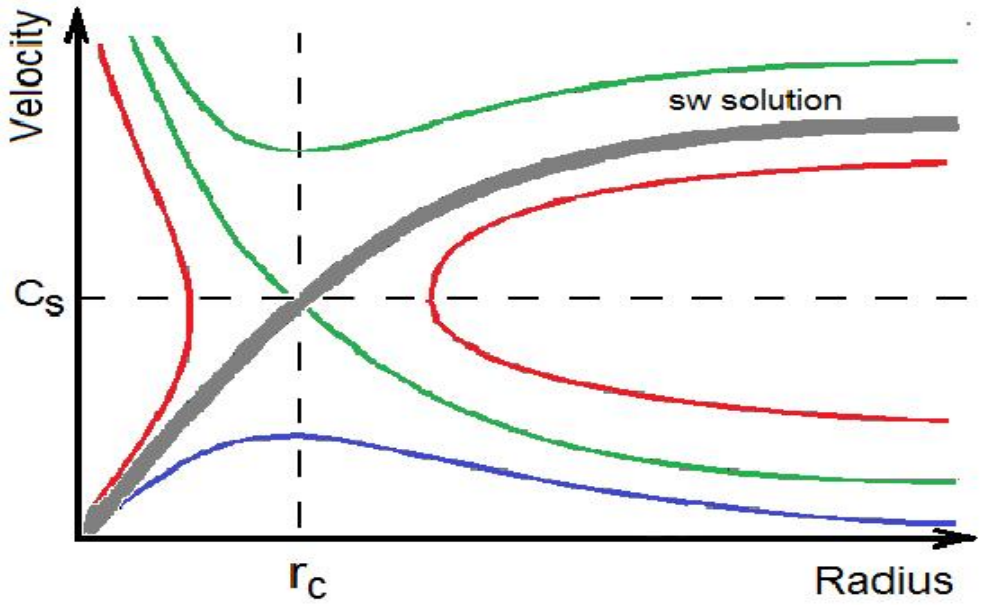

Figure 1.2: Solutions of Parker's solar wind equation with different boundary conditions. The graph gives the solar wind speed as function of the distance from the center of the Sun. The solution matching the physical boundary conditions is given by the grey line. Picture courtesy of Christopher Thomas Haynes.

- the first class of solutions has a subsonic velocity in all the domain; v increases in the first part of the expansion, until reaching a maximum value in proximity of the critical radius and then starts decreasing (blue line in the figure);
- the second class contains a unique solution with monotonically increasing velocity and $v(r_c) = C_s$. This is the solution suggested by Parker (grey line);
- the third class contains a unique solution with monotonically decreasing velocity and $v(r_c) = C_s$ (lower green line);
- the fourth class of solutions has a supersonic velocity in all the domain; v decreases in the first part of the expansion, until it reaches a minimum value in proximity of the critical radius and then it starts increasing (upper green line);

The red lines delimit the region where the solutions exist. Each class is found combining different boundary conditions for $r = r_\odot$ and $r \to \infty$. The third and fourth classes can be excluded from the possible solutions as they require a supersonic flow velocity at the base of the solar corona which is not observed. Conversely the first and second classes predict a subsonic flow velocity at $r = r_\odot$ so they are acceptable.

However the behaviour is very different for $r \to \infty$. Simple considerations on the pressure levels at $r \to \infty$ yield to a finite value $p_\infty = \frac{2\rho_\infty T}{m_p}$, with ρ_∞ finite mass density, which does not match the smaller physical value. Conversely, $p \to 0$ is obtained for the second class which matches the observed very small interstellar pressure.

The class 2 solution is the only one which matches the physical boundary conditions. It predicts the expansion of the solar corona radially outward at subsonic velocities in the region of space close to the Sun, reaching the sound speed at the critical radius and accelerating to supersonic values moving far away from the Sun. Parker named the continuous coronal flow the solar wind.

The Ulysses Spacecraft [Bame et al., 1992, Marsden and Smith, 1997, Mccomas et al., 2001] was launched in 1990 as a union of forces between NASA and ESA. It accomplished three fast latitude scans of the Sun in 1994/1995, 2000/2001, and 2007/2008 flying by Jupiter in 1992 [Tsurutani, 1992] probing its magnetosphere. In Fig. 1.3 we can see the third orbit made by the spacecraft, with Earth's and

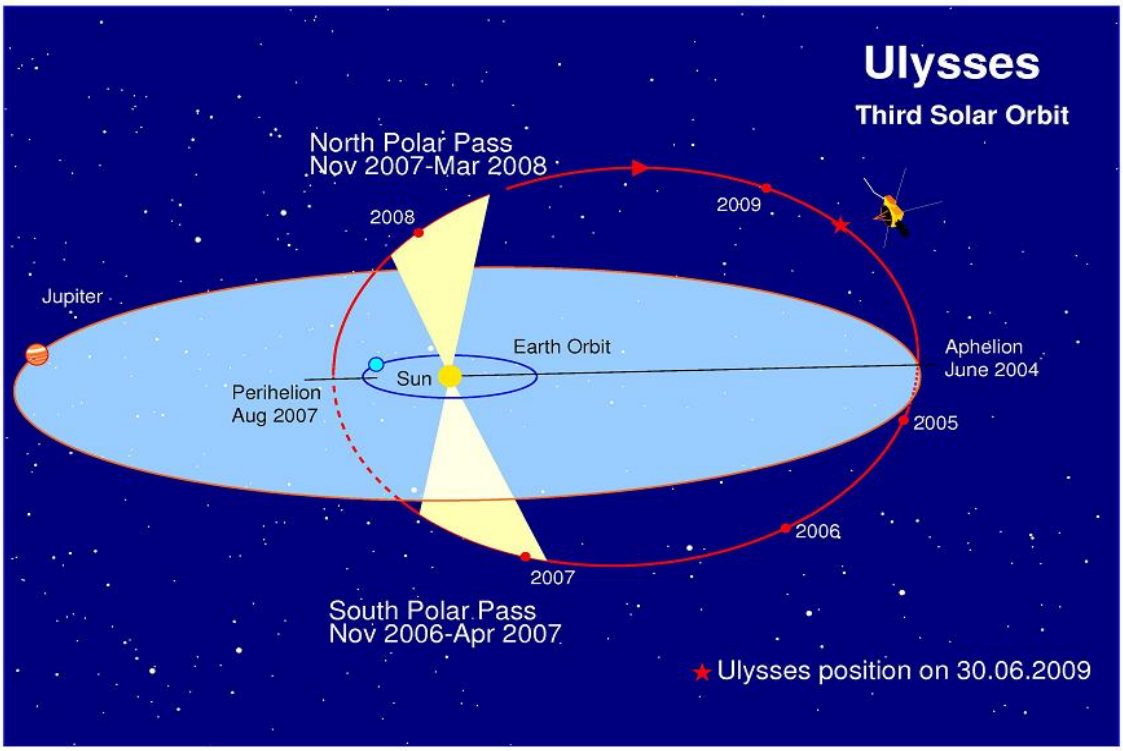

Figure 1.3: Ulysses third orbit. The figure shows the spacecraft's orbit plus the Earth's and Jupiter's ones, around the Sun.
Source: *https://www. cosmos.esa.int/web/ulysses/third-orbit.*

Jupiter's orbits included in the scheme.

Ulysses data confirmed that the solar wind is not uniform. It's speed changes depending on latitude and time. In particular there is a distinction between fast

and slow solar wind. The former has typical speeds of $750-800$ km/h and is situated over coronal holes, region at low energy density in the solar corona, the latter has speed of $300-350 km/h$ and is found above streamers, magnetic loops which connect regions at opposite magnetic polarity. In Fig. 1.4 we can see the average solar wind speed as a function of the polar coordinate. Here measurements come from Ulysses

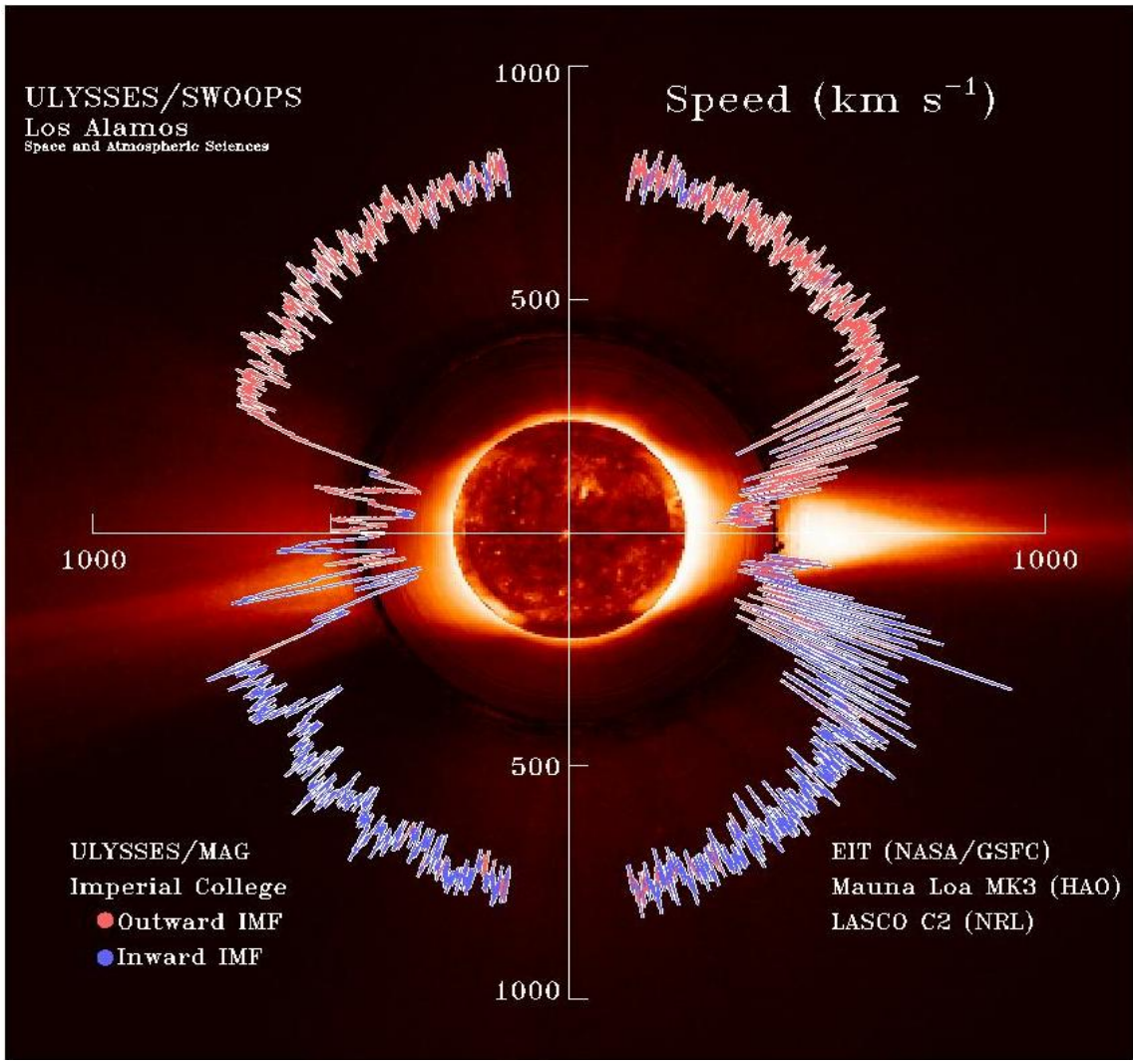

Figure 1.4: Average solar wind speed, in kms^{-1} as function of latitude in polar coordinate system centred on the Sun's centre. It is possible to see regions at slow and regions at fast solar wind. Measures from Ulysses and SOHO. Source: *http://sci.esa.int/ulysses/12399-swoops-solar-wind-speed-data/.*

and from SOHO, the Solar and Heliospheric Observatory a satellite launched in 1995 by NASA and ESA. The former is positioned in the first of the Lagrange points, L1.

Another satellite in vicinity of L1 is the Advanced Composition Explorer (ACE), launched by NASA in 1997 [McComas et al., 1998]. Real time solar wind data from

ACE are available from Caltech website. An example is shown in Fig. 1.5

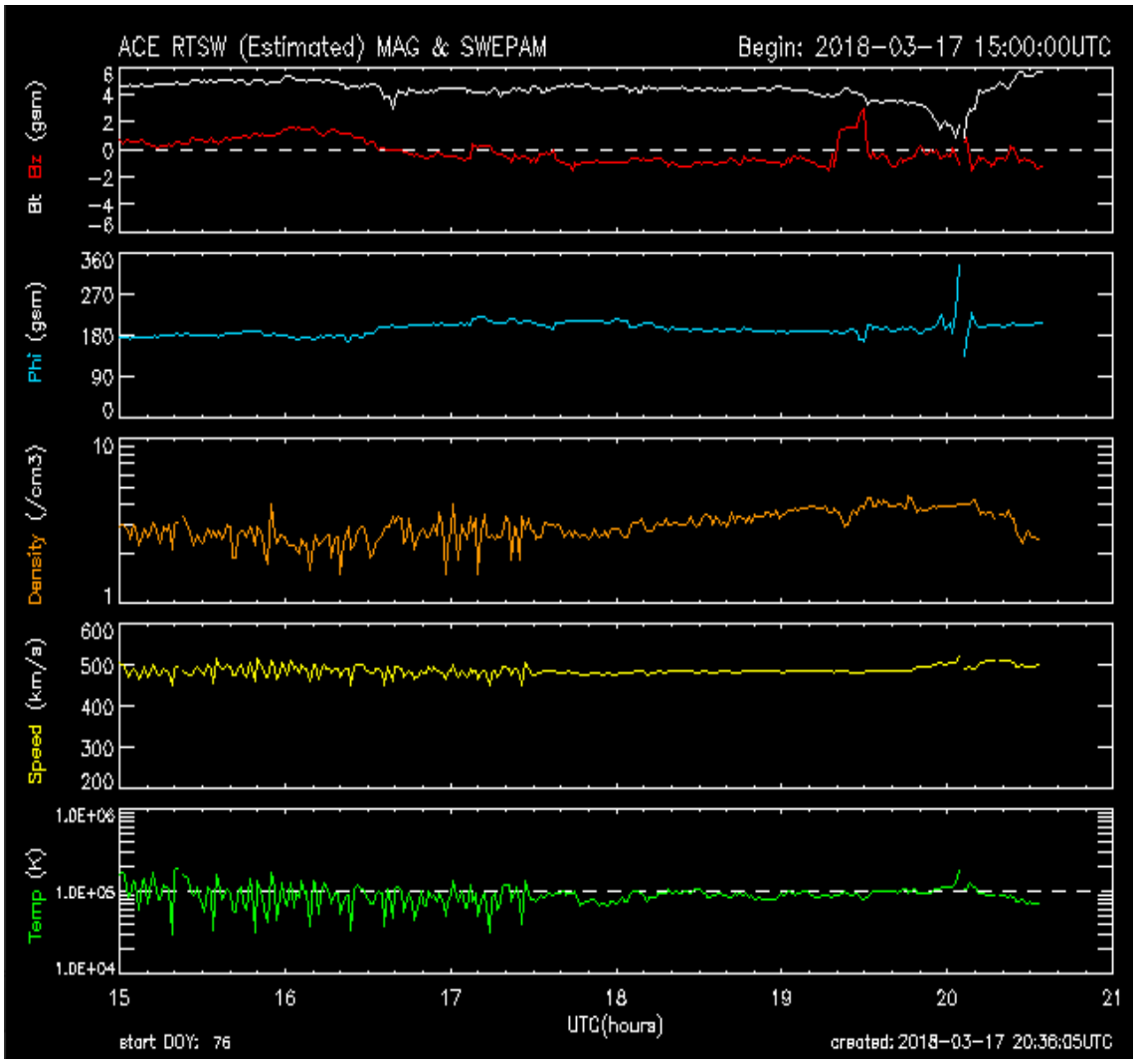

Figure 1.5: Solar wind real time data from the Advanced Composition Explorer. On the horizontal ax we have the time, in hours, between 3.00 PM and 9.00 PM UTC of the 17th March 2018. On the 5 vertical axes we have in order: magnetic field, total (white line) and along z (red line) in the geocentric solar magnetospheric system of coordinates in nT; angle of the interplanetary magnetic field that is being carried out by the solar wind, in the gsm system; solar wind number density in cm^{-3}, solar wind speed in km/s and Temperature in K. Source: *https://www.swpc.noaa.gov/products/ace-real-time-solar-wind*.

The solar wind streaming out of the Sun convects out the Interplanetary Magnetic Field. The IMF was postulated by Hale [1908] who used the Zeeman effect and the spectroheliograph he invented to show that sunspots were magnetic features. The first in situ observations arrived in 1960 with the launch of Pioneer V [Coleman

et al., 1960] sufficiently far from the Earth so that the planet's magnetic field would not interact in the observations [Ness and Burlaga, 2001]. The IMF existence is due to the expansion of the solar corona and can be explained within MHD theory.

We will first obtain the equation for the solar wind flow velocity then use it to describe the interplanetary magnetic field. We set two frames of reference with center O, at the center of the Sun and O', corotating with the Sun, at r_c, where the radial flow begins. We consider the fluid at $\boldsymbol{r} < \boldsymbol{r}_c$ part of the Sun atmosphere, therefore corotating with the Sun . The velocities in the different frames of reference are related by:

$$\boldsymbol{v} = \boldsymbol{v}' + \boldsymbol{\Omega} \times \boldsymbol{r}', \tag{1.9}$$

where Ω is the Sun's angular velocity and $\boldsymbol{r}' = \Omega(\boldsymbol{r} - \boldsymbol{r}_c)$. The components of the flow velocity in spherical coordinates are:

$$v_r = v_{r'} = v_{sw} \tag{1.10}$$

$$v_\theta = v_{\theta'} = 0 \tag{1.11}$$

$$v_\phi = v_{\phi'} + \Omega\,(r - r_c) = \Omega\,(r - r_c)\,, \tag{1.12}$$

where θ and ϕ are polar and azimuthal directions respectively. To obtain the equation which models the streamlines we impose $d\boldsymbol{l} \times \boldsymbol{v} = 0$; this implies in fact that the velocity is tangent to $\boldsymbol{l}$, therefore defining $\boldsymbol{l}$ as streamline:

$$\frac{dr}{v_r} = \frac{r d\theta}{v_\theta} = \frac{r \sin\theta d\phi}{v_\phi}, \tag{1.13}$$

which, considering the flow confined to the ecliptic plane, after integration gives:

$$\frac{r}{r_c} - 1 - ln\frac{r}{r_c} = \frac{v_{sw}}{\Omega r_c}\,(\phi - \phi_0)\,, \tag{1.14}$$

which models the solar wind velocity at any r and azimuthal angle, ϕ, given the angular rotation of the Sun.

Since the solar wind is a good conductor we assume the validity of the Alfvèn's frozen-in-field theorem, i.e. for a fluid with infinite electric conductivity the magnetic field ($\boldsymbol{B}$) lines move along with the fluid. Therefore we obtain the equation for the interplanetary magnetic field tangent to the streamlines imposing $d\boldsymbol{l} \times \boldsymbol{B} = 0$:

$$\frac{dr}{B_r} = \frac{r d\theta}{B_\theta} = \frac{r \sin\theta d\phi}{B_\phi}. \tag{1.15}$$

Imposing $B_\theta = 0$ and comparing with the equation for the streamlines we obtain a relation between flow velocity and magnetic field:

$$\frac{v_r}{v_\phi} = \frac{B_r}{B_\phi}. \tag{1.16}$$

From Gauss theorem in spherical coordinates:

$$\frac{1}{r^2}\frac{\partial}{\partial r}\left(r^2 B_r\right) + \frac{1}{r sin\theta}\frac{\partial}{\partial \theta}B_\theta + \frac{1}{r\sin\theta}\frac{\partial}{\partial \phi}B_\phi = 0 \tag{1.17}$$

we impose $B_\theta = 0$ and require axial symmetry, i.e. $\frac{\partial}{\partial \phi}B_\phi = 0$, to obtain:

$$\frac{1}{r^2}\frac{\partial}{\partial r}\left(r^2 B_r\right) = 0, \tag{1.18}$$

which has solution:

$$B_r\left(r\right) = B_r\left(r_c\right)\frac{r_c^2}{r^2}. \tag{1.19}$$

Substituting in Eq.(1.16) and making use of the equations for the velocity components we obtain:

$$B_\phi\left(r\right) = B_r\left(r_c\right)\frac{r_c^2}{r^2}\frac{\Omega\left(r - r_c\right)}{v_{sw}}, \tag{1.20}$$

valid only in the ecliptic plane. The radius is given by the streamlines equation. For $r < r_c$ the magnetic field has only radial component as we initially imposed, while for $r > r_c$ the transverse component forms spirals.

This magnetic field can be directed towards or away from the Sun. To give an idea of its configuration we show in Fig. 1.6 the IMF on the 30th December 2014 to 2 AU. We can see that the direction alternates between towards the Sun (blue lines) and away from the Sun (red lines).

This model doesn't include a magnetic field component perpendicular to the ecliptic plane. However this has been observed, with a small value of ≈ 1 nT at 1 AU. This component, B_z, is said to be northward when positive in value and southward when negative.

1.2 Plasma models

In the first paragraph of this chapter we mentioned that plasmas have very complicated behaviour due to self consistent electric and magnetic fields. A plasma model is a set of equations which describes the temporal evolution of a plasma, with known boundary and initial conditions [Schindler, 2006]. There are several plasma

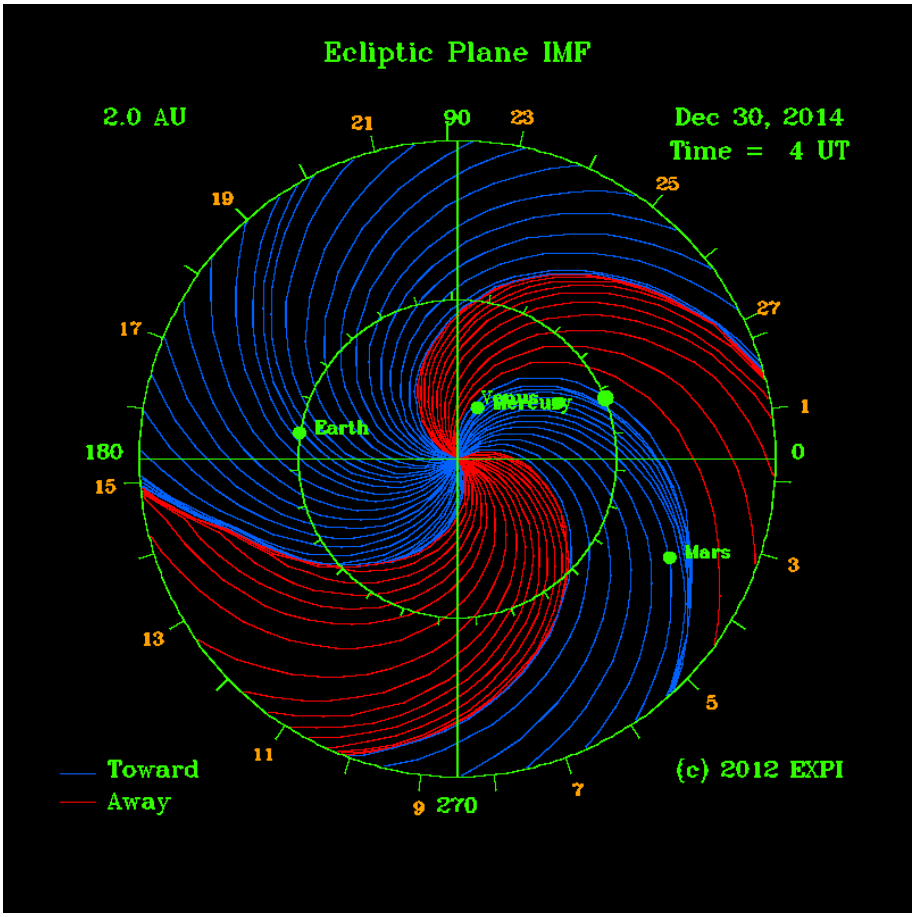

Figure 1.6: Interplanetary magnetic field in the ecliptic plane on 30th December 2014 to 2 AU. Red lines represent directions away from the Sun; blue lines represent directions toward the Sun. Source *www.expi.com*

models and they make use of different levels of approximation so they are suitable for different ranges of application.

For space plasmas it is reasonable to neglect quantum effects. In fact the typical values of action as momentum, time, length or energy are much larger than the Planck constant ($h = 6.63 \cdot 10^{-34} \mathrm{m^2 kg/s}$). Here we will discuss only plasma models which make use of classical or statistical mechanics and electromagnetism. Reactions between particles and radiations are not taken into account. In most astrophysical plasmas the speed of the particles is much smaller than the light speed. Particles moving at relativistic velocities can be found in the Van Allen Radiation Belts which we will not examine in this document. For this reason we will consider the particles in the non-relativistic limit.

In the following paragraphs we will fist show the simple single particle motion which involves the motion of one particle in an external non self consistent electro-

magnetic field. Then we will show self consistent kinetic and fluid models, followed by a discussion of consevation laws and their implications.

In the following paragraphs we will first show the simple single particle motion which involves the motion of one particle in an external non self consistent electromagnetic field. Then we will show self consistent kinetic and fluid models, followed by a discussion of conservation laws and their implications.

1.2.1 Single particle motion

In a plasma the charged particles move in electromagnetic fields. If the electric field, $\boldsymbol{E}(\boldsymbol{x},t)$, and the magnetic field,$\boldsymbol{B}(\boldsymbol{x},t)$, are known it is possible to describe the motion of a charged particle in the non-relativistic limit with the equation of motion:

$$m\frac{d\boldsymbol{v}}{dt} = q\left(\boldsymbol{E}\left(\boldsymbol{x},t\right) + \boldsymbol{v}\times\boldsymbol{B}\left(\boldsymbol{x},t\right)\right) - \nabla\psi\left(\boldsymbol{x}\right), \tag{1.21}$$

where $\boldsymbol{v}$ is the velocity given by:

$$\frac{d\boldsymbol{x}}{dt} = \boldsymbol{v}, \tag{1.22}$$

m and q are the particle's mass and charge and ψ represents the total conservative vector fields. For the purpose of this document, we will neglect this last term on the RHS of Eq.(1.21). This set of typically coupled ordinary differential equations can be solved to give the position and velocity at any time of a single particle moving in a prescribed electromagnetic field given certain initial conditions.

From the equation of motion, taking the dot product with the velocity, it is possible to obtain an equation for the energy:

$$\frac{d}{dt}\left(\frac{1}{2}mv^2\right) = q\boldsymbol{v}\cdot\boldsymbol{E} - m\boldsymbol{v}\cdot\nabla\psi. \tag{1.23}$$

We can see that the magnetic force in the Lorentz force does not contribute to change the kinetic energy. In fact the force acts in the direction perpendicular to the velocity, contributing in the change of trajectory of the particles, giving rise to a centripetal acceleration. This is the basis for one of the most important properties of particle motion: gyration.

Suppose that a particle is moving in a uniform constant magnetic field, with no electric field and no other forces applied. If the particle starts from zero velocity in the direction parallel to the magnetic field, then it starts moving on a circle perpendicular to the magnetic filed, while if it has an initial velocity it moves along

a helix. The centre of gyration is called gyrocentre. In this case the latter moves with constant velocity equal to the initial velocity of the particle. The radius of the helix is called gyroradius and is given by:

$$r_g = \frac{mv_\perp}{|q|B} \tag{1.24}$$

while

$$\omega_g = \frac{|q|B}{m} \tag{1.25}$$

is the gyrofrequency. The sense of rotation comes from the Lorentz force. This can be easily derived writing Lorentz force in the three components and solving two coupled ordinary differential equations, the solution of which gives a circular motion at ω_g.

In the presence of other fields and forces or for a varying magnetic field the particle moves in more complex ways. For slowly varying fields the particle preserves the gyromotion. However the gyrocenter starts drifting due to a series of different effects. In this case the particle has an adiabatic motion.

The simplest case of drift is due to the presence of a constant $\boldsymbol{E}$ perpendicular to $\boldsymbol{B}$. This gives rise to a drift of the gyrocenter with a velocity:

$$\boldsymbol{v}_E = \frac{\boldsymbol{E} \times \boldsymbol{B}}{B^2}. \tag{1.26}$$

The total particle motion corresponds to gyration in a frame of reference which moves at $\boldsymbol{v}_E$. Variations in electromagnetic fields in both time and space can lead to a set of other drifts of the gyrocenter. In particular drifts can be caused by external forces, electric field (as we mentioned), spatial variations in the electric field, spatial variations in the magnetic field (grad-B drift and curvature drift), temporal variation of the fields (polarization drift). It is possible to find the total velocity drift to zeroth and first order in $\frac{\omega}{\omega_g}$, where ω defines the frequency of the variations on the fields, as:

$$\boldsymbol{v}_d = v_\parallel \boldsymbol{b} + \boldsymbol{v}_E + \frac{\mu}{qB^2}\boldsymbol{B} \times \nabla B + \frac{m}{qB^2}\boldsymbol{B} \times \left(v_\parallel \frac{d\boldsymbol{b}}{dt} + \frac{d\boldsymbol{v}_E}{dt} + \nabla\psi \right), \tag{1.27}$$

where $\boldsymbol{b}$ is the unit vector of the magnetic field and the parallel drift velocity satisfies:

$$m\frac{dv_\parallel}{dt} = qE_\parallel - \boldsymbol{b} \cdot \nabla B + m\boldsymbol{v}_E \cdot \frac{d\boldsymbol{b}}{dt} - m\boldsymbol{b} \cdot \nabla\psi. \tag{1.28}$$

We introduce the magnetic moment:

$$\mu = \frac{\frac{1}{2}mv_{\perp}^2}{B}. \tag{1.29}$$

The latter is the first adiabatic invariant of particle motion. This means that the magnetic moment stays approximately constant when the system changes slowly. The second adiabatic invariant, I, is associated with particles trapped between regions where the magnetic field is strong:

$$I = \oint v_{\parallel} ds. \tag{1.30}$$

This quantity stays constant when the integration is performed along the field line between the points of mirroring. For completeness we give the Hamiltonian formulation of single particle motion. Using electric potential $\phi(\boldsymbol{x}, t)$ and magnetic vector potential $\boldsymbol{A}(\boldsymbol{x}, t)$, related to the fields with:

$$\boldsymbol{E} = -\nabla\phi - \frac{\partial \boldsymbol{A}}{\partial t} \tag{1.31}$$

$$\boldsymbol{B} = \nabla \times \boldsymbol{A}, \tag{1.32}$$

we can find the Hamiltonian as:

$$H(\boldsymbol{P}, \boldsymbol{x}) = \frac{1}{2m}\left(\boldsymbol{P} - q\boldsymbol{A}(\boldsymbol{x}, t)\right)^2 + q\phi(\boldsymbol{x}, t), \tag{1.33}$$

where the equations of motion are the Hamilton's equation:

$$\frac{d\boldsymbol{x}}{dt} = \frac{\partial H}{\partial \boldsymbol{P}} \tag{1.34}$$

$$\frac{d\boldsymbol{P}}{dt} = -\frac{\partial H}{\partial \boldsymbol{r}} \tag{1.35}$$

Here $\boldsymbol{P} = m\boldsymbol{v} + q\boldsymbol{A}$ is the canonical momentum [Schindler, 2006].

1.2.2 Kinetic models

In kinetic theory a plasma is represented by a large number of charged particles in constant motion. To describe these particles we introduce a fundamental quantity: the particle distribution function. The latter is a function of the 6-dimensional phase space and time. It is possible to define it as function of space and momentum,

$F_s(\boldsymbol{x}, \boldsymbol{P}, t)$, or of space and velocity, $f_s(\boldsymbol{x}, \boldsymbol{v}, t)$, where the subscript s identifies a plasma species. Given an infinitesimal volume in the phase space we use the distribution function to obtain the infinitesimal number of particles in that volume, i.e.:

$$dN_p(t) = F_s(\boldsymbol{x}, \boldsymbol{P}, t)\, d\boldsymbol{x} d\boldsymbol{P} \tag{1.36}$$

$$dN_p(t) = f_s(\boldsymbol{x}, \boldsymbol{v}, t)\, d\boldsymbol{x} d\boldsymbol{v} \tag{1.37}$$

To study the kinetic behaviour of plasmas we follow the evolution of the distribution function using a transport equation, coupled with Maxwell's equations. A plasma is formed by different species, generally at least one electron and one ion species. The Hamilton's equations described in the previous paragraph imply an equation for the distribution function $F_s(\boldsymbol{x}, \boldsymbol{P}, t)$ for the species s in the 6 dimensional phase space $(\boldsymbol{x}, \boldsymbol{P})$:

$$\frac{\partial F_s}{\partial t} + \frac{\partial F_s}{\partial \boldsymbol{x}} \cdot \frac{\partial H_s}{\partial \boldsymbol{P}} - \frac{\partial F_s}{\partial \boldsymbol{P}} \cdot \frac{\partial H_s}{\partial \boldsymbol{x}} = 0. \tag{1.38}$$

This equation, known as the Liouville theorem, means that the distribution function is invariant following the trajectory of the particles in the 6-dimensional phase space. To take into account N particles and their interactions we add a collisional term on the RHS of the equation. Rewriting in terms of $(\boldsymbol{x}, \boldsymbol{v})$ and substituting the expressions for $\boldsymbol{P}$, H, $\boldsymbol{A}$ and ϕ given in the previous paragraph we obtain the plasma transport equation:

$$\frac{\partial f_s}{\partial t} + \boldsymbol{v} \cdot \frac{\partial f_s}{\partial \boldsymbol{x}} + \frac{q_s}{m_s} (\boldsymbol{E} + \boldsymbol{v} \times \boldsymbol{B}) \cdot \frac{\partial f_s}{\partial \boldsymbol{v}} = \left.\frac{\partial f_s}{\partial t}\right|_c. \tag{1.39}$$

The term on the RHS is the collision term and represents the changes in the distribution function in time due to the effects of collisions between particles. This equation is usually named depending on how the collision term is defined (e.g. Boltzmann equation, Fokker-Planck equation). However, space plasmas are in most cases collisionless. These are plasmas with sufficiently high temperatures and sufficiently low densities, where the collisions happen very rarely and they are negligible. They obey the Vlasov equation:

$$\frac{\partial f_s}{\partial t} + \boldsymbol{v} \cdot \frac{\partial f_s}{\partial \boldsymbol{x}} + \frac{q_s}{m_s} (\boldsymbol{E} + \boldsymbol{v} \times \boldsymbol{B}) \cdot \frac{\partial f_s}{\partial \boldsymbol{v}} = 0, \tag{1.40}$$

which, coupled with Maxwell's equations gives the description of distribution function and electromagnetic fields. Taking moments of the distribution function we

find thermodynamic quantities:

$$n_s = \int f_s d^3v \tag{1.41}$$

$$\boldsymbol{v}_s = \frac{1}{n_s} \int \boldsymbol{v} f_s d^3v \tag{1.42}$$

$$e_{kin,s} = \int \frac{m_s v^2}{2} f_s d^3v \tag{1.43}$$

$$\boldsymbol{Q} = \int \frac{m_s v^2}{2} \boldsymbol{v} f_s d^3v \tag{1.44}$$

$$\bar{\bar{P}}_s (\boldsymbol{x}, t) = m_s \int (\boldsymbol{v} - \boldsymbol{v}_s) (\boldsymbol{v} - \boldsymbol{v}_s) f_s(\boldsymbol{x}, \boldsymbol{v}, t) d^3v, \tag{1.45}$$

where $\bar{\bar{P}}_s$ is the pressure tensor, $\boldsymbol{Q}$ is the energy flux density and $e_{kin,s}$ is the kinetic energy of species s. From the Vlasov equation it is possible to obtain the following conservation laws:

- of particles, by integrating over velocity space:

$$\frac{\partial n_s}{\partial t} + \nabla \cdot (n_s \boldsymbol{v}_s) = 0, \tag{1.46}$$

  which implies conservation of mass and electric charge when multiplied by m_s and q_s.

- the momentum equation, multiplying times $m_s \boldsymbol{v}_s$ and integrating over velocity space:

$$\rho_s \frac{\partial \boldsymbol{v}_s}{\partial t} + \rho_s \boldsymbol{v}_s \cdot \nabla \boldsymbol{v}_s = -\nabla \cdot \bar{\bar{P}}_s + \boldsymbol{j}_s \times \boldsymbol{B} + \sigma_s \boldsymbol{E} i; \tag{1.47}$$

- the energy equation, dividing by $\frac{mv^2}{2}$ before integrating over velocity space:

$$\frac{\partial e_{kin,s}}{\partial t} + \nabla \cdot \boldsymbol{Q}_s = \boldsymbol{E} \cdot \boldsymbol{j}_s \tag{1.48}$$

- the pressure tensor equation, multiplying by $m_s (\boldsymbol{v} - \boldsymbol{v}_s) (\boldsymbol{v} - \boldsymbol{v}_s)$, integrating over velocity space and substituting the momentum equation and the conservation of mass:

$$\frac{\partial \bar{\bar{P}}_s}{\partial t} + \boldsymbol{v}_s \cdot \nabla \bar{\bar{P}}_s + \bar{\bar{P}}_s \nabla \cdot \boldsymbol{v}_s + \bar{\bar{P}}_s \cdot \nabla \boldsymbol{v}_s + \left[\bar{\bar{P}}_s \nabla \boldsymbol{v}_s \right]^T + \frac{q_s}{m_s} \boldsymbol{B} \times \bar{\bar{P}}_s + \frac{q_s}{m_s} \left[\boldsymbol{B} \times \bar{\bar{P}}_s \right]^T + \nabla \cdot \bar{\bar{Q}}_s = 0, \tag{1.49}$$

  where $\bar{\bar{Q}}_s$ is the third order heat flow tensor.

The system is a hierarchy of equation: each of them contains a higher order moment, which needs the following equation to be defined. In the equation for the pressure tensor we introduced the third order heat flow tensor, which is not defined. We could take a higher order moment of Vlasov equation to have an equation for $\bar{\bar{Q}}_s$ in the so called Landau-fluid model [Passot and Sulem, 2004], which is beyond the scope of this document. However we would introduce another higher order moment which would need another equation. The system of equation obtained taking moment of the Vlasov equation always needs a closure, since the number of unknowns is always greater by one of the number of equations. We will show this in more detail in the next paragraph.

We report here Maxwell's equations using the distribution function:

$$\nabla \cdot \boldsymbol{E} = \frac{1}{\epsilon_0} \sum_s q_s \int f_s d^3v \tag{1.50}$$

$$\nabla \times \boldsymbol{E} = -\frac{\partial \boldsymbol{B}}{\partial t} \tag{1.51}$$

$$\nabla \cdot \boldsymbol{B} = 0 \tag{1.52}$$

$$\nabla \times \boldsymbol{B} = \mu_0 \sum_s q_s \int \boldsymbol{v} f_s d^3v + \frac{1}{c^2} \frac{\partial \boldsymbol{E}}{\partial t}, \tag{1.53}$$

which together with the Vlasov equation describes the Vlasov-Maxwell system.

1.2.3 Fluid models

In plasma physics a fluid is a compressible medium described by macroscopic quantities which depend only on spatial coordinates and time. These quantities are called fluid variables and we have introduced them in the previous paragraph. They are obtained taking velocity moments of the distribution function. In the previous paragraph we showed also how to obtain the moment equations. However, the set we obtained is not complete: the equation for the pressure tensor contains a moment of third order, the heat flow tensor. If we were willing to write the equation for the heat flow tensor we would obtain a fourth order moment in the equation. In general the equation for the moment of order n obtains a moment of order $n+1$ for $n \in 0, 1, 2..\infty$. The set of equations is never complete. A complete set is obtained by truncation at a certain point which depends on the model.

However, in fluid models the heat flux is generally neglected, the pressure is assumed isotropic, $\bar{\bar{P}}_s = p_s \bar{\bar{I}}$, with $\bar{\bar{I}}$ unit tensor and p_s scalar pressure. Excluding chemical reaction in the collisions between particles we can obtain the equations for

the fluid model as:

$$\frac{\partial \rho_s}{\partial t} + \nabla \cdot (\rho_s \boldsymbol{v}_s) = 0, \tag{1.54}$$

$$\rho_s \frac{\partial \boldsymbol{v}_s}{\partial t} + \rho_s \boldsymbol{v}_s \cdot \nabla \boldsymbol{v}_s = -\nabla p_s + \boldsymbol{j}_s \times \boldsymbol{B} + \sigma_s \boldsymbol{E} + \boldsymbol{M}_{cs} = 0 \tag{1.55}$$

$$\frac{\partial p_s}{\partial t} + \boldsymbol{v}_s \cdot \nabla p_s + \frac{5}{3} p_s \nabla \cdot \boldsymbol{v}_s + N_{cs} \tag{1.56}$$

$$\sum_s \sigma_s = 0 \tag{1.57}$$

$$\nabla \times \boldsymbol{E} = -\frac{\partial \boldsymbol{B}}{\partial t} \tag{1.58}$$

$$\nabla \cdot \boldsymbol{B} = 0 \tag{1.59}$$

$$\nabla \times \boldsymbol{B} = \mu_0 \sum_s \boldsymbol{j}_s, \tag{1.60}$$

where $\boldsymbol{M}_{cs}$ and N_{cs} take into account the collisions and σ_s is the electric charge of species s. Here we made some additional approximations. We have neglected the displacement current $\boldsymbol{j}_D = \epsilon_0 \frac{\partial \boldsymbol{E}}{\partial t}$ in Ampère law (recognized as Darwin approximation in the "hybrid community") and assumed that quasi-neutrality holds, i.e. electrons move quickly enough, compared to the time scales of interest, to neutralize any charge in the plasma. These approximations can be derived assuming that the particles move in the non-relativistic limit. Notice that quasi-neutrality implies that Poisson equation cannot be longer used as it would imply $\nabla \cdot \boldsymbol{E} = 0$. Of particular interest are two different fluid models which we will describe in the following.

Two fluid model

Considering a plasma made by 2 species only, electrons and protons, the two-fluid model aims at using a momentum equation for the global electrons+ions fluid, combined with the electrons momentum equation. From quasi-neutrality $n_p = n_e = n$. Also, the sum of the effects of the collisions has to vanish as we assumed that there are no reactions between the particles. This yields $\boldsymbol{M}_{c,p} + \boldsymbol{M}_{c,e} = 0$ and $N_{c,p} + N_{c,e} = 0$. Summing the momentum equations for protons and ions:

$$\rho \frac{\partial \boldsymbol{v}}{\partial t} + \rho \boldsymbol{v} \cdot \nabla \boldsymbol{v} = -\nabla p + \boldsymbol{j} \times \boldsymbol{B}, \tag{1.61}$$

where ρ and p are the total density and pressure given by the sum of the single species and $\boldsymbol{v}$ is the bulk velocity, obtained averaging proton and electron velocities over density. To complete the set of equation, the electron momentum equation is

considered. After substituting

$$\boldsymbol{v}_e = \boldsymbol{v}_p - \frac{\boldsymbol{j}}{en_e}, \tag{1.62}$$

and considering the electron mass negligible when compared to the proton mass we obtain the Ohm's law:

$$\boldsymbol{E} + \boldsymbol{v}_p \times \boldsymbol{B} = -\frac{1}{en_e}\nabla p_e + \frac{1}{en_e}\boldsymbol{j} \times \boldsymbol{B} + \eta \boldsymbol{j}, \tag{1.63}$$

where η is the resistivity. This equation is of particular interest for space plasmas. In fact it is the massless electron fluid equation which is used in most of the hybrid simulation models that we will discuss later in this document. In these models, for phenomena occurring at ion scales, the second term of the RHS of the electron momentum equation, the Hall term, assumes an important role. For collisionless plasmas one should neglect the collisional term given by $\eta\boldsymbol{j}$. However to take into account the effects of turbulence we can include the term, referring to η as a turbulent resistivity.

Magnetohydrodynamics

The Magnetohydrodynamics (MHD) model is a simplified fluid model obtained with further assumptions from the two-fluid model. When the time and space scales of interest are large if compared to ion gyroperiod and Debye length the Ohm's law can be rewritten in its ideal form to find the set of equations:

$$\frac{\partial \rho}{\partial t} + \nabla \cdot (\rho \boldsymbol{v}) = 0 \tag{1.64}$$

$$\rho \frac{\partial \boldsymbol{v}}{\partial t} + \rho \boldsymbol{v} \cdot \nabla \boldsymbol{v} = -\nabla p + \boldsymbol{j} \times \boldsymbol{B} \tag{1.65}$$

$$\boldsymbol{E} + \boldsymbol{v} \times \boldsymbol{B} = 0 \tag{1.66}$$

$$\left(\frac{\partial}{\partial t} + \boldsymbol{v} \cdot \nabla\right)\left(\frac{p}{\rho^\gamma}\right) = 0 \tag{1.67}$$

$$\nabla \times \boldsymbol{E} = -\frac{\partial \boldsymbol{B}}{\partial t} \tag{1.68}$$

.

$$\nabla \cdot \boldsymbol{B} = 0 \tag{1.69}$$

$$\nabla \times \boldsymbol{B} = \mu_0 \boldsymbol{j}, \tag{1.70}$$

which represents the ideal MHD model. Here an ideal Ohm's law is used and no resistivity is included in the equations. Therefore the flux freezing is ideal. As there is no distinction between the electrons and ions fluids the pressure equation, which would assume the adiabatic form for each species, is postulated as adiabatic law for the all fluid. The index of the polytropic law, γ varies depending on the different phenomena of interest. MHD does not include a thermodynamic definition of temperature. However it is given from the ideal gas law:

$$p = nkT, \tag{1.71}$$

where k is the Boltzmann constant and n is the number density.

If the friction between the particles cannot be neglected a resistive term is added on the RHS of the ideal Ohm's law:

$$\boldsymbol{E} + \boldsymbol{v} \times \boldsymbol{B} = \eta \boldsymbol{j} \tag{1.72}$$

and the pressure equation becomes:

$$\left(\frac{\partial}{\partial t} + \boldsymbol{v} \cdot \nabla\right)\left(\frac{p}{\rho^\gamma}\right) = \frac{\gamma - 1}{\rho^\gamma}\eta j^2. \tag{1.73}$$

However, for sufficiently small values of the current density the quadratic term in the last equation can be neglected. The first equation of MHD expresses the conservation of mass. From the set of equation it is possible to obtain the conservation of energy in the form:

$$\frac{\partial}{\partial t}\left(\frac{\rho v^2}{2} + u + \frac{B^2}{2\mu_0}\right) + \nabla \cdot \left(\frac{\rho v^2}{2}\boldsymbol{v} + (u + p)\,\boldsymbol{v} + \frac{1}{\mu_0}\boldsymbol{E} \times \boldsymbol{B}\right), \tag{1.74}$$

where u is the internal energy.

1.3 Numerical models

In the previous section we presented the theoretical models used to study plasma. However, they involve coupled system of partial differential equations which cannot be solved analytically in most cases. Therefore the study of plasma physics phenomena heavily relies on numerical simulations.

The partial differential equations are discretized on a computational domain, i.e. a grid made of points, cells and edges which is a representation of the physical

domain. Time is subdivided in time steps and starting from an initial condition the solution is advanced step by step until the end of the simulation is reached. To achieve the discretization of the system of PDE under consideration, different applied mathematics approaches can be used, depending on the characteristics of the equations involved.

In this section we will review some kinetic and fluid numerical models, describing some features and the most common mathematical approaches used. Additionally we will introduce the concept of a hybrid model which is the main subject of this thesis.

1.3.1 Kinetic numerical models

Here we present two main kinetic numerical approaches:

- discretization of the Vlasov-Maxwell system of equations;
- the Particle In Cell (PIC) model.

The main differences between the two is that the former uses an Eulerian approach while the latter uses a Lagrangian approach. Furthermore the former approximates a continuous function for the distribution function, while the latter uses a Monte Carlo method to approximate positions and velocities of particles. In the Vlasov-Maxwell system of equations phenomena are studied focusing on specific spatial locations where the flow is calculated solving an equation for the distribution function. In the Particle In Cell the focus is on the single particles which are moved in a grid used to collect density and current from particles position and velocity. Both cases use a computational grid to compute fields but in the PIC model they need to be interpolated at particles positions.

Vlasov-Maxwell system of equations

The Vlasov-Maxwell system of equations given in Eqs.(1.40,1.50,1.51,1.52,1.53) is discretized in space, velocity and time. The system is solved in a 6-dimensional computational domain at each time step. This makes the Vlasov-Maxwell system of equations CPU and memory expensive.

The Vlasov equation can be seen as an advection equation in space and velocity domains. A common approach is to split the equation in space and velocity operators [Cheng and Knorr, 1976]. The operator splitting is widely used and described in Chap.4.

Between the mathematical methods commonly used to solve the system we mention here:

- Weighted Essentially Non Oscillatory (WENO) methods for hyperbolic conservation laws to solve the Vlasov equation [Carrillo and Vecil, 2007, Qiu. and Shu, 2005] ;
- Discontinuous Galerkin [Cheng et al., 2014, Qiu and Shu, 2011];
- Conservative flux based methods, e.g. Filbet et al. [2001];
- Energy conserving finite difference [Arakawa and R. Lamb, 1981];
- Fourier-Hermite discretization [Camporeale et al., 2013a,b, Parker and Dellar, 2015].

The description of these algorithms is beyond the scope of this document and we refer the reader to the references for more information.

Particle In Cell

Another type of kinetic approach is the Particle In Cell (PIC) method. The method was first introduced by Harlow [1955] to study the strongly non-linear dynamics of different materials in multi-dimensional problems [Harlow, 1988]. It is suitable to simulate collisionless phenomena. Maxwell's equation are discretized on a finite grid and the continuous magnetic and electric fields assume values at grid points. The continuous probability density function is replaced by the sum of computational macro particles:

$$f(\boldsymbol{x}, \boldsymbol{v}) \Rightarrow \sum_{i=1}^{N} S(\boldsymbol{x} - \boldsymbol{x}_i)\, \delta(\boldsymbol{v} - \boldsymbol{v}_i), \tag{1.75}$$

where $S(\boldsymbol{x})$ is the space shape function and $\delta(\boldsymbol{v})$ is the velocity shape function. Both have the properties to be normalized and symmetric. The macro particles are assumed to be at a precise velocity given by the shift of the Kronecker delta function. This is possible because the velocity space is not discretized. The number of simulation particles N is very large to minimize statistical noise, but much smaller than the number of actual physical particles.

The spatial shape functions are used to collect the moments at grid points and to interpolate fields at particle's positions. For this purpose b-splines are often used

(Lapenta [2012]) in the form:

$$b_0(\xi) = \begin{cases} 1 & \text{if } |\xi| < 1/2 \\ 0 & \text{otherwise} \end{cases} \tag{1.76}$$

$$b_l(\xi) = \int_{-\infty}^{\infty} b_0(\xi - \xi')\, b_{l-1}(\xi')\, d\xi', \tag{1.77}$$

where b_l increases the order of accuracy of the interpolation with increasing l.

Taking moments of the Vlasov equation it is possible to obtain the equations of motion for the macroparticles:

- the 0^{th} order moment gives:
$$\frac{dN_p}{dt} = 0, \tag{1.78}$$
which states that the number of particles per macro particle is constant in time;

- multiplying by $\boldsymbol{x}$ and integrating over the phase space gives:
$$\frac{d\boldsymbol{x}_p}{dt} = \boldsymbol{v}_p; \tag{1.79}$$

- multiplying by $\boldsymbol{v}$ and integrating over the phase space gives:
$$\frac{d\boldsymbol{v}_p}{dt} = \frac{q_s}{m_s}\left(\boldsymbol{E}_p + \boldsymbol{v}_p \times \boldsymbol{B}_p\right). \tag{1.80}$$

The last two are Newton's equations of motion for macro particles. The electric field $\boldsymbol{E}_p$ is interpolated at particles positions using the shape functions:

$$\boldsymbol{E}_p = \int S(\boldsymbol{x} - \boldsymbol{x}_p)\, \boldsymbol{E}(\boldsymbol{x})\, d\boldsymbol{x}, \tag{1.81}$$

where $\boldsymbol{E}(\boldsymbol{x})$ is calculated at grid point and considered constant in the cells:

$$\boldsymbol{E}(\boldsymbol{x}) = \sum_i \boldsymbol{E}_i b_0\left(\frac{\boldsymbol{x} - \boldsymbol{x}_i}{\Delta \boldsymbol{x}}\right). \tag{1.82}$$

Substituting in $\boldsymbol{E}_p$:

$$\boldsymbol{E}_p = \sum_i \boldsymbol{E}_i \int b_0\left(\frac{\boldsymbol{x} - \boldsymbol{x}_i}{\Delta \boldsymbol{x}}\right) S_{\boldsymbol{x}}(\boldsymbol{x} - \boldsymbol{x}_p)\, d\boldsymbol{x} = \sum_i \boldsymbol{E}_i W(\boldsymbol{x}_i - \boldsymbol{x}_p). \tag{1.83}$$

Here W is the weight function given by the next order b-spline:

$$W\left(\boldsymbol{x}_i - \boldsymbol{x}_p\right) = b_{l+1}\left(\frac{\boldsymbol{x}_i - \boldsymbol{x}_p}{\Delta \boldsymbol{x}}\right). \tag{1.84}$$

An analogous procedure can be done for the magnetic field, starting from:

$$\boldsymbol{B}_p = \int S\left(\boldsymbol{x} - \boldsymbol{x}_p\right) \boldsymbol{B}\left(\boldsymbol{x}\right) d\boldsymbol{x}. \tag{1.85}$$

The density and current are collected at grid points using the functional form of the distribution function:

$$\rho_s\left(\boldsymbol{x}, t\right) = \sum_p q_s N_p S_{\boldsymbol{x}}\left(\boldsymbol{x} - \boldsymbol{x}_p\right), \tag{1.86}$$

$$\boldsymbol{j}_s\left(\boldsymbol{x}, t\right) = \sum_p q_s N_p \boldsymbol{v}_p S_{\boldsymbol{x}}\left(\boldsymbol{x} - \boldsymbol{x}_p\right). \tag{1.87}$$

A simple Particle in Cell algorithm can be summarized in the following steps:

1. initialization of the particles, positioning them in the spatial phase space according to the density and using a Monte Carlo method to assign them a velocity according with their distribution function;
2. initialization of electromagnetic fields at grid point
3. for each macro particle interpolation of fields and calculation of acceleration;
4. use of the acceleration to compute the velocity;
5. use of the velocity to change the position;
6. use of new positions and velocities to collect density and current at grid points;
7. calculation of new electromagnetic fields at grid point

The points from 3 to 7 are repeated until reaching the end of the simulation. However a simple explicit advancement of velocities and positions often leads to numerical instabilities.

The integration of the equations of motion for each particle is usually carried out through a leapfrog in time of position and velocity and integrating the second Newton's law with Boris algorithm [Birdsall and Langdon, 2004]. Starting from $t = 0$, $\boldsymbol{x}_p$ is advanced explicitely of $\Delta t/2$. Knowing positions at $t = (n + 1/2)\,\Delta t$

and velocities at $t = n\Delta t$ the former are used to interpolate the fields and the Newton's equation are discretized as follows:

$$m_p \frac{\boldsymbol{v}_p^{n+1} - \boldsymbol{v}_p^n}{\Delta t} = q_p \left(\boldsymbol{E}_p^{n+1/2} + \boldsymbol{v}_p^{n+1/2} \times \boldsymbol{B}_p^{n+1/2} \right) \tag{1.88}$$

$$\frac{\boldsymbol{x}_p^{n+3/2} - \boldsymbol{x}_p^{n+1/2}}{\Delta t} = \boldsymbol{v}_p^{n+1}. \tag{1.89}$$

The presence of $\boldsymbol{v}_p^{n+1/2}$ on the RHS of the velocity advancement makes things a bit complicated.

However Boris et al. [1970] introduced a second order stable algorithm. The Lorentz force is split in electric and magnetic components. The integration is carried out applying first half acceleration due to $\boldsymbol{E}$, then full rotation due to $\boldsymbol{B}$ and finally another half acceleration:

$$m_p \frac{\boldsymbol{v}_p^{-} - \boldsymbol{v}_p^n}{\Delta t} = q_s \boldsymbol{E}_p^{n+1/2} \tag{1.90}$$

$$m_p \frac{\boldsymbol{v}_p^{+} - \boldsymbol{v}_p^{-}}{\Delta t} = q_s \frac{\boldsymbol{v}_p^{-} + \boldsymbol{v}_p^{-}}{\Delta t} \times \boldsymbol{B}_p^{n+1/2} \tag{1.91}$$

$$m_p \frac{\boldsymbol{v}_p^{n+1} - \boldsymbol{v}_p^{+}}{\Delta t} = q_s \boldsymbol{E}_p^{n+1/2}. \tag{1.92}$$

The method has been proved to conserve energy for vanishing electric field and is currently the standard pusher for explicit Particle In Cell codes. Implicit particles pushers [Friedman et al., 1955] [Pogorelov et al., 2009] [Markidis et al., 2009] exist but are beyond the scope of this document.

1.3.2 Fluid numerical models

The system of equations which constitutes a fluid model (see previous section) is generally composed of an equation for conservation of mass, a force equation, a pressure equation, Ohm's law and Maxwell's equations, where the Poisson equation is usually dropped due to quasi-neutrality [Tóth, 2011]. It is possible and convenient to rewrite the equations in conservative form. We report here the MHD case:

$$\frac{\partial \rho}{\partial t} = -\nabla \cdot (\rho \boldsymbol{v}) \tag{1.93}$$

$$\frac{\partial \rho \boldsymbol{v}}{\partial t} = -\nabla \cdot \left(\boldsymbol{v} \rho \boldsymbol{v} + \bar{\bar{I}} p + \bar{\bar{I}} \frac{B^2}{2} - \boldsymbol{B}\boldsymbol{B} \right) \tag{1.94}$$

$$\frac{\partial e}{\partial t} = -\nabla \cdot \left[\left(\boldsymbol{v}\,(e+p) + \boldsymbol{v} \cdot (\bar{\bar{I}}\frac{B^2}{2} - \boldsymbol{B}\boldsymbol{B} \right) - \boldsymbol{B} \times \eta \boldsymbol{j} \right] \tag{1.95}$$

$$\frac{\partial \boldsymbol{B}}{\partial t} = \nabla \times (\boldsymbol{v} \times \boldsymbol{B} - \eta \boldsymbol{j})\,, \tag{1.96}$$

where

$$e = \frac{p}{\gamma - 1} + \frac{\rho v^2}{2} + \frac{B^2}{2} \tag{1.97}$$

is the energy density. Here Ohm's law has been substituted in Eq.(1.96). To solve this system any numerical approach for conservation laws can be used e.g.:

- Lax Wendroff Scheme with artificial viscosity;
- Finite Difference Scheme with artificial viscosity;
- Flux Corrected Transport (FCT) [Boris and Book, 1973];
- TVD scheme with Lax-Friedrichs, HLL, HLLC, HLLD or Roe flux;
- Essentially Non Oscillatory and Weighted Essentially Non Oscillatory methods;
- Finite Elements;
- Spectral Elements;
- Finite Volume;
- Spectral Volume.

A widely used numerical technique is the Adaptive Mesh Refinement. The latter has the goal to allow to study phenomena on scales much smaller of the overall domain using higher spatial and temporal resolution where needed. Starting from a coarse grid, regions where a finer grid is needed are identified. This can be done using different criteria, e.g. error estimates, gradients, geometrical criteria. In these regions finer sub-grids are superimposed. This method is clearly more efficient than using a finer grid in all the computational domain. Adaptive Mesh Refinement implementation is much more complex for PIC models than fluid models. In fact the technique makes use of an irregular grid on which the tracking of particles movement is more difficult.

1.3.3 Hybrid models

Hybrid models have been developed to study some kinetic behaviour over regions of large volume of plasma. In astrophysical plasma simulations the sizes of the box are usually very large if compared to the electron gyroradius. A very large number of cells in each direction are needed to resolve electron motion. For explicit numerical schemes stability conditions give a constraint on time step length given the cell size. When the cell size is reduced the time step needs to be reduced accordingly. For this reason one might decide to neglect kinetic electrons and focus only on ion motion, treating the electrons as a whole fluid. In fact the ions gyroradius is $\frac{m_i}{m_e}^{1/2}$ bigger than the electrons one so a much smaller number of cells are needed to resolve ions gyration.

While the electrons are treated as a whole fluid, typically including only the electron's momentum equation to compute the electric field, the ions are treated kinetically using either a Particle In Cell or a Vlasov-Maxwell approach. These methods are explained throughout the rest of this thesis.

1.4 Linear Vlasov theory

In this section we provide an introduction to plasma microinstabilities useful for the reading of Chap. 5 and Chap. 6. We proceed describing briefly what are plasma microinstabilities, then we focus on their analysis describing the fundamentals of linear Vlasov theory. Finally we present a linear solver code implementation written by Enrico Camporeale and David Burgess that we used throughout this thesis as a reference to compare our results from simulations.

1.4.1 Plasma microinstabilities

Several different type of instabilities can grow in plasmas. Some of them are associated with macroscopic phenomena, e.g. gradients in fluid quantities, others are associated with microscopic phenomena, i.e. perturbations in the distribution function from Maxwellian equilibrium. The latter are called plasma microinstabilities.

For a plasma to be in equilibrium all the species need to have a Maxwellian distribution function with the same temperature and bulk velocity. This is not generally the case in a magnetized plasma. In fact, taking the solar wind as example, the presence of a directional background magnetic field $\boldsymbol{B}_0$ generates heating and cooling processes which act non-isotropically, in direction parallel or perpendicular

to $\boldsymbol{B}_0$ leading to non equilibrium conditions. In the solar wind there is indeed a broad range of phenomena which can cause the plasma to deviate from equilibrium conditions, e.g. double adiabatic expansion, anisotropic dissipation of turbulence. These phenomena cause perturbations in the distribution function from Maxwellian state, therefore leading to microinstabilities.

Due to their nature, the study of plasma microinstabilities involves the use of kinetic methods. These involve the solution of a system of non-linear equations which is not possible to accomplish in an analytical way. One way is to use the numerical approaches seen in the previous section to fully study their growth and saturation (i.e. the phase of the instability when it stops growing). Numerical methods are a powerful tool, but in order to be used they need to be validated with comparisons with theoretical models.

Linear Vlasov theory uses a linear expansion of the Vlasov equation to study small amplitude waves in plasma [Gary, 1993]. It assumes that the plasma is collisionless and it is valid only in the first phase of the instability, where the oscillations are small. It is used to compute the linear growth rates of microinstabilities, a quantity that indicates how the wave's amplitude changes in time and to find the dispersion relation, i.e. an equation which correlates frequency and wave vector for a certain instability (more details in the next section). The linear growth rate can be computed also from numerical simulations. Later in this thesis we used the comparison between linear theory and our simulations to validate our code.

However, this method can be used to study only the initial small amplitude linear phase of an instability. To describe what happens when the perturbations become larger one needs to use numerical simulations.

1.4.2 Linear Vlasov theory

Linear Vlasov theory starts from the Vlasov equation that we saw earlier in this chapter. For species j it reads:

$$\frac{\partial f_j}{\partial t} + \boldsymbol{v} \cdot \frac{\partial f_j}{\partial \boldsymbol{x}} + \frac{q_j}{m_j} \left(\boldsymbol{E} + \boldsymbol{v} \times \boldsymbol{B} \right) \cdot \frac{\partial f_j}{\partial \boldsymbol{v}} = 0, \tag{1.98}$$

together with Maxwell equations. Here the distribution function of species j is a function of seven variables $(\boldsymbol{x}, \boldsymbol{v}, t)$ and the fields are functions of four $(\boldsymbol{x}, t)$. The equation for one species is coupled through the fields to the equations for the other species. It is therefore challenging (if not impossible) to solve this system of equations analytically.

Linear theory assumes that at any time distribution function and fields are given by the sum of the initial state plus a perturbed state approximated by a plane wave. In particular:

$$f_j(\boldsymbol{x},\boldsymbol{v},t) = f_j^{(0)}(\boldsymbol{x},\boldsymbol{v}) + f_j^{(1)}(\boldsymbol{x},\boldsymbol{v},t) \\ = f_j^{(0)}(\boldsymbol{x},\boldsymbol{v}) + f_j^{(1)}(\boldsymbol{k},\boldsymbol{v},\omega)\exp\left[i\left(\boldsymbol{k}\cdot\boldsymbol{x}-\omega t\right)\right], \quad (1.99)$$

$$\boldsymbol{E}(\boldsymbol{x},t) = \boldsymbol{E}^{(0)}(\boldsymbol{x}) + \boldsymbol{E}^{(1)}(\boldsymbol{x},t) \\ = \boldsymbol{E}^{(0)}(\boldsymbol{x}) + \boldsymbol{E}^{(1)}(\boldsymbol{k},\omega)\exp\left[i\left(\boldsymbol{k}\cdot\boldsymbol{x}-\omega t\right)\right], \quad (1.100)$$

$$\boldsymbol{B}(\boldsymbol{x},t) = \boldsymbol{B}^{(0)}(\boldsymbol{x}) + \boldsymbol{B}^{(1)}(\boldsymbol{x},t) \\ = \boldsymbol{B}^{(0)}(\boldsymbol{x}) + \boldsymbol{B}^{(1)}(\boldsymbol{k},\omega)\exp\left[i\left(\boldsymbol{k}\cdot\boldsymbol{x}-\omega t\right)\right]. \quad (1.101)$$

Here $\boldsymbol{k}$ is the wave vector, ω is the angular frequency and i the imaginary unit. Conventionally the former assumes real values, while the latter is a complex number: $\omega = \omega_r + i\omega_i$. ω_i is usually referred as γ or growth rate, a quantity which indicates the temporal behaviour of the perturbation. When $\gamma > 0$, the multiplication of ω times $-i$ results in a positive real part of the exponential, therefore leading to a growth in the wave's amplitude. Conversely if $\gamma < 0$ the wave decays.

However, ω for a certain wave is a function of k through the dispersion relation. Therefore $\gamma = \gamma(\boldsymbol{k})$. If $\gamma(\boldsymbol{k}) > 0$ for at least some values of $\boldsymbol{k}$ the plasma is considered unstable and the the wave exhibits exponential growth. The dispersion relation has usually a very complicated form. Anyhow, numerical tools allow the computation of $\gamma(\boldsymbol{k})$ for any given $\boldsymbol{k}$. This function has frequently multiple local maxima which might be larger than zero causing therefore an instability to develop. Instead of considering the function for all the values of $\boldsymbol{k}$ usually ranges of $\boldsymbol{k}$ are associated to different instabilities, assigning one local maxima only to one instability. The former is called the linear growth rate of the instability:

$$\gamma_{max} = \gamma(\boldsymbol{k}_{max}) = max\big|_{\boldsymbol{k}}\,\gamma(\boldsymbol{k}), \quad (1.102)$$

where the maximum is computed in the range of $\boldsymbol{k}$ corresponding with the instability under consideration.

We will proceed now deriving the dispersion relation for a uniform magnetized plasma. We choose the frame of reference which results in no net current for the

unperturbed plasma. We fix:

$$\boldsymbol{E}^{(0)}(\boldsymbol{x}) = 0, \tag{1.103}$$

and

$$\boldsymbol{B}^{(0)}(\boldsymbol{x}) = B_0 \boldsymbol{e}_z. \tag{1.104}$$

Using parallel and perpendicular directions to the background magnetic field, the wave vector is given by:

$$\boldsymbol{k} = k_\perp \boldsymbol{e}_\perp + k_\parallel \boldsymbol{e}_\parallel, \tag{1.105}$$

where the parallel direction is along the z ax. The angle of propagation of the wave respect to the background magnetic field θ is given by:

$$\cos\theta = \frac{k_\parallel}{k}, \tag{1.106}$$

where k is the wave number, i.e. the magnitude of the wave vector.

These assumptions yield:

$$\boldsymbol{E}(\boldsymbol{x}, t) = \boldsymbol{E}^{(1)}(\boldsymbol{x}, t) = \boldsymbol{E}^{(1)}(\boldsymbol{k}, \omega) \exp\left[i\left(\boldsymbol{k}\cdot\boldsymbol{x} - \omega t\right)\right], \tag{1.107}$$

$$\boldsymbol{B}(\boldsymbol{x}, t) = \boldsymbol{B}_0 + \boldsymbol{B}^{(1)}(\boldsymbol{x}, t) = \boldsymbol{B}_0 + \boldsymbol{B}^{(1)}(\boldsymbol{k}, \omega) \exp\left[i\left(\boldsymbol{k}\cdot\boldsymbol{x} - \omega t\right)\right], \tag{1.108}$$

and

$$\boldsymbol{J}(\boldsymbol{x}, t) = \boldsymbol{J}^{(1)}(\boldsymbol{x}, t) = \boldsymbol{J}^{(1)}(\boldsymbol{k}, \omega) \exp\left[i\left(\boldsymbol{k}\cdot\boldsymbol{x} - \omega t\right)\right]. \tag{1.109}$$

We now substitute these expressions in Faraday's and Ampère's laws to obtain an equation for the first order perturbations:

$$\mu_0 \boldsymbol{J}^{(1)}(\boldsymbol{k}, \omega) = \frac{i}{\omega}\boldsymbol{k} \times \left(\boldsymbol{k} \times \boldsymbol{E}^{(1)}(\boldsymbol{k}, \omega)\right) + \mu_0 \epsilon_0 i\omega \boldsymbol{E}^{(1)}(\boldsymbol{k}, \omega). \tag{1.110}$$

The first order current density is the sum of the first order particle flux density, $\boldsymbol{\Gamma}_j^{(1)}(\boldsymbol{k}, \omega)$, times the charge for each species j:

$$\boldsymbol{J}^{(1)}(\boldsymbol{k}, \omega) = \sum_j q_j \boldsymbol{\Gamma}_j^{(1)}(\boldsymbol{k}, \omega), \tag{1.111}$$

where:

$$\boldsymbol{\Gamma}^{(1)}(\boldsymbol{k}, \omega) = \int_{-\infty}^{\infty} \boldsymbol{v} f_j^{(1)}(\boldsymbol{k}, \boldsymbol{v}, \omega) d^3\boldsymbol{v}. \tag{1.112}$$

Here the integral is performed over the three velocity directions.

The particle density flux is related to the electric field through the dimensionless

conductivity tensor, $\bar{\bar{S}}_j(\boldsymbol{k},\omega)$:

$$\boldsymbol{\Gamma}^{(1)}(\boldsymbol{k},\omega) = -\frac{i\epsilon_0 k^2 c^2}{q_j \omega}\bar{\bar{S}}_j(\boldsymbol{k},\omega)\cdot\boldsymbol{E}^{(1)}(\boldsymbol{k},\omega). \tag{1.113}$$

The latter equation combined with Eq.(1.110) and Eq.(1.111) yields:

$$\bar{\bar{D}}(\boldsymbol{k},\omega)\cdot\boldsymbol{E}^{(1)}(\boldsymbol{k},\omega) = 0, \tag{1.114}$$

where

$$\bar{\bar{D}}(\boldsymbol{k},\omega) = \left(\omega^2 - c^2k^2\right)\bar{\bar{1}} + c^2\boldsymbol{k}\boldsymbol{k} + c^2k^2\sum_j \bar{\bar{S}}_j(\boldsymbol{k},\omega) \tag{1.115}$$

is the plasma dispersion tensor. Here $\bar{\bar{1}}$ is the unit tensor and $\boldsymbol{k}\boldsymbol{k}$ is the dyadic product of $\boldsymbol{k}$ times itself. Since $\boldsymbol{E}^{(1)}(\boldsymbol{k},\omega) \neq 0$, or there would not be any perturbation in the plasma we require that:

$$det\left[\bar{\bar{D}}(\boldsymbol{k},\omega)\right] = 0. \tag{1.116}$$

This, knowing the expression for $\bar{\bar{S}}_j(\boldsymbol{k},\omega)$, yields to the dispersion relation. The procedure to find the conductivity tensor involves the use of the initial distribution function for each species, i.e. $f_j^{(0)}(\boldsymbol{x},\boldsymbol{v},t)$, which is different depending on the instability considered and goes beyond the scope of this document. Details are given in Gary [1993]. This is a drawback of the method which requires to know a priory which instability one wants to study.

1.4.3 Linear solver

Throughout this document we will be using a linear solver written by Enrico Camporeale and David Burgess. The latter is an implementation of the procedure explained in Podesta [2012].

Equation(1.116) is solved numerically expanding the determinant as a function $f(z)$ of the complex variable $z = \omega'/k'_{\parallel}$, where $\omega' = \omega/\Omega_p$ is the ion cyclotron frequency normalized frequency and $\boldsymbol{k}' = \boldsymbol{k}\rho_p$ is the thermal proton gyroradius normalized wave vector. z is the dimensionless parallel phase velocity. We denote that $f(z)$ is not the distribution function, but here represents the function obtained solving Eq. (1.116). The function $f(z)$ is expressed as a series of terms containing the modified Bessel functions and the plasma dispersion function in the case of Maxwellian distributions of particles. To find the roots of $f(z) = 0$ in the complex

plane one follows this procedure:

- the contours of $\frac{1}{|f(z)|} = const$ are plotted using a graphical routine;
- the roots of $f(z)$ are where $\frac{1}{|f(z)|} \to \infty$, so where we find the maxima in the plot; those are found visually on the contour plot;
- once a small region containing a root is identified the root itself is found using the Newton method.

In the second step some roots might be lost because of the grid resolution used in the plot and different roots might happen to be in the same plotting cell. To avoid this special attention is required.

The location of the root as a function of $k = |\boldsymbol{k}|$ at fixed θ is found varying the value of k slowly and following the trajectory of the root itself in the complex plane.

1.5 Thesis outline

My work has been focused on the development, implementation and testing of a new Vlasov-hybrid algorithm with Hermite expansion of the distribution function with the goal to improve the simulation models available for the study of low growth rate instabilities.

This thesis is composed by this introduction followed by seven chapters (Chapter 2 to Chapter 8).

In the introduction we have described the solar wind, the medium where plasma turbulence is continuously observed. We presented some simple plasma theoretical and numerical models that are needed later in this document to fully understand the equations we are solving in the code we developed. Then we introduced plasma microinstabilities and a tool for their analysis.

In Chapter 2 we will introduce turbulence, describing the interesting problem of the turbulent energy cascade. We will then review the current state of hybrid simulations underlying that there is a need of improvement in Vlasov-hybrid algorithms.

In Chapter 3 we will focus on existing hybrid algorithms. We will first present the different algorithms for the hybrid time advancement then we will study how electron inertia has been introduced by several different authors. Also, we will present a suite of existing hybrid algorithms that we elaborated, comparing the results on a set of different tests. This code has been used for teaching purposes at the 12^{th} International Summer School/Symposium for Space Simulations (ISSS-12).

In Chapter 4 we will present a 1D3V Vlasov-hybrid algorithm and code implementation. The latter performs the discretization in the velocity space using the asymmetrically weighted Hermite basis to reduce the computational costs involved in Vlasov simulations. Here we will describe the simple tests that we used to validate the code by comparison with linear Vlasov theory.

In Chapter 5 we will study a proton cyclotron temperature anisotropy instability with low growth rate. We will compare the linear growth rate obtained with our Hermite Vlasov-hybrid code with the ones expected by linear Vlasov theory and the ones obtained with the *CAM-CL* PIC-hybrid code we developed. We will show that our code is extremely more accurate on this type of instability, even when the number of particles used in the PIC-hybrid simulation becomes very large.

In Chapter 6 we will study an ion/ion right hand resonant instability using two different values of relative drift velocity between core and beam populations. We will show that our code is capable of capturing the evolution of the right mode in the linear phase, resulting in a linear growth rate more accurate in the case with lower linear growth rate. When the growth rate increases, due to the increase in the relative drift velocity between the two populations, the PIC-hybrid simulation gives better results.

In Chapter 7 we will describe the implementation of the 2D3V version of the code and some preliminary results.

Finally in Chapter 8 we will deduce some conclusions and discuss the possible future works.

2 Use of hybrid codes in space plasma turbulence studies

In this chapter we will introduce the motivation behind the work described in the later chapters.

We start by defining the length scales of interest. Hybrid codes are capable of capturing ion dynamics in large regions of volume such as space plasmas. However, the electrons are treated as a fluid and their dynamics is neglected. We are therefore interested in ion scales which are the scales at which ion dynamics happen. This are subdivided in two main ranges:

- the ion inertial range, for lengths of interest comparable to the ion inertial length $d_i = \frac{c}{\omega_{p,i}}$, where c is the speed of light and $\omega_{p,i}$ is the ion plasma frequency. At this scales the ions decouple from the electrons and the magnetic field is frozen into the electron fluid;

- the ion gyration scales, for lengths of interest comparable to the ion gyroradius $r_{L,i} = \frac{v_{th,i}}{\Omega_i}$, where $v_{th,i}$ is the ion thermal velocity and Ω_i is the ion gyrofrequency. At this scales it is possible to follow the ions gyration motion.

Turbulence in space plasma is a phenomena not yet well understood. In fact, even though there are theoretical models to study turbulence, these are not valid for all the scales of interest, and there are aspects of observations and simulation results which are not completely explained. Often it is referred to as the last unsolved problem in classical physics.

However, we must first give a definition of turbulence. In general it can be defined as violent or unsteady movement of a fluid. For example an aircraft entering a turbulent region of the atmosphere starts moving in a violent and unpredictable way. This motion and in particular the one of the air is not regular and shows some apparently random effect. This definition is qualitative and does not allow to distinguish, following a quantitative assessment, between turbulent and non turbulent, i.e. laminar flow. The latter is a flow where the fluid moves following steady stream lines.

Hydrodynamics provides criteria to identify the transition between the two different regimes, and since plasma is seen as a magnetized fluid these criteria are adopted also in space plasma physics. A typical approach to study hydrodynamics phenomena is to define dimensionless numbers as combination of fluid variables, through which it is possible to identify the characteristics of a process. Turbulence is described by the Reynolds number, R_e, defined as the ratio between inertial and viscous forces acting on a fluid. From this definition we can say that for a fluid not in motion $R_e = 0$, since the inertial forces vanish. At the same time for increasing flow velocity of a fluid in motion we can expect R_e to increase. Its definition is

$$R_e = \frac{\rho v L}{\mu} = \frac{v L}{\nu}. \tag{2.1}$$

Here ρ is the mass density, v is the bulk flow velocity, L is the length scale of interest, μ and ν are the dynamic and kinematic viscosities.

The value of Reynolds number is used to identify the different types of flow. For $R_e < 2300$ the regime is considered to be laminar. When R_e becomes > 2300 there is first a transition region where both laminar and turbulent flow can coexist. This happens for $2300 < R_e < 4000$. For Reynolds numbers bigger than 4000 the flow is considered turbulent: the motion along parallel stream lines is lost and the formation of vortexes and irregularities are observed. Defining the vorticity:

$$\boldsymbol{\omega} = \nabla \times \boldsymbol{v}, \tag{2.2}$$

we have here $\boldsymbol{\omega} \neq 0$.

In space plasma physics the irregularities give rise to perturbations in the flow and the fields at different scales. It is interesting to study how the kinetic energy resulting from these perturbations distributes as function of the wave number k. The most well known theoretical model is Kolmogorov [1941]. However, as we will see in detail in the next section, this is valid only for certain ranges of k (the so called inertial range). What is observed and obtained as result of simulations outside these ranges is currently a matter of interest for the scientific community. In fact a strong matching between observational data and simulations results at high k values (where other plasma scales are important) is still not completely explained yet.

Due to the nature of the problem, which involves perturbations with large variations in k, which means very different length scales, the choice of hybrid codes as a tool is widely adopted. In fact the length resolution of hybrid algorithms is broad and extends the range from MHD to sub-ion scales. While fluid codes are

able to verify the theoretical models, they cannot be used to study what happens outside of the inertial range. Full PIC codes can resolve perturbations at electrons scales, but they do not allow the simulation of large volumes, therefore neglecting perturbations at lower k. One may argue that hybrid codes neglect electron kinetics which might be important at the scales of interest. However a strong agreement between observations and hybrid simulations, as we will show in more details later in this chapter, suggests that electrons effects are negligible.

In this chapter we will first present the Kolmogorov model of turbulence, defining its ranges of applicability and limitations. Then we will describe some observational data of the turbulent energy cascade, explaining the problems of interest. Then we will see how the latter has been studied using Vlasov-Hybrid and PIC-Hybrid codes, showing that the current simulations need improvements due to their CPU and memory cost, which makes them slow and hard to use for actual science. This reasoning has motivated us to develop a new Vlasov-Hybrid code which uses a spectral expansion of the distribution function to reduce memory usage and the number of calculations needed.

2.1 Kolmogorov model of turbulence

Kolmogorov [1941] first described the fundamental theory of hydrodynamic turbulence. To obtain a simple tractable model he assumed that the velocity fluctuations due to turbulent phenomena are isotropic, i.e. the same in all velocity directions, and homogeneous, i.e. distributed in space in the same way. Also, he assumed a stationary regime, considering as constant the statistical properties such as mean, variance and power spectrum of fluids and fields quantities, with kinetic energy dissipation happening only at small scales (i.e. for large k).

Turbulence can be considered as a consequence of injection of energy in a system. This energy causes the particles to move generating perturbations on the distribution function at certain length scales L called the stirring scale. Eddies and vortexes are driven by the particle motion with dimensions comparable to the stirring scale. It is therefore convenient to define $k_{in} = 2\pi/L$. The eddies can break forming smaller ones, transferring energy to higher k. This transfer of energy constitutes the turbulent cascade. When the k becomes large the energy is transformed in heat, being therefore dissipated. In Fig.(2.1) we show a schematic power spectrum of the kinetic energy in a turbulent phenomena. The graph shows a negative power law behaviour for a range of k called the inertial sub-range.

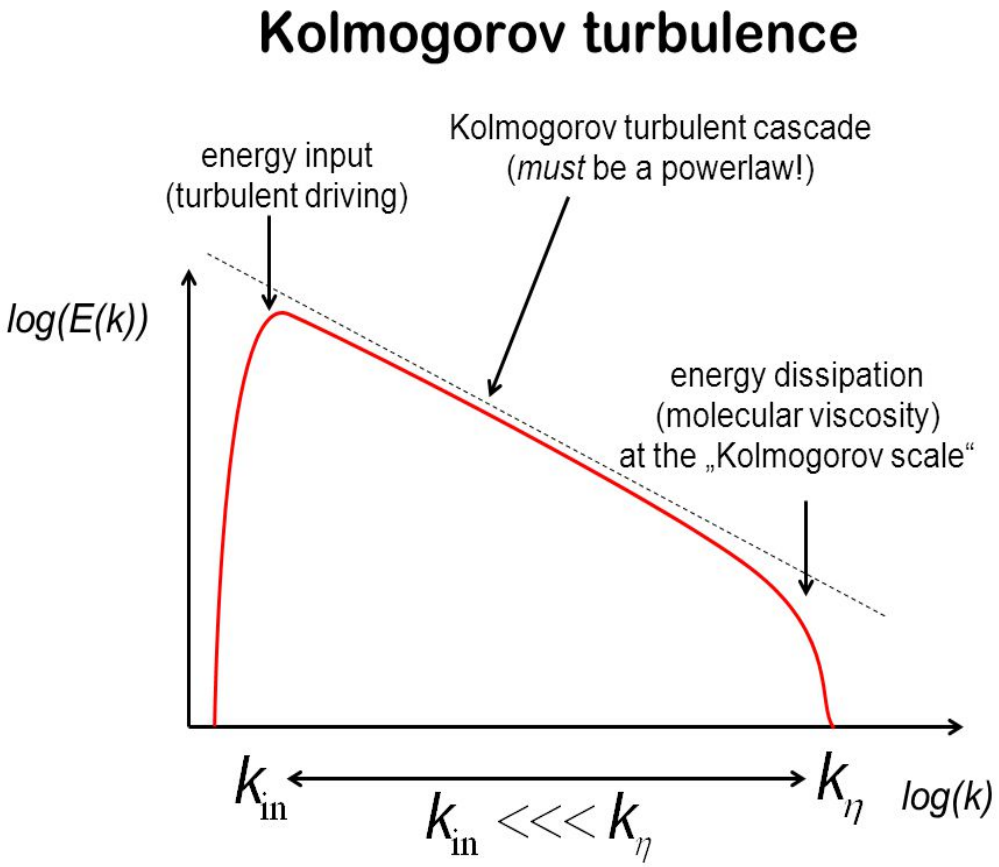

Figure 2.1: Schematic energy distribution in a turbulent energy cascade. The graph contains the logarithm of the kinetic energy in function of k. k_{in} is the k at which the energy is injected in the system, k_η is the value of k for which the energy is dissipated. The linear behaviour in the logarithmic plot suggests a power low in k. Source: *Lecture on Turbulence by C.P. Dullemond, http://slideplayer.com/slide/3170127/*

This power law behaviour has been modelled by Kolmogorov [1941]. It is obtained from a discussion on the dimensionality of the energy spectrum. The total energy in the system can be computed as:

$$E = \int_0^\infty E\left(k\right) dk, \tag{2.3}$$

since the energy in Fourier space is conserved. Here $E\left(k\right)$ is the energy at the infinitesimal wave number range dk. Considering one unit of mass the dimensionality of $E\left(k\right)$ is one of the square of a velocity per unit of wave number. Since $v^2 \sim l^2 t^{-2}$, where l and t define the length and time units, and $k \sim l^{-1}$, $E\alpha\left(k\right)^3 t^{-2}$.

Since the regime is stationary, the constant rate of energy injected in the system,

ϵ, is equal to the rate of energy dissipated by the system, $\epsilon_\eta = \epsilon$. This is therefore equal to the transfer of energy from a certain k to $k + dk$ for all the values of k between injection and dissipation. In the inertial range the transfer of energy is proportional to the square of the velocity fluctuations associated with eddies over the time it takes for the energy to transfer to smaller scales:

$$\epsilon \sim \frac{(\delta v_I)^2}{\tau_I}, \tag{2.4}$$

where δv_i is the velocity fluctuation and τ_I is the time required to transfer the energy.

The unit of ϵ is energy per unit time, i.e. $l^2 t^{-3}$. $E(k)$ is a function of the energy transferred and of the wave number:

$$E(k) = f(\epsilon, k). \tag{2.5}$$

Since ϵ does not depend on k, as explained earlier in this paragraph, and it is the only variable containing the time unit as t^{-3} it needs to appear with exponent 2/3 to match the time unit on the LHS t^{-2}. We can therefore rewrite

$$E(k) = \epsilon^{2/3} g(k), \tag{2.6}$$

where $\epsilon^{2/3}$ has units $(l^2 t^{-3})^{2/3} = l^{4/3} t^{-2}$. Now we require the length dimensions to be equal between RHS and LHS. Since $E(k)$ is energy per unit of wave number, its dimensions are $l^3 t^{-2}$. To obtain l^3 in the RHS we must multiply $l^{4/3}$ in $\epsilon^{2/3}$ times $l^{5/3}$. Since $g(k)$ depends only on k, which has unit l^{-1}, $g(k) \sim k^{-5/3}$, therefore:

$$E(k) \sim \epsilon^{2/3} k^{-5/3} \tag{2.7}$$

states that the power spectrum has a dependence on k as a power law with exponent $-5/3$. This has been confirmed by observations (see next section) and it is recognized as a universal law of hydrodynamics within the inertial sub-range.

2.2 Kraichnan model of turbulence

Kolmogorov's model of turbulence does not include the presence of a magnetic field and it is restricted to hydrodynamics. Kraichnan [1965] derived a theory valid for MHD following a procedure similar to the one used by Kolmogorov. In magneto-hydrodynamics the laws governing the motion of the fluid are similar to those of hydrodynamics, but due the presence of electromagnetic fields the Lorentz force has

to be added in the force balance. This generates MHD waves which can interact between each other, therefore transferring energy to each other.

Kraichnan assumed that the interaction between Alfvén waves with different wave numbers is responsible of the MHD turbulent cascade. An Alfvén wave is a low frequency oscillation of ion and magnetic fields where the movement (inertia) of the ions is balanced by the restoring force provided by the magnetic field. Defining the Alfvén velocity as:

$$v_A = \frac{B}{\sqrt{\mu_0 n_i m_i}}, \tag{2.8}$$

where B is the intensity of the magnetic field, n_i is the ions number density and m_i is the ions mass, the dispersion relation of an Alfvén wave is:

$$\omega^2 = k^2 v_A^2 cos^2\theta, \tag{2.9}$$

where θ is the angle between the direction of propagation and the magnetic field. These waves travel at a velocity:

$$v_{ph} = \frac{\omega}{k} = \pm v_A cos\theta. \tag{2.10}$$

The information is transported at the group velocity:

$$\boldsymbol{v}_g = \frac{\partial \omega}{\partial k} = v_A \boldsymbol{b}, \tag{2.11}$$

where $\boldsymbol{b}$ is the magnetic field unit vector.

The information can travel along the magnetic field's direction at $\pm v_A$. Therefore, for incompressible flow, only counter propagating waves can interact non linearly. We define the Alfvén time as:

$$\tau_A\left(l_\parallel\right) \sim \frac{l_\parallel}{v_A}, \tag{2.12}$$

where $l_\parallel$ is the characteristic length in the magnetic field direction. τ_A is the time that two counter propagating Alfvén wave packets take to pass through each other, ignoring a factor of 2 for anti-parallel waves. The strain time is given by:

$$\tau_s\left(l_\perp\right) \sim \frac{l_\perp}{\delta v_I}, \tag{2.13}$$

where $l_\perp$ is the characteristic length in the direction perpendicular to the magnetic field and δv_I is the velocity fluctuation associated with the eddies. Since $\frac{\delta v_I^2}{l_\perp}$is the

rate of variation of the velocity fluctuations, during τ_A the latter is:

$$\Delta\delta v_I \sim \frac{\delta v_I^2 \tau_A}{l_\perp} \sim \frac{\delta v_I \tau_A}{\tau_S}. \tag{2.14}$$

The variation is assumed to be very small compared to the fluctuation itself, therefore $\tau_A \ll \tau_S$. τ_I is the time it takes to change δv_I by an amount of the order of δv_I. If N is the number of wave interactions during τ_I then $\tau_I = N\tau_A$. Assuming the process to be Markovian the change in N interactions is proportional to $\sqrt{N} = \sqrt{\frac{\tau_I}{\tau_A}}$:

$$\sum^{\tau_I} \Delta\delta v_I \sim \delta v_I \frac{\tau_a}{\tau_S}\sqrt{\frac{\tau_I}{\tau_A}} \sim \delta v_I. \tag{2.15}$$

Therefore:

$$\frac{\tau_a}{\tau_S}\sqrt{\frac{\tau_I}{\tau_A}} \sim 1. \tag{2.16}$$

Assuming isotropy, $l_\perp = l_\perp = l$:

$$\tau_I \sim \frac{\tau_S^2}{\tau_A} \sim \frac{v_A l}{\delta v_I^2}. \tag{2.17}$$

Recalling that the rate of energy cascade is defined as:

$$\epsilon \sim \frac{\delta v_I^2}{\tau_I}, \tag{2.18}$$

substituting for τ_I:

$$\delta v_I^2 \sim \epsilon \frac{v_A l}{\delta v_I^2}, \tag{2.19}$$

and rearranging and writing in terms of k:

$$\delta v_I \sim (\epsilon v_A)^{1/4} k^{-1/4}. \tag{2.20}$$

Since $E(k)$ is the energy per unit wave number,

$$E(k) \sim \frac{\delta v_I^2}{k} \sim (\epsilon v_A)^{1/2} k^{-3/2}, \tag{2.21}$$

which is the Kraichnan power law for MHD energy cascade. The exponent is slightly different from that found by Kolmogorov in hydrodynamics. However in some situations the Kolmogorov law can be applied to MHD. This happens when there is a balance between the linear Alfvén time scale and the non-linear time required to

transfer energy in the cascade, which is said to be critically balanced. In this situation, when the flow is perpendicular to the magnetic field the cascade has a power law with exponent $-5/3$. For flow parallel to the magnetic field the exponent is -2.

In the next section we will show some results from solar wind observations which have confirmed the Kolmogorov and Kraichnan laws. Then we will describe what happens at scales smaller than the inertial sub-range.

2.3 Solar wind observations of energy cascade

Turbulent phenomena in the solar wind have been observed starting from the first Mariner missions during the 1960s [Bruno and Carbone, 2013]. Coleman [1968] used data from Mariner 2 to first prove the existence of turbulent fluctuations. He showed that the solar wind is often turbulent, with phenomena happening over a broad range of frequencies. He found a power spectrum following a power law with exponent -1.2, different from the one expected by Kraichnan model.

Recently Podesta et al. [2007] found that the magnetic energy spectra followed an expected Kolmogorov $-5/3$ power law, while velocity spectra and kinetic spectra followed a Kraichnan $-3/2$ power law. This result has been confirmed by other authors [Salem et al., 2009] [Tessein et al., 2009].

Alexandrova et al. [2009] used data from Cluster spacecraft, gathered by instruments capable of capture spectra up to 300 Hz, to study the energy cascade at ion kinetic scales, which allowed the study of the magnetic power spectrum at kinetic ranges. While a Kolmogorov $-5/3$ power law has been found for MHD scales, at kinetic scales the cascade follows a -2.8 power law, which still does not have any theoretical explanation. Figure 2.2 shows the magnetic power spectrum as function of the frequency. Since frequency and wave number are linearly related the power spectrum as function of the wave number has the same exponent. From the figure it is possible to see the inertial range, where the power spectra follows a power law with exponent -1.7, a region of break after which, with increasing frequency, the exponent changes to -2.8 in the kinetic range. For smaller scales, where $k\rho_e \sim [0.1, 1]$ the cascade follows an exponential $\sim \exp\left(-\sqrt{k\rho_e}\right)$.

These results have been confirmed and extended in Sahraoui et al. [2010]. Here the authors found similar behaviour at ion inertial scales and kinetic scales, with a region of break following a power law of ~ -4.0. At smaller than ion kinetic scales a power law with exponent ~ -3.5 was found.

The break region between the ions inertial and kinetic scales, in which the cascade

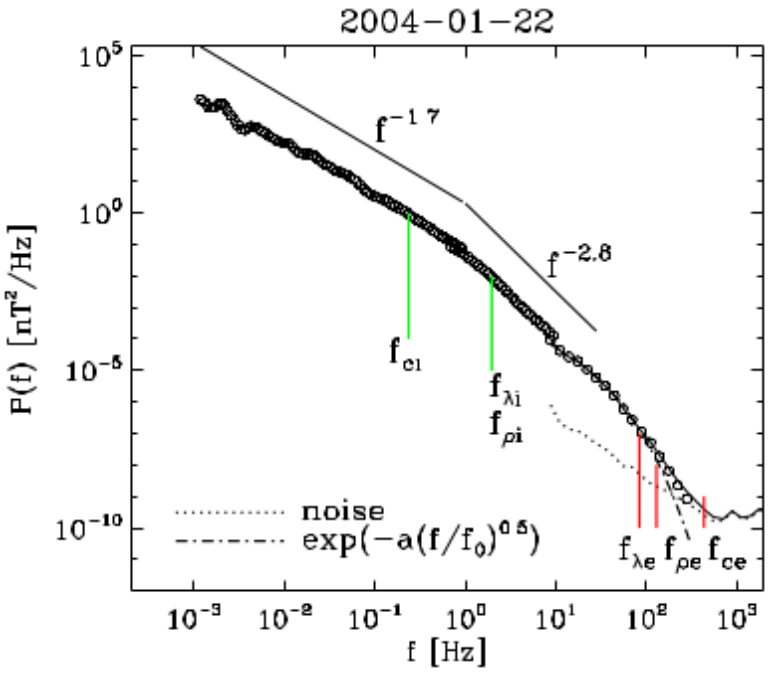

Figure 2.2: Magnetic power spectra in function of frequency. Measurements from three Cluster instruments. FGM (up to 1 Hz), STAFF-SC (up to 10 Hz), and STAFF- SA ($f > 8$ Hz, solid line: initial spectrum, open circles: spectrum after the noise subtraction). The vertical lines indicate the different plasma kinetic scales. Source: Alexandrova et al. [2009]

changes the exponent of the power law, has been confirmed by other authors, but the explanation to this physical phenomenon is still unclear [Bruno and Trenchi, 2014] [Chen et al., 2014].

In the next sections we will show how this problems have been studied computationally and the results which have been obtained with simulations. We remark that the problem of studying the energy cascade requires the ability to resolve both very large and very small scales at the same time. Therefore hybrid codes have been the ones more often employed, thanks to their ability to resolve ion kinetics over large regions of volume.

2.4 PIC-Hybrid simulations

Bi-dimensional and three-dimensional Particle in Cell hybrid simulations of the turbulent energy cascade have been recently carried out [Franci et al., 2015a,b, 2016a,b, 2017, 2018, Hellinger et al., 2017, Hellinger et al., 2015].

In a first set of direct numerical simulations Franci et al. [2015a,b] confirmed the

different scaling between magnetic and kinetic fluctuations in the inertial range and the existence of a break region in the magnetic power spectrum separating the MHD scale from the ion kinetic scale where a steeper power law has been found. Their 2D simulations were based on a Particle In Cell hybrid code making use of the *CAM-CL* approximation [Matthews, 1994] which we will describe in detail in the next chapter. The authors fixed $\beta_p = \beta_e = 0.5$, $n_p = n_e = 1$ and the temperature anisotropy ratio equals to 1 in all the domain. They ran a set of simulations varying cell size Δx, length of the box L, resistivity η and number of particles per cell (ppc), setting a constant magnetic field in the direction perpendicular to the simulation box. They imposed perturbations using a spectrum of linearly polarized magnetic and bulk velocity fluctuations with in-plane only components, exciting Fourier modes in the range of normalized k $0.2 < k_{x,y} < 0.2$ with equal amplitude and random phases.

Figure 2.3 shows that at $t = 200\Omega_p^{-1}$ the turbulence is fully developed. The picture shows 6 isocontour plots of different quantities at the same time step, for the more detailed run: the magnitude of the magnetic fluctuations,$|\boldsymbol{B}_\perp^2|$, in the top-left panel; the magnitude of the perpendicular velocity fluctuations, $|\boldsymbol{u}_\perp^2|$, in the top-right panel; the out of plane current density, $J_\parallel$ and vorticity, $\omega_\parallel$, in the middle- left and right panels respectively; the proton temperature variation to the initial temperature, $\Delta T_p/T_0$, in the bottom-left panel and the temperature anisotropy ratio, A_p in the bottom-right panel.

The figure shows the existence of coherent structures as vortices in both magnetic and velocity plots. However these have strong correlations in some regions and opposite correlations in others. $J_\parallel$ and $\omega_\parallel$ exhibit a similar behaviour, with peaks in the same regions and both forming a structure with many thin layers. The proton temperature is subjected to both positive and negative variations in contiguous regions. From the bottom right panel we can see that A_p varies in a broad range also in very narrow regions.

At the same time step the power spectra of magnetic and velocity fluctuations were computed. Figure 2.4 shows that they found agreement with observations in the inertial range with a $-5/3$ power law for the perpendicular magnetic fluctuations power spectrum and a $-3/2$ law for the velocity. This is followed by a break region which separates the inertial range to the ions kinetic range, where a -3 power law for the magnetic power spectrum has been found. This is very close to the observational result of -2.8. The noise produced from the initial distribution of particles is shown in light blue. The latter affects the power spectra partially only for very large values of k.

However, it is interesting to see how the variation of the perpendicular proton tem-

perature depends on the number of particles employed for the simulation. Figure 2.5 shows this dependence giving the value of $\Delta T_{p,\perp}/T_0$ for 5 different simulations with different number of particles , ranging from 500 to 8000 ppc. While there is a good convergence to a value of 3.4%, for small numbers of particles per cell the variation of perpendicular temperature increases noticeably. This remarks the dependency of the proton heating and therefore of temperature anisotropies on the initial noise. We believe that 8000 ppc is probably an order of magnitude greater that used for most PIC simulations.

In a subsequent work Franci et al. [2016b] performed a set of run varying the plasma beta. They found (see Fig. 2.6) that the position of the break moves towards lower k when β increases. Also, while the power law has similar exponent in all the runs for the inertial range, in the kinetic range it is much steeper for lower values of β. The break shape is therefore sharper at low values of β.

The presence of a break in the power spectra has been related to magnetic reconnection [Franci et al., 2017]. The latter is a phenomenon which happens when regions with magnetic fields in opposite directions stream towards each other. The magnetic topology is then rearranged: the magnetic field lines are broken and reformed by a composition of the lines coming from the two regions. These new field lines then stream away from the point where reconnection happens, called the X point. Here the perpendicular magnetic field vanishes and a parallel electric field is generated. Reconnection converts magnetic energy into kinetic energy, thermal energy, and particle acceleration.

The authors found that following an injection of energy in the inertial range, when magnetic reconnection starts occurring there is a transfer of energy straight to ion kinetic ranges of k. From here a power law -2.8 develops even before the turbulent cascade is fully evolved. The exponents of $-5/3$ and -2.8 for inertial and kinetic ranges have been recently confirmed by 3D simulations [Franci et al., 2018] make use of *CAMELIA* (Current Advance Method Et cycLIc leApfrog) code. The authors were capable of carrying out simulations on 512^3 grid points with simulation box length $L = 128d_i$ and 2048 particles per cell. The limit on the particles per cell in 3D is reduced due to the increase in the number of cells.

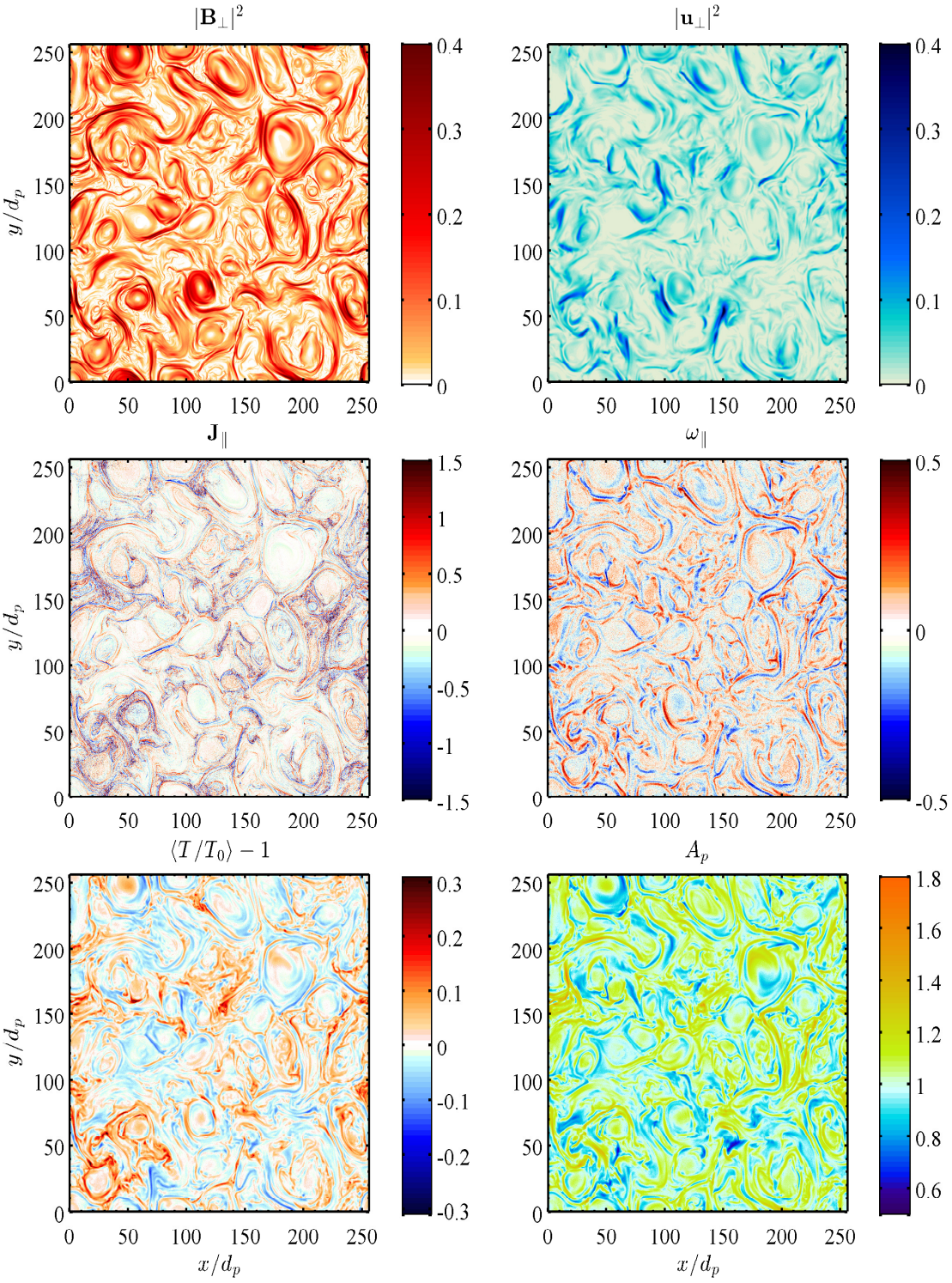

Figure 2.3: Isocontours at $t = 200\Omega_p^{-1}$. Magnitude of the perpendicular velocity fluctuations, $|\boldsymbol{u}_\perp^2|$, in the top-right panel; out of plane current density, $J_\parallel$ and vorticity, $\omega_\parallel$, in the middle- left and right panels respectively; proton temperature variation to the initial temperature, $\Delta T_p/T_0$, in the bottom-left panel and temperature anisotropy ratio, A_p in the bottom-right panel. Source: Franci et al. [2015a]

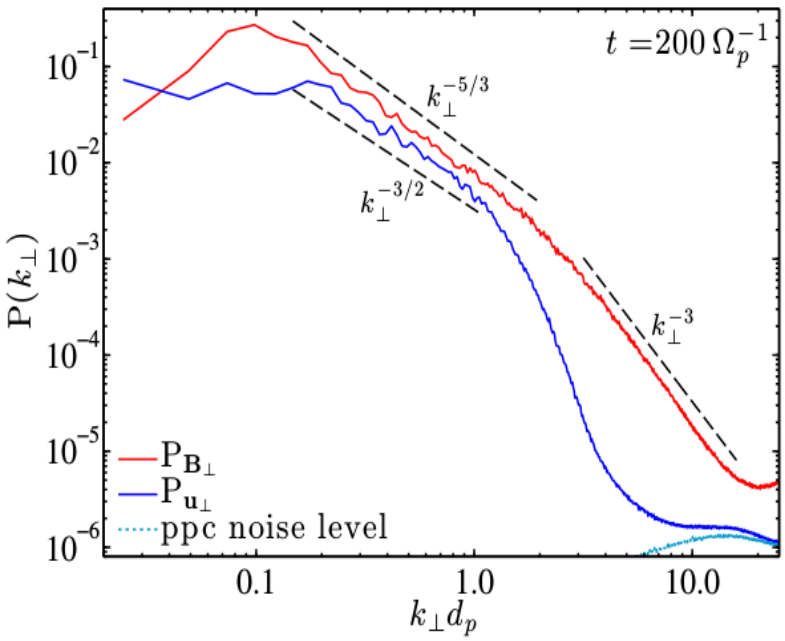

Figure 2.4: Power spectra of the perpendicular magnetic (red solid line) and velocity (blue solid line) fluctuations at $t = 200\Omega_p^{-1}$. Source: Franci et al. [2015a]

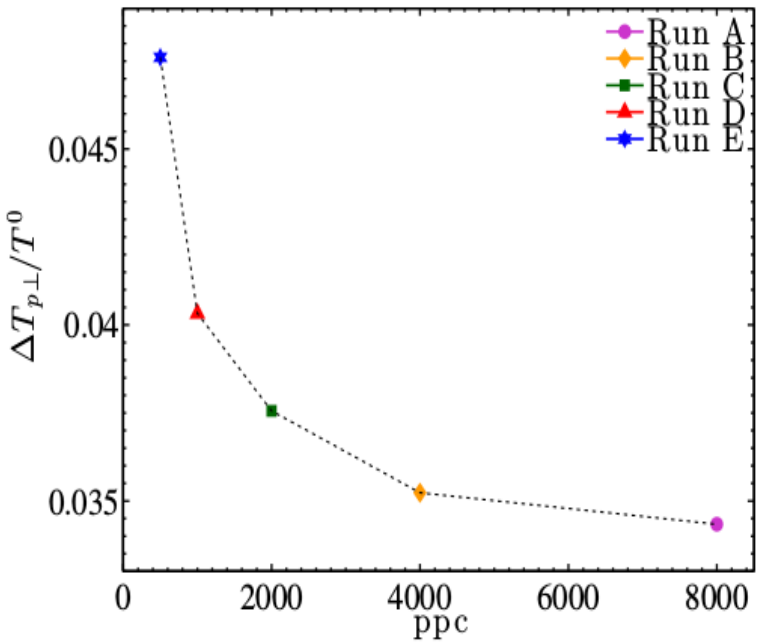

Figure 2.5: Perpendicular proton heating, $\Delta T_{p,\perp}/T_0$, at $t = 200\Omega_p^{-1}$ in function of the number of particles per cell employed, ranging from 8000 (Run A) to 500 (Run E). Source: Franci et al. [2015a]

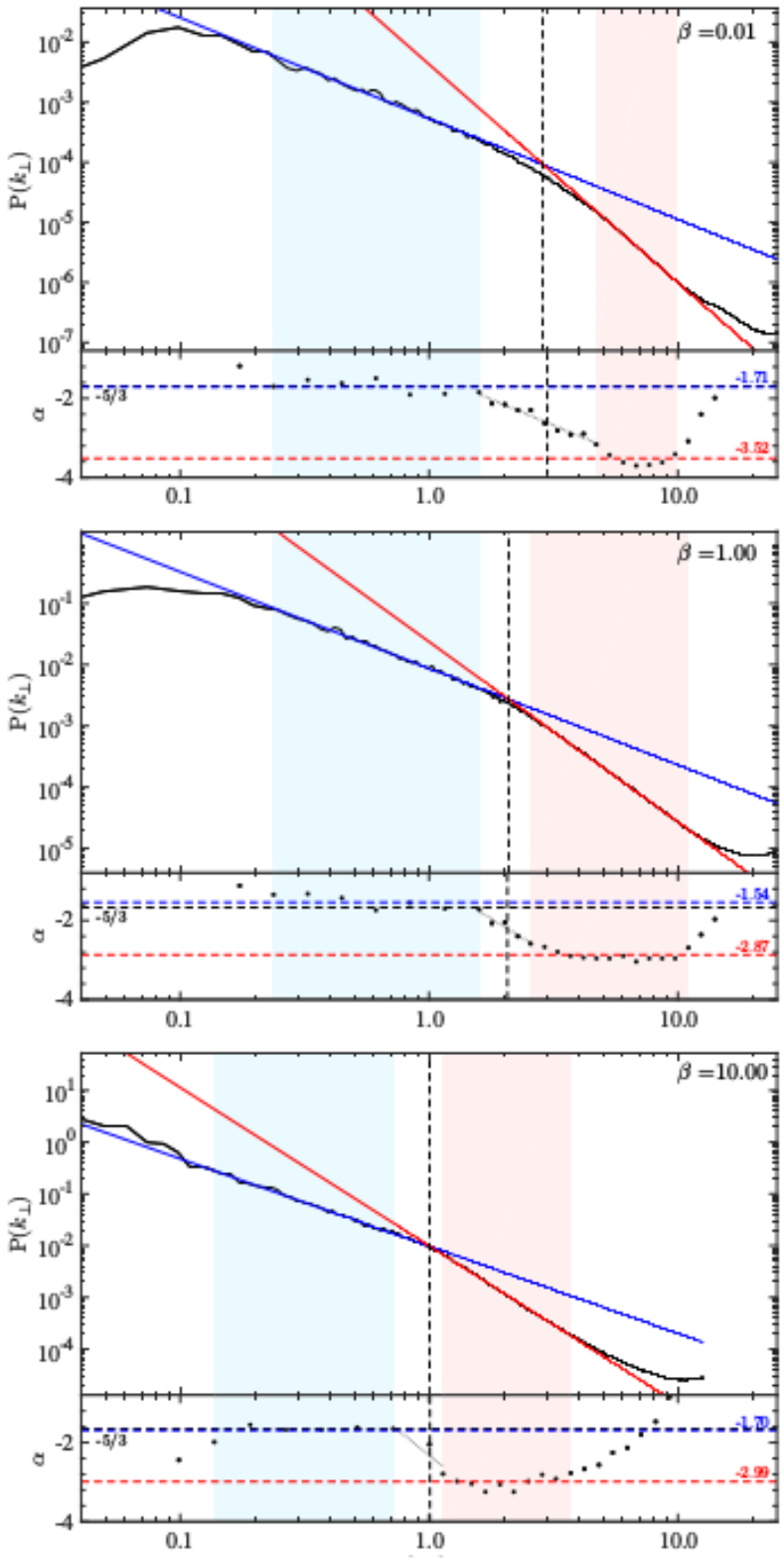

Figure 2.6: Global fits of the power spectra of magnetic field fluctuations for three different values of plasma beta: $\beta = 0.01$ in the top panel, $\beta = 1$ in the middle panel, $\beta = 10$ in the bottom panel. The global fits were performed in the inertial range (blue lines and light blue regions) and in the ions kinetic range (red lines and light red regions). The intersection point defines the break position. Source: Franci et al. [2016b]

2.5 Vlasov-Hybrid simulations

The turbulent energy cascade also has been studied by solving the Vlasov-Maxwell system of equations coupled with electrons momentum equation in Vlasov-Hybrid simulations described in the introduction [Cerri et al., 2017, 2018, Cerri et al., 2017, Servidio et al., 2012, 2014, 2015, Sorriso-Valvo et al., 2018]. These kind of simulations are capable of reducing the initial particle noise approximating directly the distribution function in a discretized 6-dimensional phase space, without performing any particle positioning through random number generation.

Servidio et al. [2012] carried out simulations on a 2D3V geometry (two dimensions in physical space and three in velocity space), using a massless electron fluid. The mean magnetic field is oriented in the direction perpendicular to the simulation box. They perturbed a Maxwellian plasma initial condition with a 2D spectrum of Fourier modes for perpendicular components of magnetic field and ions velocity. They chose an artificial value for the resistivity of $\eta \sim 10^{-2}$. This does not mimic any particular plasma behaviour but just acts to reduce numerical instabilities at large k.

The authors carried out 3 runs varying the amplitude of the perturbations and the sizes of the simulation box, therefore obtaining different times for the turbulence to develop. Figure 2.7a shows isocontours of the parallel current j_z and the magnetic potential of the in plane magnetic field a_z, where $\boldsymbol{b}_\perp = \nabla a_z \times \boldsymbol{z}$, where $\boldsymbol{z}$ is the unit vector in the z direction, after the turbulence is fully developed. The X points are marked with black crosses and these are the places where reconnection happens. Figure 2.7b reports the power spectra of magnetic field, ions bulk velocity, electric field and ions density as a function of the normalized wave number. In the inertial length the expected Kolmogorov $-5/3$ power law is found. We can see that the magnetic power spectra is not flattened in the inertial range and in the ion kinetic range it does not follow a power law. This might be due to the artificial resistivity which does not correspond to any physical characteristic of the plasma.

More recently Cerri et al. [2017] extended the Vlasov-Hybrid sumulations to 3D3V geometry, including electron inertia effects. They achieved this using a generalized Ohm's law for the electron fluid described in Mangeney et al. [2002], Valentini et al. [2007] and reported in the next chapter. They imposed a proton to electron mass ratio of $m_p/m_e = 100$. They initialized the plasma with an isotropic Maxwellian proton distribution function and a mean field in the z direction, imposing random large scale 3D magnetic perturbations. They used 384^2 grid points in the xy plane and 64 in the parallel z direction, obtaining simulation box lengths of $10\pi d_i$ and

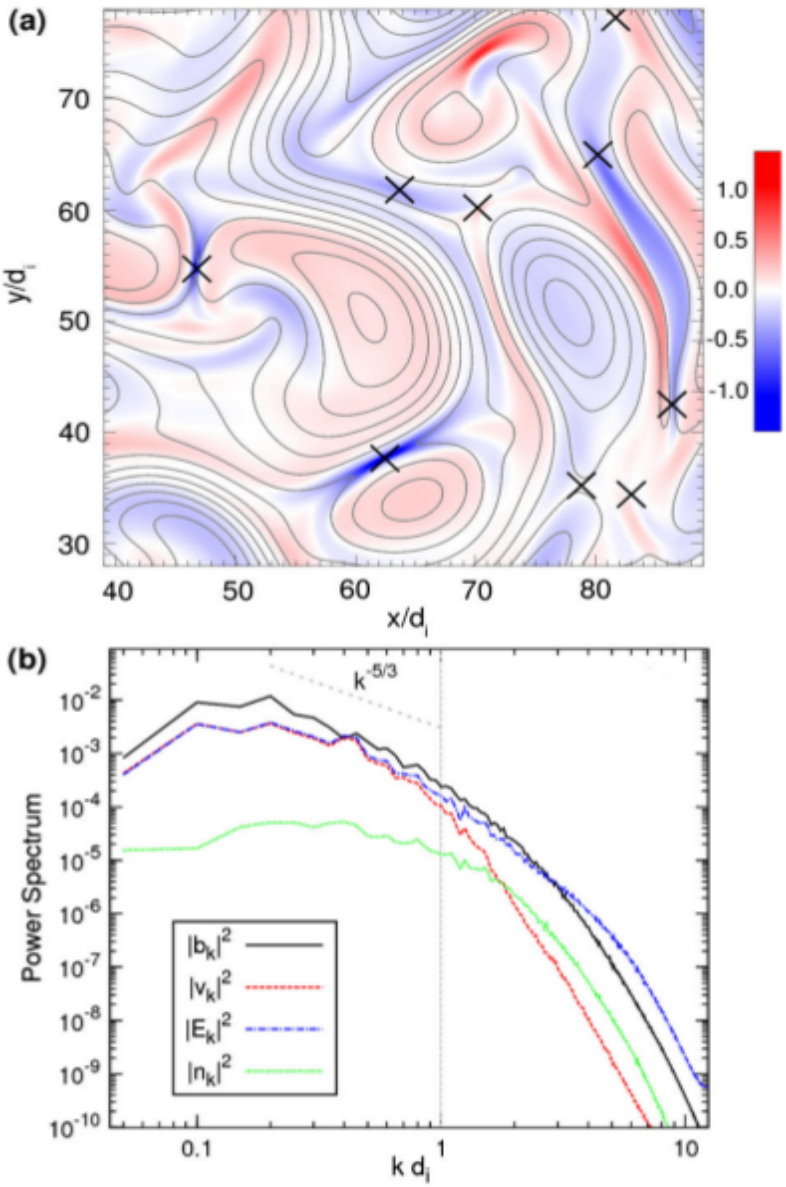

Figure 2.7: Top: zoomed isocontours of j_z and a_z isolines, and its X points (black crosses) after turbulence is developed. Bottom: Power spectra of magnetic field (black line), ions bulk velocity (red dashed line), electric field (blue dot-dashed line) and ions density (greend dotted line). The expected Kolmogorov power law is reported as reference (gray dashed line).Source: Servidio et al. [2012]

$2\pi d_i$ respectively. They performed 2 runs: one with $\beta = 1$ and the velocity domain ranging between $\pm 8 v_{th,i}$ using 61^3 points to discretize it, and one with $\beta = 0.2$ and the velocity domain ranging between $\pm 5 v_{th,i}$ using 51^3 points to discretize it. They assumed an anisotropic cascade. In Fig. 2.8 they show total magnetic energy spectra in the dual-phase space $(k_\parallel, k_\perp)$ for both runs:the $k_\parallel$ -averaged spectrum versus $k_\perp$

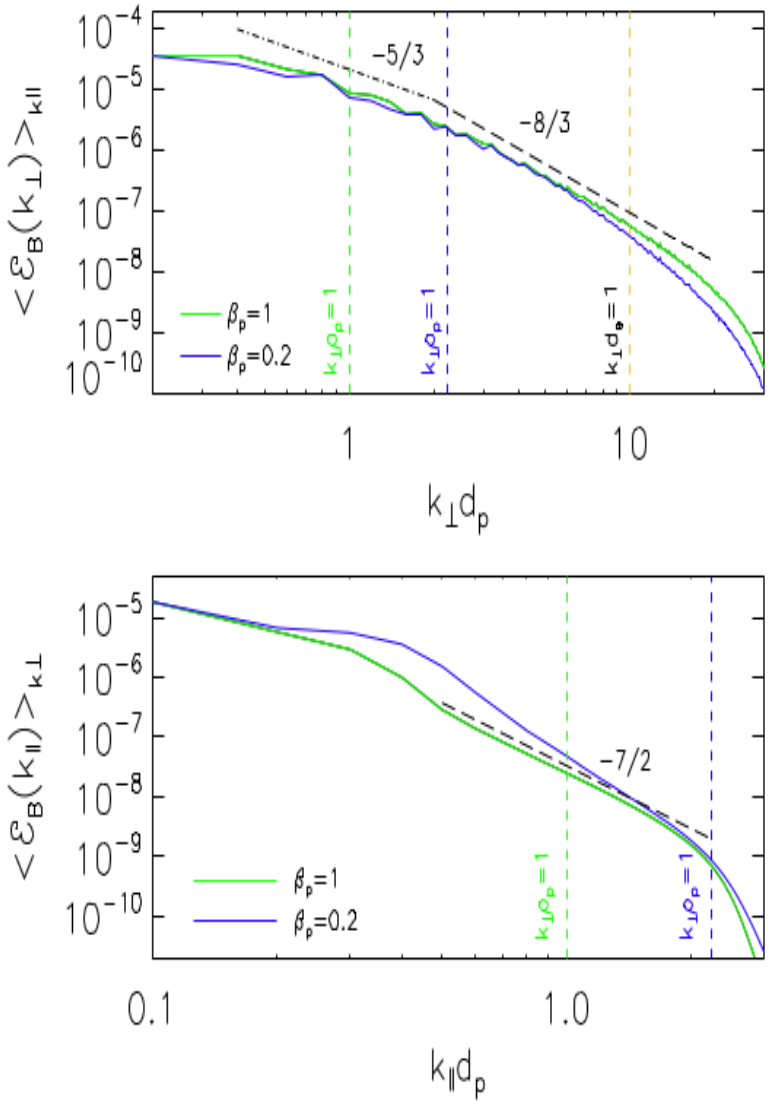

Figure 2.8: Top: total magnetic energy spectra in the dual-phase space $(k_\parallel, k_\perp)$ for both runs:the $k_\parallel$ -averaged spectrum versus $k_\perp$. Bottom: and the $k_\perp$ -averaged counterpart versus $k_\parallel$. $\beta = 1$ run in green, $\beta = 0.2$ run in blue.Source: Cerri et al. [2017]

(top frame), and the $k_\perp$ -averaged counterpart versus $k_\parallel$ (bottom frame). At large perpendicular scales we can see the cascades follows a nearly $-5/3$ power law for both cases. However in these simulations the inertial range is not studied extensively due to the limited sizes of the box. At bigger k a power law of $-8/3$ is found. No clear power law is found for small parallel wave numbers. For increasing values of $k_\parallel$ a $-7/2$ power law is found for the $\beta = 1$ case. These results are consistent with Boldyrev and Perez [2012] model of anisotropic turbulence.

The Vlasov-hybrid method is in principle better than particle in cell hybrid sim-

ulations because of the intrinsic absence of noise. However there are currently important differences in the results and it is not osbvious why. This might be because of the discretization in the velocity space which still does not employ enough grid points due to CPU and memory limitations of current calculators.

Summary

In this chapter we have given a brief summary of turbulence study and its application to space plasma, together with some recent observational and simulation results. This is not a complete review, but it shows the status of hybrid simulations for current research.

Many of the current results rely on PIC-hybrid simulations. The large dynamic range of turbulence suggest that Vlasov-hybrid methods would be appropriate, but current Vlasov-hybrid codes are still computational and memory expensive even for modern computers. Full 3D3V simulations cannot resolve both small and large scales due to these limitations. For this reason we think that the implementation of a spectral Vlasov-Hybrid code would improve the performance of these simulations, and this is the subject of our work described later.

3 Hybrid algorithms

In this chapter we will first give a description of traditional Particle in Cell hybrid algorithms. Then we will see some comparisons between the different methods using the codes we implemented starting from a Predictor Corrector. The term "hybrid" in plasma physics can refer to any simulation model in which one or more of the plasma species are treated as fluids, while the remaining species are treated kinetically as particles [Winske et al., 2003]. In space plasma applications electrons are traditionally modelled as a fluid, while ions are treated with a kinetic approach. This implies that the scales of interest fall between those obtained by magnetohydrodynamic simulations and those obtained with full PIC simulations.

One may wonder why we need this type of code. In the introduction we presented the canonical types of simulation approach available in plasma physics. We review them here with the goal of understanding why hybrid codes are widely used in space plasma simulations:

- Vlasov-Maxwell system of equations. In this case the solution is in terms of the distribution function, which is a function of 7 independent variables $f(\boldsymbol{x}, \boldsymbol{v}, t)$. If the discretization is made by 10^3 points in each direction we have 10^{18} unknown to solve for, for each time step. This is extremely memory and CPU expensive even for modern computers. For this reason Vlasov simulations are usually just 1D or 2D in space and restricted resolution in velocity space. Also, the velocity distribution usually has a large dynamic range and this leads to inefficiencies in the velocity discretization, with the possibility of mass loss through velocity space boundaries.

- Fluid - MHD. Moments of the distribution function are computed and a system of fluid equations for the macroscopic variables together with Maxwell equations for the fields is solved. For the derivation of the fluid system an equilibrium distribution function is assumed. Space plasmas are collisionless, but for the distribution function to be in equilibrium requires a collisional process to be happened. In this approach any kinetic effects associated with non-equilibrium distribution function are neglected.

- Particle-in-Cell. The plasma material is treated as a set of simulation particles with a distribution similar to the actual plasma particles. Each particle is moved in the simulation box applying the Lorentz force. Charge and current density are deposited at grid points and used to compute fields through Maxwell equations. Fields are then interpolated at the particle position and used to move the particles again. Since the proton to electron mass ratio $m_i/m_e = 1836$ the electron and ion kinetic scales differ by orders of magnitude. Space plasma simulations usually involve large regions of volume and to resolve the electron kinetics would require too many grid points, too many particles and too many time steps. In fact to follow electron movements implies to focus on very small length scales due to the small value of the electron Debye length. For explicit algorithms this implies short time steps due to stability criteria.

With hybrid codes some of the features of fluid simulations and of Particle-in-Cell, or Vlasov simulations are coupled. Treating electrons as a fluid lets us avoid resolving the electron gyroradius and frequency. Particle motion is solved only for ions which have gyroradius ~ 40 times and period 1836 times that of the electrons. Likewise for the Vlasov-Hybrid model the distribution function is solved only for the ion species for which phenomena happen in a much slower time scale than that of the electron one. This allows to use larger time steps and cell sizes, which implies larger simulation boxes. In space plasma physics, where the domains become very large this advantage of hybrid codes compared to classical kinetic simulations is fundamental and this is why the use of the former is so widespread.

3.1 Hybrid approximations and equations

The ion equations of motion for single particles are coupled with the electron momentum equation and Maxwell equations for electron fluid quantities and fields computations. Nevertheless there are some approximations which are typical and simplify these equations to the canonical system solved in hybrid algorithms.

The ion equations of motion are given by:

$$m_i \frac{d\boldsymbol{v}_p}{dt} = q_i \left(\boldsymbol{E} + \boldsymbol{v}_p \times \boldsymbol{B}\right) \tag{3.1}$$

$$\frac{d\boldsymbol{x}_p}{dt} = \boldsymbol{v}_p, \tag{3.2}$$

where fields are interpolated at particle position. Here $\boldsymbol{x}_p$ and $\boldsymbol{v}_p$ are position and velocity of each particle. The resistive coupling between electrons and ions has been here left off. This would have added a term $-e\eta\boldsymbol{J}$, where η is the resistivity, to the acceleration term.

In order to eliminate electron kinetic effects, the electrons are most often treated as a massless fluid (i.e., $m_e = 0$). Neglecting the resistive coupling between the electrons and ions again, the electron momentum equation reads:

$$-en_e\left(\boldsymbol{E} + \boldsymbol{v}_e \times \boldsymbol{B}\right) - \nabla \cdot \underline{\boldsymbol{P}}_e = 0, \tag{3.3}$$

where the pressure is in most cases approximated as a scalar: $\underline{\boldsymbol{P}}_e = p_e\underline{\mathbf{1}}$, where p_e is the isotropic electron pressure. This means that the electrons are an isotropic fluid. Typically an isothermal or adiabatic relation between pressure and temperature is assumed.

Since the effects of the electron Debye length are ignored, the plasma is considered quasi-neutral, i.e.:

$$en_e \simeq q_i n_i. \tag{3.4}$$

The electromagnetic fields are treated in the low frequency (Darwin) approximation so the displacement current is neglected in Ampère's law:

$$\nabla \times \boldsymbol{B} = \mu_0 \boldsymbol{J} = \mu_0 q_i n_i \left(\boldsymbol{v}_i - \boldsymbol{v}_e\right). \tag{3.5}$$

Faraday's law reads:

$$\frac{\partial \boldsymbol{B}}{\partial t} = -\nabla \times \boldsymbol{E}. \tag{3.6}$$

Ampère law is used to eliminate $\boldsymbol{v}_e$ in the electron momentum equation. Since the latter does not contain any time derivative, the electric field at a given time can be computed directly provided that we know the other variables at that time. The only quantities to be advanced are particles velocities and positions, and the magnetic field. Here we do not consider $\nabla \cdot \boldsymbol{B} = 0$. In fact it is easy to show that the latter is satisfied imposing the divergence of $\boldsymbol{B}$ vanishing as initial condition. We therefore use in 1D $B_x = const.$

3.2 Existing algorithms

The solution of hybrid equations is not as simple as it can seem. In fact, to advance all the quantities to the next time step some approximation is needed. In this

section we will first show this, illustrating the problem of hybrid algorithms. Then we will see how this problem is traditionally solved presenting different types of hybrid codes.

The particle positions and velocities are leapfrogged in time, so that positions and fields are known at full time step, N, while velocities are known at half time step, $N \pm 1/2$. The discretized ion equations of motion become:

$$\boldsymbol{v}_p^{N+\frac{1}{2}} = \boldsymbol{v}_p^{N-\frac{1}{2}} + \Delta t \frac{q}{m} \left(\boldsymbol{E}^N + \boldsymbol{v}_p^N \times \boldsymbol{B}^N \right) \tag{3.7}$$

$$\boldsymbol{x}_p^{N+1} = \boldsymbol{x}_p^N + \Delta t \boldsymbol{v}_p^{N+\frac{1}{2}}, \tag{3.8}$$

Provided that fields are known at time N, eq. (3.7) can be solved, noting that it is implicit in $\boldsymbol{v}_p^N$ which can be written as averages between velocities at half time steps. This equation can be solved using an energy preserving method such as Boris algorithm reported in Section 1.3.1.

The field's equations are solved explicitly in time. The magnetic field is advanced a half a time step using Faraday's law:

$$\boldsymbol{B}^{N+1/2} = \boldsymbol{B}^N - \frac{\Delta t}{2} (\nabla \times \boldsymbol{E}^N). \tag{3.9}$$

The electron momentum equation can then be solved for the electric field at time step $N + 1/2$:

$$\boldsymbol{E}^{N+1/2} = -\boldsymbol{v}_i^{N+1/2} \times \boldsymbol{B}^{N+1/2} - \frac{\nabla p_e^{N+1/2}}{q_i n_i^{N+1/2}} - \frac{\boldsymbol{B}^{N+1/2} \times \left(\nabla \times \boldsymbol{B}^{N+1/2} \right)}{q_i n_i^{N+1/2}}, \tag{3.10}$$

where positions at half time step are obtained as averages of positions at full time step. With the half time step electric field it is possible to again advance the magnetic field through Faraday's law:

$$\boldsymbol{B}^{N+1} = \boldsymbol{B}^{N+1/2} - \frac{\Delta t}{2} (\nabla \times \boldsymbol{E}^{N+1/2}). \tag{3.11}$$

The electric field at time step $N + 1$ is needed to advance the velocities. Using the electron momentum equation we need ion velocity at time step $N + 1$, which has not been computed yet. Here arises the problem of hybrid codes. To implement a good hybrid algorithm one has to find a good way to calculate an approximation of the electric field at the next time step.

In the literature, several different algorithms have been derived. We will focus here on the ones which we decided to implement and compare:

- *Predictor-Corrector*;
- *Current Advance Method and Cyclic Leapfrog*, CAM-CL;
- *Velocity extrapolation*.

In the following subsections we explain the different algorithms, noting that we implemented two similar versions of the CAM-CL. We will also show a CAM-CL algorithm which uses a Total Variation Diminishing (TVD) scheme for the spatial discretization of the magnetic induction equation. A TVD scheme is one where the total variation, i.e. $\sum_j |u_{j+1} - u_j|$ where the sum is over all the grid points and u is a general unknown, becomes smaller or stays equal every time step.

3.2.1 Predictor-Corrector

The Predictor-Corrector scheme [Harned, 1982] [Winske and Quest, 1986] is the first method historically introduced. Since the basic idea is very simple and it is proved to conserve energy in an adequate way, it is still widely used. The computation of the electric field at time step $N+1$ is performed in 4 main steps:

- The electric field is predicted through an extrapolation and it is used to compute a predicted magnetic field:

$$\boldsymbol{E'}^{N+1} = -\boldsymbol{E}^{N} + 2\boldsymbol{E}^{N+1/2}, \tag{3.12}$$

$$\boldsymbol{B'}^{N+1} = \boldsymbol{B}^{N+1/2} - \frac{\Delta t}{2}(\nabla \times \boldsymbol{E'}^{N+1}); \tag{3.13}$$

- The predicted fields are used to advanced particles and obtain predicted moments, $\boldsymbol{v'}_i^{N+3/2}$, $n_i'^{N+3/2}$;
- The predicted fields are advanced to $N + 3/2$:

$$\boldsymbol{B'}^{N+3/2} = \boldsymbol{B'}^{N+1} - \frac{\Delta t}{2}(\nabla \times \boldsymbol{E'}^{N+1}); \tag{3.14}$$

$$\boldsymbol{E'}^{N+3/2} = F(\boldsymbol{B'}^{N+3/2}, n_i'^{N+3/2}; \boldsymbol{v'}^{N+3/2}); \tag{3.15}$$

- A corrected electric fields at $N+1$ are computed as the average between that at $N+1/2$ and that predicted at $N+3/2$. This is used to advance the magnetic field:

$$\boldsymbol{E}^{N+1} = \frac{1}{2}(\boldsymbol{E}^{N+1/2} + \boldsymbol{E'}^{N+3/2}); \tag{3.16}$$

$$\boldsymbol{B}^{N+1} = \boldsymbol{B}^{N+1/2} - \frac{\Delta t}{2}(\nabla \times \boldsymbol{E}^{N+1}). \tag{3.17}$$

The advancement of the magnetic field might include substepping to improve accuracy at high frequency. The Predictor Corrector method involves two particle move for each time step. Since the particles' movement is the most computationally expensive part of a hybrid code, the method is expected to be somewhat slow when compared to algorithms which involve just one particle move per time step.

3.2.2 Current Advance Method and Cyclic Leapfrog (CAM-CL)

The Current Advance Method and Cyclic Leapfrog (CAM-CL) was first introduced by Matthews [1994]. We start here by describing the Current Advance Method. Consider the ion current density evaluated using velocities at the beginning of the time step and position at half time step. This is equivalent to neglecting the acceleration and only taking into account the transport of charge due to freely streaming particles, since the velocity of each particle has remained constant during the time interval $\Delta t/2$, whereas the particle position has changed. This current density is called the "free-streaming" current density. If $\phi(\boldsymbol{x}_s)$ is the weight given to the particle in the current collection procedure (see Introduction, Sect.(1.3.1)), depending on the position of the particle relative to the grid point where the current is being collected, we have:

$$\boldsymbol{J}_i^+ \left(\boldsymbol{x}^{1/2}, v^0\right) = \sum_s \phi\left(\boldsymbol{x}_s^{1/2}\right) q_s \boldsymbol{v}_s^0. \tag{3.18}$$

Now we proceed by deriving an equation for advancing $\boldsymbol{J}_i$ to the midpoint of the time-step. If we take the ion equation of motion used to push the particles at the first time step (i.e. the "pre-push" equation):

$$\boldsymbol{v}_p^{1/2} = \boldsymbol{v}_p^0 + \frac{\Delta t}{2}\frac{q_s}{m_s}\left(\boldsymbol{E}^* + \boldsymbol{v}^0 \times \boldsymbol{B}^{1/2}\right), \tag{3.19}$$

where $\boldsymbol{E}^* = \boldsymbol{E}\left(\rho_c^{1/2}, \boldsymbol{J}_i^0, \boldsymbol{B}^{1/2}, T_e\right)$, and we multiply the equation times q_s, sum the contributions of the terms at grid points, using weights $\phi_{sj}^{1/2} = \phi\left(\boldsymbol{x}_s^{1/2}, \boldsymbol{x}_j\right)$, i.e. the

weights due to species s at grid points $\boldsymbol{x}_j$ at time step $N + 1/2$, we have:

$$\sum_s \phi_{sj}^{1/2} q_s \boldsymbol{v}_s^{1/2} = \sum_s \phi_{sj}^{1/2} q_s \boldsymbol{v}_s^0 + \frac{\Delta t}{2} \sum_s \phi_{sj}^{1/2} \frac{q_s^2}{m_s} \left(\boldsymbol{E}^* + \boldsymbol{v}_s^0 \times \boldsymbol{B}^{1/2} \right), \tag{3.20}$$

which can be written as:

$$\boldsymbol{J}_i^{1/2} = \boldsymbol{J}_i^+ + \frac{\Delta t}{2} \left(\Lambda \boldsymbol{E}^* + \boldsymbol{\Gamma} \times \boldsymbol{B}^{1/2} \right), \tag{3.21}$$

where:

$$\Lambda = \sum_s \phi_{js}^{1/2} \frac{q_s^2}{m_s}, \tag{3.22}$$

$$\boldsymbol{\Gamma} = \sum_s \phi_{js}^{1/2} \frac{q_s^2}{m_s} \boldsymbol{v}_s^0. \tag{3.23}$$

The equation just obtained is used to advance the current in the computational cycle explained in the following, where we omit $N+$, indicating with 0 time step N and with $1/2$ time step $N + 1/2$:

- The magnetic field is advanced to $1/2$ and used to compute $\boldsymbol{E}^*$. The current is advanced to $1/2$ and used to compute $\boldsymbol{E}^{1/2}$:

$$\boldsymbol{B}^{1/2} = \boldsymbol{B}^0 - \int_0^{\Delta t/2} \nabla \times \boldsymbol{E} \left(\rho_c^0, \boldsymbol{J}_i^0, \boldsymbol{B}(t), T_e \right) dt \tag{3.24}$$

$$\boldsymbol{E}^* = \boldsymbol{E} \left(\rho_c^{1/2}, \boldsymbol{J}_i^0, \boldsymbol{B}^{1/2}, T_e \right) \tag{3.25}$$

$$\boldsymbol{J}_i^{1/2} = \boldsymbol{J}_i^+ + \frac{\Delta t}{2} \left(\Lambda \boldsymbol{E}^* + \boldsymbol{\Gamma} \times \boldsymbol{B}^{1/2} \right), \tag{3.26}$$

$$\boldsymbol{E}^{1/2} = \boldsymbol{E} \left(\rho_c^{1/2}, \boldsymbol{J}_i^{1/2}, \boldsymbol{B}^{1/2}, T_e \right); \tag{3.27}$$

- The particle positions and velocities are advanced for a time step:

$$\boldsymbol{v}_p^{1/2} = \boldsymbol{v}_p^0 + \frac{\Delta t}{2} \frac{q_s}{m_s} \left(\boldsymbol{E}^{1/2} + \boldsymbol{v}_p^0 \times \boldsymbol{B}^{1/2} \right), \tag{3.28}$$

$$\boldsymbol{v}_p^1 = \boldsymbol{v}_p^0 + \Delta t \frac{q_s}{m_s} \left(\boldsymbol{E}^{1/2} + \boldsymbol{v}_p^{1/2} \times \boldsymbol{B}^{1/2} \right), \tag{3.29}$$

$$\boldsymbol{x}_p^{3/2} = \boldsymbol{x}_p^{1/2} + \Delta t \boldsymbol{v}^1 \tag{3.30}$$

- The species' partial moments are collected:

$$n_s^{3/2} = \sum_s \phi\left(\boldsymbol{x}_s^{3/2}\right), \tag{3.31}$$

$$(\boldsymbol{nv})_s^{+} = \sum_s \phi\left(\boldsymbol{x}_s^{3/2}\right) \boldsymbol{v}_s^1 \tag{3.32}$$

$$(\boldsymbol{nv})_s^{-} = \sum_s \phi\left(\boldsymbol{x}_s^{1/2}\right) \boldsymbol{v}_s^1 \tag{3.33}$$

- The partial moments are multiplied times particle charge (squared) and divided by particle mass and summed over species to obtain:

$$\rho_c^{3/2} = \sum_s q_s n_s^{3/2} \tag{3.34}$$

$$\boldsymbol{J}_i^{+/-} = \sum_s q_s \left(\boldsymbol{nu}\right)_s^{+/-} \tag{3.35}$$

$$\Lambda = \sum_s \frac{q_s^2}{m_s} n_s^{3/2} \tag{3.36}$$

$$\boldsymbol{\Gamma} = \sum_s \frac{q_s^2}{m_s} \left(\boldsymbol{nu}\right)_s^{+/-} \tag{3.37}$$

- The density, current and Γ at next time step are obtained as averages and magnetic field is advanced to the full time step:

$$\rho_c^1 = \frac{1}{2}\left(\rho_c^{1/2} + \rho_c^{3/2}\right) \tag{3.38}$$

$$\boldsymbol{J}_i^1 = \frac{1}{2}\left(\boldsymbol{J}_i^{-} + \boldsymbol{J}_i^{+}\right) \tag{3.39}$$

$$\boldsymbol{\Gamma}_i^1 = \frac{1}{2}\left(\boldsymbol{\Gamma}_i^{-} + \boldsymbol{\Gamma}_i^{+}\right) \tag{3.40}$$

$$\boldsymbol{B}^1 = \boldsymbol{B}^{1/2} - \int_{\Delta t/2}^{\Delta t} \nabla \times \boldsymbol{E}\left(\rho_c^1, \boldsymbol{J}_i^1, \boldsymbol{B}(t), T_e\right) dt \tag{3.41}$$

In the equations for the magnetic field advancement we kept the expression of the time integral. This has to be substituted by the Cyclic Leapfrog scheme. In this particular time integration scheme the integration interval is subdivided in n substeps. The magnetic field is advanced in two different solutions. The first one updates the magnetic field of a substep and it is used to calculate the electric field

after a substep. This electric field is used to advance the second solution of two substeps. It is then possible to use the second solution to compute the electric field after two substeps and use it to advance the first solution to the third substep. This operation of leapfrog is repeated until the second solution reaches the full time step and the first is then advanced for the remaining substep (or vice versa depending whether n is odd or even). The final magnetic field is given by the average of the two solutions. The latter, together with density and current density, allows the calculation of the electric field.

We implemented an alternative version of the CAM-CL which, instead of computing densities and velocities at full time step as averages, collects them directly, moving the particle positions and velocities of half time step at a time. As we show in the last section of this chapter this produces very few changes, while the computational time is larger.

3.2.3 Velocity extrapolation

In this method [Fujimoto, 1991] the electric field is advanced to time level $N+1$ with an extrapolation of the ion flow velocity (or the ion current density) from $N+1/2$ to $N+1$. The velocity at time step $N+1$ is the only unknown quantity needed to evaluate directly $\boldsymbol{E}^{N+1}$ with the electron momentum equation. The extrapolation can be done in several ways. The simplest example is by using the saved values $\boldsymbol{v}_i^{N-1/2}$ and $\boldsymbol{v}_i^{N+1/2}$:

$$\boldsymbol{V}_i^{N+1} = \frac{3}{2}\boldsymbol{v}_i^{N+1/2} - \frac{1}{2}\boldsymbol{v}_i^{N-1/2}. \tag{3.42}$$

If one desires to improve the accuracy it is possible to keep also $\boldsymbol{v}_i^{N-3/2}$ to obtain a 4th order Adams-Bashford extrapolation:

$$\boldsymbol{v}_i^{N+1} = 2\boldsymbol{v}_i^{N+1/2} - \frac{3}{2}\boldsymbol{v}_i^{N-1/2} + \frac{1}{2}\boldsymbol{v}_i^{N-3/2}. \tag{3.43}$$

Although this method is very intuitive, the implementation requires the copy of several values, so that it performs slower than the CAM-CL as we show in the last section of this chapter.

3.2.4 CAM-CL with TVD spatial discretization

Finite volume method is not so widely used for hybrid codes as finite difference methods, but they have been proposed as an efficient method for global-scale hybrid simulations [Matsumoto et al., 2012] with good accuracy for systems with propagat-

ing gradients or with strong fluxes. In my test case the hybrid time advancement used is identical to CAM-CL, while the magnetic field is advanced following the procedure described in Matsumoto et al. [2012]. The magnetic induction equation is obtained substituting the electron momentum equation into Faraday's law, making use of Ampere's law in the Darwin approximation. It reads:

$$\frac{\partial \boldsymbol{B}}{\partial t} = \nabla \times \boldsymbol{v}_i \times \boldsymbol{B} + \frac{\nabla p_e}{2n} - \frac{1}{n}(\nabla \times \boldsymbol{B}) \times \boldsymbol{B} \,, \tag{3.44}$$

where the magnetic field is normalized by some reference value, the velocity is normalized by the Alfvén velocity and the pressure by the magnetic pressure. The convective part of the equation (first term) is treated with a finite volume approach, using the Total Variation Diminishing method by Harten and Yee described in Yee [1989], while the other terms are discretized with a central difference scheme. If we consider only the convective part of the RHS of equation (3.44), in the mono dimensional case, the equation is a hyperbolic conservation law of the form:

$$\frac{\partial \boldsymbol{Q}}{\partial t} + \frac{\partial \boldsymbol{F}}{\partial x} = 0, \tag{3.45}$$

where $\boldsymbol{Q} = (B_y, B_z)'$ and $\boldsymbol{F} = (v_x B_y - v_y B_x, v_x B_z - v_z B_x)'$. Here we explain the time advancement of the equation for a forward Euler scheme, for the sake of simplicity. However, in the code we chose to implement a third order Runge-Kutta scheme.

The system in Eq.(3.45) can be treated as two different scalar equations, which discretized take the form:

$$Q_j^{N+1} = Q_j^N - \frac{\Delta t}{\Delta x}\left(\tilde{F}_{j+1/2}^N - \tilde{F}_{j-1/2}^N\right), \tag{3.46}$$

where Q_j^N is the numerical approximation of B_y or B_z at $x = j\Delta x$ and $t = N\Delta t$ and $\tilde{F}$ is a numerical flux vector. Following Harten and Yee TVD approach, the numerical flux is given by:

$$\tilde{F}_{j+1/2} = \frac{1}{2}\left(F_{j+1} + F_j + \phi_{j+1/2}\right), \tag{3.47}$$

where:

$$\phi_{j+1/2} = \sigma\left(c_{j+1/2}\right)(g_j + g_{j+1}) - \psi\left(c_{j+1/2} + \gamma_{j+1/2}\right)\Delta_{j+1/2}, \tag{3.48}$$

$$g_j = minmod\left(\Delta_{j+1/2}, \Delta_{j-1/2}\right) \tag{3.49}$$

$$minmod\,(x, y) = sgn\,(x) \cdot max\;0, min\,[|x|, ysgn(x)] \tag{3.50}$$

$$\gamma_{j+1/2} = \sigma\left(c_{j+1/2}\right) \begin{cases} \frac{g_{j+1}-g_j}{\Delta_{j+1/2}} & \Delta_{j+1/2} \neq 0 \\ 0 & \Delta_{j+1/2} = 0 \end{cases} \tag{3.51}$$

$$\sigma\left(z\right) = \frac{1}{2}\left(\psi\left(z\right) - \frac{\Delta t}{\Delta x} z^2\right), \tag{3.52}$$

$$\psi(z) = \begin{cases} |z| & |z| \geq \delta \\ \left(z^2 + \delta^2\right)/2\delta & |z| < \delta. \end{cases} \tag{3.53}$$

In the previous equations $c_{j+1/2}$ indicates the characteristic velocity and is equal to $v_{x,j+1/2}$. $\Delta_{j+1/2}$ is defined as $\Delta_{j+1/2} = Q_{j+1} - Q_j$ and δ is a small positive parameter.

The algorithm just described should limit numerical instabilities and non-physical oscillations.

3.3 Hybrid algorithms with electron finite mass

Electron inertia should be included in hybrid codes when the spatial scales of interest are a small fraction of the ion inertial length, but greater than the electron gyroradius [Winske et al., 2003]. This allows us to study high frequency whistler wave propagation. The latter is a right hand circularly polarized wave which continues from the Alfvén wave above the ion cyclotron frequency, Ω_i. This wave propagates until the electron cyclotron frequency, Ω_e. Therefore the inclusion of phenomena at small spatial scales implies the inclusion of high frequency perturbations, where the highest frequency depends on $\Omega_e = \frac{eB}{m_e}$. The value of Ω_e increases with increasing ion to electron mass ratios. Large ion to electron mass ratios imply higher frequencies phenomena in the plasma, consequently the need of smaller time step. For this reason a real $\frac{m_i}{m_e} = 1836$ is very limiting on the time step and authors frequently use a smaller ratio.

In the history of hybrid codes there have been different methods to deal with the case $m_e \neq 0$. In the following we will first present briefly some of the approaches coming from different authors at different times, then we will give some examples in which the methods have been used. For a more detailed explanation the following can be consulted: Hewett and Nielson [1978], Swift [1996], Lipatov [2001], Cheng et al. [2013], Hesse and Winske [1994], and Hesse et al. [1995], Valentini et al. [2007], Muñoz et al. [2017].

The first approach we will consider has been developed by Hewett and Nielson [1978]. The electron current density is separated into longitudinal (curl-free) and

transverse (div-free) components. Summing electron and ion momentum equations, an equation for the total current is obtained. Taking the divergence of this equation and using quasi neutrality, which from charge continuity equation implies $\nabla \cdot \boldsymbol{J} = 0$, one can obtain an equation for the longitudinal electric field. The longitudinal part of the electron current density can be expressed as a scalar potential, $\boldsymbol{J}_{e,l} = -\nabla V$, since it is curl-free. Taking the divergence of this expression a Poisson equation is obtained:

$$\nabla^2 V = -\nabla \cdot \boldsymbol{J}_{e,l} = -\nabla \cdot \boldsymbol{J}_e = \nabla \cdot \boldsymbol{J}_i. \tag{3.54}$$

The transverse electron current density is advanced in time by direct evaluation of the electron momentum equation to find $\dot{\boldsymbol{J}}_e$, which is used to advance $\boldsymbol{J}_{e,t}$ in time using a second order time scheme. The evaluation of the electron momentum equation involves the computation of the divergence of the kinetic energy tensor. Doing so a shifted Maxwellian distribution is assumed for the electrons, where the temperature is obtained by time advance of the thermodynamic relation for the specific entropy. To calculate fields the electric field is subdivided into longitudinal and transversal parts and the transversal part of the displacement current is neglected. Maxwell's equation are solved in the Coulomb gauge:

$$\nabla^2 \Phi = -\frac{e}{\epsilon_0} \left(n_i - n_e \right), \tag{3.55}$$

$$\nabla^2 \boldsymbol{A} = -\mu_0 \boldsymbol{J}_t, \tag{3.56}$$

$$\nabla^2 \boldsymbol{E}_t = \mu_0 \dot{\boldsymbol{J}}_t, \tag{3.57}$$

where

$$\boldsymbol{B} = \nabla \times \boldsymbol{A}, \tag{3.58}$$

$$E_l = -\nabla \Phi, \tag{3.59}$$

and

$$\boldsymbol{J}_t = \boldsymbol{J} + \epsilon_0 \frac{\partial \boldsymbol{E}_l}{\partial t} \tag{3.60}$$

Alternatively Φ can be calculated taking the divergence of the sum of electron and ion momentum equations:

$$\nabla \cdot (\mu \nabla \Phi) = \nabla \cdot \left(\boldsymbol{D} + \mu \boldsymbol{E}_t + \boldsymbol{\xi} \times \boldsymbol{B} \right), \tag{3.61}$$

where

$$\mu = \mu_0 n \left(\frac{1}{m_i} + \frac{1}{m_e} \right), \tag{3.62}$$

$$\xi = \frac{\mu_0}{c}\left(\frac{\boldsymbol{J}_i}{m_i} - \frac{\boldsymbol{J}_e}{m_e}\right), \tag{3.63}$$

$$\boldsymbol{D} = \frac{1}{\sqrt{4\pi\epsilon_0}}\left(\boldsymbol{K}_i + \boldsymbol{K}_e\right), \tag{3.64}$$

where $\boldsymbol{K}_i$ and $\boldsymbol{K}_e$ are the divergences of ion and electron kinetic energy tensors:

$$\boldsymbol{K}_e = -q\nabla \cdot \int \boldsymbol{v}\boldsymbol{v} f_e d^3v, \tag{3.65}$$

$$\boldsymbol{K}_i = -q\nabla \cdot \int \boldsymbol{v}\boldsymbol{v} f_i d^3v, \tag{3.66}$$

and depends on the model used for the distribution function. In 2D Eq. (3.61) is solved using an alternating direction implicit method which eliminates the stability constraints.

The computation of the magnetic field is accomplished using Eq. (3.56) and Eq. (3.58).

Hesse and Winske [1994] developed an approach to partially deal with finite electron mass. They demonstrated that dissipation effects on ion scales can be included through the use of a detailed model for the full electron pressure tensor, and that reconnection does occur due to this effect. The electric field is obtained from the full electron momentum equation:

$$\boldsymbol{E} = -\boldsymbol{v}_i \times \boldsymbol{B} - \frac{1}{en_e}\left(\boldsymbol{J} \times \boldsymbol{B} - \nabla \cdot \bar{\bar{P}}_e\right) + \eta\boldsymbol{J} - \frac{m_e}{e}\frac{d\boldsymbol{v}_e}{dt}, \tag{3.67}$$

where $\bar{\bar{P}}_e$ is the electron pressure tensor. They first assumed that the electrons are a massless fluid and they set the resistivity to zero in the collisionless approximation, so the last two terms of Eq. (3.67) are dropped. In this way it is not possible to simulate reconnection (unless it arises because of some numerical dissipation) in the two-dimensional configuration used with a scalar pressure model. In fact reconnection is driven by E_z and with a scalar pressure model there are no z spatial derivatives. At the X point, where reconnection occurs $\boldsymbol{B} = 0$, so one finds $E_z = 0$ hence no reconnection is possible. Thus the electric field contribution is considered from the full electron pressure tensor, the evolution of which is determined by the following equation:

$$\frac{\partial \bar{\bar{P}}_e}{\partial t} = -\boldsymbol{v}_e\cdot\nabla\bar{\bar{P}}_e - \bar{\bar{P}}_e\nabla\cdot\boldsymbol{v}_e - \bar{\bar{P}}_e\cdot\nabla\boldsymbol{v}_e - \left(\bar{\bar{P}}_e\cdot\nabla\boldsymbol{v}_e\right)^T - \frac{e}{m_e}\left[\bar{\bar{P}}_e \times \boldsymbol{B} + \left(\bar{\bar{P}}_e \times \boldsymbol{B}\right)^T\right] - \nabla\cdot\bar{\bar{Q}}, \tag{3.68}$$

$\bar{\bar{Q}}$ denotes the generalized flux tensor, which is ignored. Eq. (3.68) contains explicitly the contributions of electron cyclotron dynamics, in squared brackets. These terms introduce high-frequency electron effects and tend to isotropize the electron distribution function, reducing the off-diagonal terms of the pressure tensor. They are replaced by a heuristic isotropization ansatz which takes into account the possibility of electron anisotropy-driven instabilities which can reduce the electron anisotropies. Eq. (3.68) is rewritten in the form:

$$\frac{\partial \bar{\bar{P}}_e}{\partial t} = -\boldsymbol{v}_e \cdot \nabla \bar{\bar{P}}_e - \bar{\bar{P}}_e \nabla \cdot \boldsymbol{v}_e - \bar{\bar{P}}_e \cdot \nabla \boldsymbol{v}_e - \left(\bar{\bar{P}}_e \cdot \nabla \boldsymbol{v}_e\right)^T - \frac{\Omega_e}{\tau}\left(\bar{\bar{P}}_e - p\bar{\bar{1}}\right), \quad (3.69)$$

where $p = Tr(\bar{\bar{P}}_e)/3$ is the isotropic part of the electron pressure tensor, $\bar{\bar{1}}$ is the unity tensor and τ represents a dimensionless isotropization time scale which is initially chosen equal to 100, resulting in a modest isotropization rate.

In a subsequent paper, Hesse et al. [1995] use the same approach, but electron cyclotron terms are retained. The equation for the pressure tensor is solved implicitly on ion time scales. The first four terms on the RHS of Eq. (3.68) are included in a time-centred fashion, while the cyclotron term is computed as an average of its value for the past and time-advanced electron pressure tensor. The resulting matrix equation is then solved for the time-advance pressure tensor. Since a predictor-corrector scheme is used the pressure tensor has to be computed at both integer and half time steps. However, it is still possible that the cyclotron terms introduce high-frequency electron effects which tend to isotropize the electron distribution function. These are eliminated using the implicit method. Additional isotropization effects based on processes on electron time scales need to be taken into account. For this reason an additional heuristic isotropization term is added here also.

Eq. (3.69) is rewritten in the following form:

$$\begin{aligned}\frac{\partial \bar{\bar{P}}_e}{\partial t} = &-\boldsymbol{v}_e \cdot \nabla \bar{\bar{P}}_e - \bar{\bar{P}}_e \nabla \cdot \boldsymbol{v}_e - \bar{\bar{P}}_e \cdot \nabla \boldsymbol{v}_e - \left(\bar{\bar{P}}_e \cdot \nabla \boldsymbol{v}_e\right)^T + \\ &-\frac{e}{m_e}\left[\bar{\bar{P}}_e \times \boldsymbol{B} + \left(\bar{\bar{P}}_e \times \boldsymbol{B}\right)^T\right] - \frac{\Omega_e}{\tau}\left(\bar{\bar{P}}_e - nkT\bar{\bar{1}}\right),\end{aligned} \quad (3.70)$$

where T denotes the initial electron temperature.

Different simulations were performed varying electron to ion mass ratio, to study ion tearing mode growth. Three different ratios are chosen for the simulations: $m_e/m_i = 1/18$, $m_e/m_i = 1/180$ and $m_e/m_i = 1/1800$. It was found that decreasing the electron to ion mass ratio reduces the mode growth. In the most realistic case (run 3) no growth of a tearing type instability is found. Raising τ to 1000 or 10000

decreases the importance of the isotropization. However, with both values, the simulations did not exhibit instability. Therefore it was concluded that, for small electron mass, the stabilization is controlled by the cyclotron term in the pressure evolution equation, rather than the heuristic isotropization model.

Kuznetsova et al. [1998] extended the previous model, including the electron mass also in the expression for the electric field. To incorporate the electron bulk flow velocity into the simulation code, the electron momentum equation (where resistivity has been omitted) reads:

$$\boldsymbol{E} = -\boldsymbol{v}_e \times \boldsymbol{B} - \frac{\nabla \cdot \bar{\bar{P}}_e}{en_e} - \frac{m_e}{e}\frac{d\boldsymbol{v}_e}{dt} \tag{3.71}$$

Taking the curl of Eq.(3.71):

$$\frac{\partial \hat{\boldsymbol{B}}}{\partial t} = -\left(\nabla \times \hat{\boldsymbol{E}}\right), \tag{3.72}$$

where

$$\hat{\boldsymbol{B}} = \boldsymbol{B} - d_e^2 \nabla^2 \boldsymbol{B}, \tag{3.73}$$

$$\hat{\boldsymbol{E}} = -\boldsymbol{v}_e \times \boldsymbol{B} - \frac{\nabla \cdot \bar{\bar{P}}_e}{en_e} - \frac{m_e}{e}\left(\boldsymbol{v}_e \cdot \nabla\right)\boldsymbol{v}_e, \tag{3.74}$$

and d_e is the electron skin depth. However, this set of equations is not exact: terms proportional to $m_e \partial n_e/\partial t$ and $m_e \partial \boldsymbol{v}_i/\partial t$ have been dropped because on short electron spatial scales ions are nearly immobile and the neglected density and ion velocity variations are small. In this way the equation for the electric field does not contain an explicit time derivative.

This method has also been reported by Lipatov [2001]. Here generalized fields $\hat{\boldsymbol{B}}$ and $\hat{\boldsymbol{E}}$ are advanced in time using the predictor-corrector scheme [Winske and Quest, 1986]. Two sets of simulations have been run to check if the predominant role in controlling the structure of the reconnection region around the X point was dominated by the electron bulk flow inertia or the kinetic quasi-viscous effect. The first set includes all the components of the pressure tensor, calculated without any approximation. However the heat flux is excluded from the equation. In this way the electron quasi-viscous effects associated with the evolution of the non-gyrotropic off-diagonal components of the full electron pressure tensor have been included. Conversely, in the second set of simulations the off-diagonal components of the pressure tensor have been set to zero.

Results of the simulations show that the predominant mechanism for the formation

of reconnection is the anisotropy of the pressure tensor. In the runs based only on electron bulk flow inertia the reconnection is small and strongly oscillating.

This problem has also been studied more recently in electron magnetohydrodynamics. Cai and Li [2009] found that, for EMHD, the conditions of either pressure-based dissipation or inertia-based dissipation are dominant depend on the relative magnitude between electron thermal Larmor radius and electron inertia skin depth.

The third approach we present has been developed by Swift [1996]. A fluid ion component that spatially overlaps with the discrete particle component is included in the model to approximate the cold ionospheric plasma. The electron momentum equation involves electron to ion mass ratio. This is initially set to zero. In the equation for ion particles motion friction with electron is included:

$$\frac{d\boldsymbol{v}}{dt} = \boldsymbol{E} + \boldsymbol{v} \times \boldsymbol{B} - \eta \left(\boldsymbol{u}_p - \boldsymbol{u}_e \right), \tag{3.75}$$

where $\boldsymbol{u}_p$ is the ion particle bulk flow velocity and $\boldsymbol{u}_e$ is the electron flow velocity. Here and in the rest of the description of the method $\boldsymbol{E}$ is in units of ion acceleration and $\boldsymbol{B}$ in units of ion gyrofrequency. The electron momentum equation is written in the form:

$$E = -\boldsymbol{u}_e \times \boldsymbol{B} - \eta \left(\boldsymbol{u}_e - \boldsymbol{u}_i \right), \tag{3.76}$$

where $\boldsymbol{u}_i$ is the total ion bulk flow speed, given by:

$$\boldsymbol{u}_i = \frac{n_p}{n}\boldsymbol{u}_p + \frac{n_f}{n}\boldsymbol{u}_f \tag{3.77}$$

Electron pressure term has been neglected. The electron flow speed is evaluated from Ampère's law:

$$\boldsymbol{u}_e = \boldsymbol{u}_i - \frac{\nabla \times \boldsymbol{B}}{\alpha n}, \tag{3.78}$$

where in the units of the simulation $\alpha = 4\pi e^2/m_i c^2$.

The equation for the fluid ion velocity is given by:

$$\frac{d\boldsymbol{u}_f}{dt} = \boldsymbol{E} + \boldsymbol{u}_f \times \boldsymbol{B} - \eta \left(\boldsymbol{u}_f - \boldsymbol{u}_e \right), \tag{3.79}$$

where the pressure term has been neglected again. The equation for ion particles motion can then be rewritten in the form:

$$\frac{d\boldsymbol{v}}{dt} = \boldsymbol{E}_p + \boldsymbol{v} \times \boldsymbol{B}, \tag{3.80}$$

where $\boldsymbol{E}_p$ is a convenient grouping of terms:

$$\boldsymbol{E}_p = \left(\frac{\nabla \times \boldsymbol{B}}{\alpha n} - \boldsymbol{u}_i \right) \times \boldsymbol{B} + \eta \frac{n_f}{n} \left(\boldsymbol{u}_f - \boldsymbol{u}_p \right). \tag{3.81}$$

The ion fluid momentum equation can also be rewritten in the form:

$$\frac{\partial \boldsymbol{u}_f}{\partial t} = -\boldsymbol{u}_f \cdot \nabla \boldsymbol{u}_f + \boldsymbol{E}_f + \frac{n_p}{n} \boldsymbol{u}_f \times \boldsymbol{B} - \eta \frac{n_p}{n} \boldsymbol{u}_f, \tag{3.82}$$

where $\boldsymbol{E}_f$ is again a convenient grouping of terms:

$$\boldsymbol{E}_f = \left(\frac{\nabla \times \boldsymbol{B}}{\alpha n} - \frac{n_p}{n} \boldsymbol{u}_p \right) \times \boldsymbol{B} + \eta \frac{n_p}{n} \boldsymbol{u}_p. \tag{3.83}$$

Substituting in Faraday's law electron momentum equation an expression for $\boldsymbol{B}$ time advancement is obtained:

$$\frac{\partial \boldsymbol{B}}{\partial t} = -\nabla \times \left[\left(\frac{\nabla \times \boldsymbol{B}}{\alpha n} - \boldsymbol{u}_i \right) \times \boldsymbol{B} \right] - \nabla \times \left(\eta \frac{\nabla \times \boldsymbol{B}}{\alpha n} \right). \tag{3.84}$$

The effect of electron inertia is to add electron polarization drift to the previous equation:

$$\begin{aligned} \frac{\partial}{\partial t} \left[\boldsymbol{B} + r \nabla \times \left(\frac{\nabla \times \boldsymbol{B}}{\alpha n} - \boldsymbol{u}_i \right) \right] = \\ r \nabla \times \left(\boldsymbol{u}_e \cdot \nabla \boldsymbol{u}_e \right) - \nabla \times \left[\left(\frac{\nabla \times \boldsymbol{B}}{\alpha n} - \boldsymbol{u}_i \right) \times \boldsymbol{B} \right] - \nabla \times \left(\eta \frac{\nabla \times \boldsymbol{B}}{\alpha n} \right), \end{aligned} \tag{3.85}$$

where r is the electron to ion mass ratio. Eq. (3.85) can be rewritten in a more computationally convenient way:

$$\frac{\partial}{\partial t} \boldsymbol{B}' = -r \nabla \times \left[\boldsymbol{u}_e \times \left(\nabla \times \boldsymbol{u}_e \right) \right] - \nabla \times \left[\left(\frac{\nabla \times \boldsymbol{B}}{\alpha n} - \boldsymbol{u}_i \right) \times \boldsymbol{B} \times \left(\eta \frac{\nabla \times \boldsymbol{B}}{\alpha n} \right) \right], \tag{3.86}$$

where

$$\boldsymbol{B} = \boldsymbol{B}' - r \nabla \times \left(\frac{\nabla \times \boldsymbol{B}}{\alpha n} - \boldsymbol{u}_i \right). \tag{3.87}$$

The equation is solved for $\boldsymbol{B}$ by iteration. For r small enough to maintain an electron inertial length much less than the distance between grid points only one iteration is needed. In many problems, like in the Earth's dipole field in the magnetospheric problem, the field is curl free. In order to avoid inaccuracy in the computation of the curl of the magnetic field, the latter is split into a time independent, curl-free portion $\boldsymbol{B}_0$ and a time dependent $\boldsymbol{B}_1$, where only the latter is

updated. The polarization drift correction is not included in equations for ions, since the correction is of the order of electron to ion mass ratio.

The next approach was first introduced by Jones and Parker [2003] for gyrokinetic problems and then used by Cheng et al. [2013] in hybrid simulation. The ions follow the equations of motion, where a resistive term $-\frac{q_i}{m_i}\eta \boldsymbol{J}$ is added in the equation for the velocity to provide momentum balance. From the electron momentum equation arises the generalized Ohm's law:

$$en_e(\boldsymbol{E} + \boldsymbol{v}_e \times \boldsymbol{B}) = en_e\eta\boldsymbol{J} - \nabla \cdot \bar{\bar{\Pi}}_e - m_e\frac{\partial n_e \boldsymbol{v}_e}{\partial t}, \tag{3.88}$$

where the electron stress tensor $\bar{\bar{\Pi}}_e$ is determined from the distribution function, i.e. depends on the model assumed for the electrons.

Using Ampère's law Eq.(3.89) can be written as:

$$en_e\boldsymbol{E} = -\boldsymbol{J}_i \times \boldsymbol{B} + \frac{1}{\mu_0}(\nabla \times \boldsymbol{B}) \times \boldsymbol{B} + \frac{en_e}{\mu_0}\eta(\nabla \times \boldsymbol{B}) - \nabla \cdot \bar{\bar{\Pi}}_e - m_e\frac{\partial n_e \boldsymbol{v}_e}{\partial t}. \tag{3.89}$$

To calculate the inertial term, the last on the RHS, Ampère's law is used, combined with the ion momentum equation. Taking the derivative of Ampère's law:

$$\mu_0\left(q_i\frac{\partial n_i \boldsymbol{v}_i}{\partial t} - e\frac{\partial n_e \boldsymbol{v}_e}{\partial t}\right) = \nabla \times \frac{\partial \boldsymbol{B}}{\partial t} = -\nabla \times \nabla \times \boldsymbol{E}. \tag{3.90}$$

The first term on the LHS is obtained from the ion momentum equation:

$$m_i\frac{\partial n_i \boldsymbol{v}_i}{\partial t} = q_i n_i(\boldsymbol{E} + \boldsymbol{v}_i \times \boldsymbol{B}) - \nabla \cdot \bar{\bar{\Pi}}_i - q_i n_i\frac{\eta}{\mu_0}\nabla \times \boldsymbol{B} \tag{3.91}$$

The electron inertia then takes the form:

$$m_e\frac{\partial n_e \boldsymbol{v}_e}{\partial t} = \frac{m_e q_i}{m_i e}\left(q_i n_i(\boldsymbol{E} + \boldsymbol{v}_i \times \boldsymbol{B}) - \nabla \cdot \bar{\bar{\Pi}}_i - q_i n_i\frac{\eta}{\mu_0}\nabla \times \boldsymbol{B}\right) + \frac{m_e}{\mu_0 e}\nabla \times (\nabla \times \boldsymbol{E}). \tag{3.92}$$

Using quasi neutrality the generalized Ohm's law becomes:

$$en_i\left(1 + \frac{m_e q_i^2}{m_i e^2}\right)\boldsymbol{E} + \frac{m_e}{\mu_0 e}\nabla \times (\nabla \times \boldsymbol{E}) = -\left(1 + \frac{m_e q_i}{m_i e}\right)\boldsymbol{J}_i \times \boldsymbol{B} + \frac{1}{\mu_0}\nabla \times (\nabla \times \boldsymbol{B}) + \\ + \eta\frac{en_i}{\mu_0}\left(1 + \frac{m_e q_i^2}{m_i e^2}\right)\nabla \times \boldsymbol{B} - \nabla \cdot \bar{\bar{\Pi}}_e + \frac{m_e q_i}{m_i e}\nabla \times \bar{\bar{\Pi}}_i, \tag{3.93}$$

which can be solved for $\boldsymbol{E}$ without time advancement.

Valentini et al. [2007] introduced a finite value for the electron mass in a Vlasov-Hybrid code. In the latter they solve a set of normalized equations composed by:

- The Vlasov equation for the ion's distribution function:

$$\frac{\partial f_i}{\partial t} + \boldsymbol{v}_i \cdot \nabla f_i + (\boldsymbol{E} + \boldsymbol{v}_i \times \boldsymbol{B}) \cdot \frac{\partial f_i}{\partial \boldsymbol{v}_i} = 0; \tag{3.94}$$

- A generalized Ohm's law for electric field:

$$\begin{aligned} \boldsymbol{E} - d_e^2 \Delta \boldsymbol{E} = -(\boldsymbol{v}_i \times \boldsymbol{B}) + \frac{1}{n}(\boldsymbol{J} \times \boldsymbol{B}) + \frac{1}{n} d_e^2 \nabla \cdot \bar{\bar{\Pi}}_i + \\ - \frac{1}{n}\nabla p_e + \frac{d_e^2}{n} \nabla \cdot [\boldsymbol{v}_i \boldsymbol{J} + \boldsymbol{J} \boldsymbol{v}_i] - \frac{1}{n} d_e^2 \nabla \cdot (\frac{\boldsymbol{J}\boldsymbol{J}}{n}), \end{aligned} \tag{3.95}$$

  where d_e is the electron skin depth and p_e is the scalar electron pressure considered isotropic;

- Maxwell's equations for the magnetic field are:

$$\frac{\partial \boldsymbol{B}}{\partial t} = -\nabla \times \boldsymbol{E} \tag{3.96}$$

$$\nabla \times \boldsymbol{B} = \mu_0 \boldsymbol{J} \tag{3.97}$$

where quasi-neutrality and Darwin approximation hold.

While the time advancement is discussed in details in the next chapter, we will focus here on how the generalized Ohm's law is found. A third approximation is assumed: the plasma is weakly magnetized, i.e. $\Omega_{ce} << \omega_{pe}$, where $\omega_{pe} = (\frac{ne^2}{m_e \epsilon_0})^{1/2}$ is the electron plasma frequency and $\Omega_{ce} = eB/m_e$ is the electron cyclotron frequency. Starting from electron and ion momentum equations:

$$\frac{\partial (n\boldsymbol{v}_e)}{\partial t} + \nabla \cdot (n \boldsymbol{v}_e \boldsymbol{v}_e) = -\frac{1}{m_e}\nabla p_e - \frac{ne}{m_e}(\boldsymbol{E} + \boldsymbol{v}_e \times \boldsymbol{B}), \tag{3.98}$$

$$\frac{\partial (n\boldsymbol{v}_i)}{\partial t} + \nabla \cdot (n \boldsymbol{v}_i \boldsymbol{v}_i) = -\frac{1}{m_i}\nabla \bar{\bar{\Pi}}_i - \frac{ne}{m_i}(\boldsymbol{E} + \boldsymbol{v}_i \times \boldsymbol{B}), \tag{3.99}$$

Faraday's and Ampère's laws are substituted in the LHS of the first:

$$\frac{\partial (n\boldsymbol{v}_e)}{\partial t} = \frac{\partial (n\boldsymbol{v}_i)}{\partial t} - \frac{\partial}{\partial t}\left(\frac{\boldsymbol{J}}{e}\right) = \frac{\partial (n\boldsymbol{v}_i)}{\partial t} + \frac{1}{\mu_0}\nabla \times (\nabla \times \boldsymbol{E}) \tag{3.100}$$

$$\nabla \cdot (n\boldsymbol{v}_e\boldsymbol{v}_e) = \nabla \cdot \left[n \left(\boldsymbol{v}_i - \frac{\boldsymbol{J}}{ne} \right) \left(\boldsymbol{v}_i - \frac{\boldsymbol{J}}{ne} \right) \right] = \nabla \cdot (n\boldsymbol{v}_i\boldsymbol{v}_i) - \frac{1}{e}\nabla \cdot (\boldsymbol{v}_i\boldsymbol{J}) - \frac{1}{e}\nabla \cdot (\boldsymbol{J}\boldsymbol{v}_i) + \nabla \cdot \left(\frac{\boldsymbol{J}\boldsymbol{J}}{ne^2} \right) \quad (3.101)$$

Subtracting the electron momentum equation from the ion one and defining μ as the inverse of the reduced mass $\mu = 1/m_e + 1/m_i$:

$$\mu ne\boldsymbol{E} + \frac{1}{\mu_0\sqrt{4\pi\epsilon_0}}\nabla \times (\nabla \times \boldsymbol{E}) = \frac{1}{m_i}\nabla \cdot \bar{\bar{\Pi}}_i - \frac{1}{m_e}\nabla P_e + \frac{1}{m_e}(\boldsymbol{J} \times \boldsymbol{B}) - \mu ne\,(\boldsymbol{v}_i \times \boldsymbol{B}) + \frac{1}{e}\nabla \cdot (\boldsymbol{v}_i\boldsymbol{J}) + \frac{1}{e}\nabla \cdot (\boldsymbol{J}\boldsymbol{v}_i) - \nabla \cdot \left(\frac{\boldsymbol{J}\boldsymbol{J}}{ne^2} \right), \quad (3.102)$$

which does not contain time derivatives as a consequence of quasi-neutrality approximation. Approximating $\mu \approx 1/m_e$:

$$\boldsymbol{E} + \frac{1}{\mu_0\sqrt{4\pi\epsilon_0}}\nabla \times (\nabla \times \boldsymbol{E}) = (\boldsymbol{v}_i \times \boldsymbol{B}) + \frac{1}{ne}(\boldsymbol{J} \times \boldsymbol{B}) + \frac{m_e}{nem_i}\nabla \times \bar{\bar{\Pi}}_i - \frac{1}{ne}\nabla p_e + \frac{m_e}{ne^2}\nabla \cdot [\boldsymbol{v}_i\boldsymbol{J} + \boldsymbol{J}\boldsymbol{v}_i] - \frac{m_e}{ne^3}\nabla \cdot \left(\frac{\boldsymbol{J}\boldsymbol{J}}{n} \right), \quad (3.103)$$

which after normalization this yields the generalized Ohm's equation used by Valentini.

Muñoz et al. [2017] implemented a PIC hybrid code, `CHIEF`, with inertial electron fluid equation without approximation. Here they solve the relativistic Newton's equations of motion for macro particles calculating $\boldsymbol{E}$ and $\boldsymbol{B}$ for this advancement by integrating the full electromagnetic fields over the shape function used to define the distribution function. To compute the electric field they consider the electron momentum equation with finite electron inertia and resistive effects:

$$\boldsymbol{E} = -\boldsymbol{v}_e \times \boldsymbol{B} - \frac{1}{en_e}\frac{\partial P_{e,jk}}{\partial x_k} - \frac{m_e}{e}\left(\frac{\partial \boldsymbol{v}_e}{\partial t} + (\boldsymbol{v}_e \cdot \nabla)\,\boldsymbol{v}_e \right) + \eta\boldsymbol{J}, \quad (3.104)$$

which is a generalized Ohm's law. In the latter $\eta = m_e\nu/(e^2n_e)$ is the collisional resistivity with ν collision frequency between electrons and ions and $P_{e,jk}$ is the jk component of the electron pressure tensor. Again quasi-neutrality and the Darwin

approximation hold so that Maxwell's equations read:

$$\nabla \times \boldsymbol{E} = -\frac{\partial \boldsymbol{B}}{\partial t} \tag{3.105}$$

$$\nabla \times \boldsymbol{B} = \mu_0 ne(\boldsymbol{v}_i - \boldsymbol{v}_e) \tag{3.106}$$

Combining Faraday's law and the electrons momentum equation, an equation with the form of a generalized continuity equation is obtained:

$$\frac{\partial \boldsymbol{W}}{\partial t} = \nabla \times [\boldsymbol{v}_e \times \boldsymbol{W}] - \nabla \times \left(\frac{\nabla p_e}{m_e n_e}\right) - \nabla \times \left(\frac{\nu}{e n_e}\boldsymbol{J}\right), \tag{3.107}$$

where $\boldsymbol{W} = \nabla \times \boldsymbol{v}_e - e\boldsymbol{B}/m_e$ is a generalized vorticity. A scalar electron pressure has been assumed for simplicity. After the vorticity equation has been advanced, the magnetic field is computed solving an elliptic equation given by Ampère's law and the definition of generalized vorticity:

$$\frac{1}{\mu_0 e}\nabla \times \left(\frac{\nabla \times \boldsymbol{B}}{n_e}\right) + \frac{e\boldsymbol{B}}{m_e} = \nabla \times \boldsymbol{v}_i - \boldsymbol{W}. \tag{3.108}$$

The electric field is then obtained from the generalized Ohm's law by explicit evaluation of the derivative term $\frac{\partial \boldsymbol{v}_e}{\partial t}$.

We will now proceed reporting some examples in which some of the previous methods have been used.

Yin et al. [2001] and Yin and Winske [2002] studied collisionless reconnection in a thin current sheet. To understand substorm dynamics it is important to study the mechanisms involved in the current sheet thinning process. This process has been studied using two-dimensional hybrid and Hall-MHD simulations, including the full electron pressure tensor in the generalized Ohm's law to initiate reconnection.

Overall agreement is found between the two calculations for the reconnection rate, the global configuration of the currents and the fields, and the properties of the electron pressure. It is shown that while the electron pressure tensor effect are important at the X point, in the surrounding regions the magnetic field strength becomes finite, and the Hall term provides the dominant contribution to E_z.

Swift and Lin Swift and Lin [2001] used a two-dimensional hybrid code to simulate a variety of processes related to the onset of the substorm expansion phase that take place in the midnight meridian plane of the magnetosphere. In the code they included electron inertia effects using Swift's approach. However, they concluded that some other mechanism involving electron inertia should be added to investigate

further in detail the appearance of the filamentary field-aligned currents connecting the region just behind the dipolarization front with the high-latitude ionosphere.

Since the approaches described in this section have been used only very few times, as a result of the analysis of the different algorithms to take into account electron inertia we decided to keep the approximation of a mass-less electron fluid in the implementation of our codes. We note that methods incorporating electron inertia which rely on a form of the generalized Ohm's law (e.g., Valentini et al. [2007]) are relatively easy to add to a hybrid code which, as a first step, assumes massless electrons.

3.4 Existing methods: implementation and comparisons

The algorithms described in the first section of this chapter have been implemented in C++ programming language. Making use of an already existing Predictor-Corrector code (Hips) as starting point, we implemented the algorithms described in the previous section. The new code implemented uses the same structures of Hips code for initializations and data storage. Also the hierarchy is maintained, while the functions and their calls in the main function are changed to perform each time a different algorithm. The code is implemented in a way that it is possible to select the algorithm to use from an input file, in *kvf* format (a file format for simulation initialization). We do not report here details regarding the single implementations.

In the following we use the following abbreviations:

- *PC* for Predictor Corrector;
- *CAM-CL* for the Current Advance Method with Cyclic Leapfrog described in the previous section;
- *CAM-CL 2* for a variant of the latter, where the particles at full time steps are collected after a half a time step advancement, instead of being averaged. This implies one extra particle push;
- *TVD* for the Total Variation Diminishing scheme for the magnetic induction equation, while the rest of the scheme uses the normal CAM-CL;
- *VELOCITY EXTRAPOLATION* for the Richardson's velocity extrapolation method.

A suite of tests to compare the codes has been developed. This includes:

- energy conservation on long simulations, with quiet Maxwellian initial conditions. Here the CAM-CL method is the one which performed better;
- a set of instabilities, with comparisons on the wavelengths generated with the different algorithms;
- initial conditions with discontinuities in the magnetic field. In the case of no additional flow the behaviour is the same in all the methods, with the diffusion of the discontinuity. In the presence of flow the TVD method behaves better than the others, with less spreading of the gradient due to the discontinuity;
- propagation of an Alfvén wave. Given an Alfvén wave as initial condition, we follow its propagation, checking that its ω and k are in agreement with the initial conditions. In all the methods the error are of the order of 1%;
- comparisons between the different time of executions. The following table shows the time of execution for the different algorithms for 1000 time steps.

Average time of executionf for 1000 time steps (s)				
PC	CAM-CL	CAM-CL 2	TVD	VELOCITY EXTRAPOLATION
40.56	21.50	25.66	22.76	23.04

Table 3.1: Execution time for different algorithms in seconds. The Predictor Corrector is the slower as it performs two times the advancement of particle positions and velocities every time step.

  In all the methods substepping in the magnetic field advancement has been included, with 16 substeps for each time step. We can see that the CAM-CL is the faster and it is almost twice as fast than the Predictor-Corrector scheme.

- stability test. The criterion used for stability is to find the biggest time step for which the simulation does not diverge for 100 ion cyclotron periods, for a quiet Maxwellian initial condition. It is an arbitrary criterion used only for comparison between the methods.

All the tests have been done both in the case of absence and presence of flow.

In the following we report as an example a comparison between the algorithms for a beam instability simulation.

Bigger time step without diverging for 100 Ω_i^{-1} (in Ω_i^{-1})				
PC	CAM-CL	CAM-CL 2	TVD	VELOCITY EXTRAPOLATION
0.251675	0.253527	0.237400	0.415355	0.133357

Table 3.2: Stability test for different algorithms. For each method is given the biggest time step in ion cyclotron periods for which the simulation does not diverge.

3.5 A beam instability simulation

We report here results from a beam instability simulation. For more details about ion beam instabilities refer to Chapter 6. The initial conditions are set up using two different ion populations: a main population and a beam which constitutes the 1% of the total ions. The two populations have different shift velocities, with a difference of 10 times the Alfvén velocity. However, the total ion shift velocity considered the two populations together is zero and there is no net flow.

We performed a simulation on 800 cells of size $\Delta x = 0.5$ ion inertial length, running it for 5000 time steps, with $\Delta t = 0.02$ ion cyclotron periods, with four different algorithms, and compared the results.

Here and throughout the rest of our work we used second order shape functions for PIC interpolations.

Figure 3.1 shows the evolution of the y component of the magnetic field. In the horizontal axe we have the x position, while in the vertical axe the time t. Different colours represent different values of magnetic field as specified by the colourbar. On the top left panel we show B_y obtained using the Predictor Corrector scheme, on the top right panel that obtained using the CAM-CL scheme, on the bottom left using the TVD shceme and on the bottom right using the Velocity Extrapolation. In the linear phase we obtain perturbations with roughly the same amplitude and wave length for all the simulations.

It is interesting to see how the results are almost identical in all the simulations, excluding the TVD scheme, which is the only one which adds some artificial element during the field computations. However, also in this case the wavelengths developed are the same as in the other methods and this can be visualized in the Fourier transformed graphs of both B_y and B_z. We report here results for B_y, number density, and total energy.

In Fig. 3.2 we show the evolution of the number density in the same order as before. Again we can see that the TVD scheme anticipates the propagation of perturbations adding some artificial effects. However this method preserves energy better, having

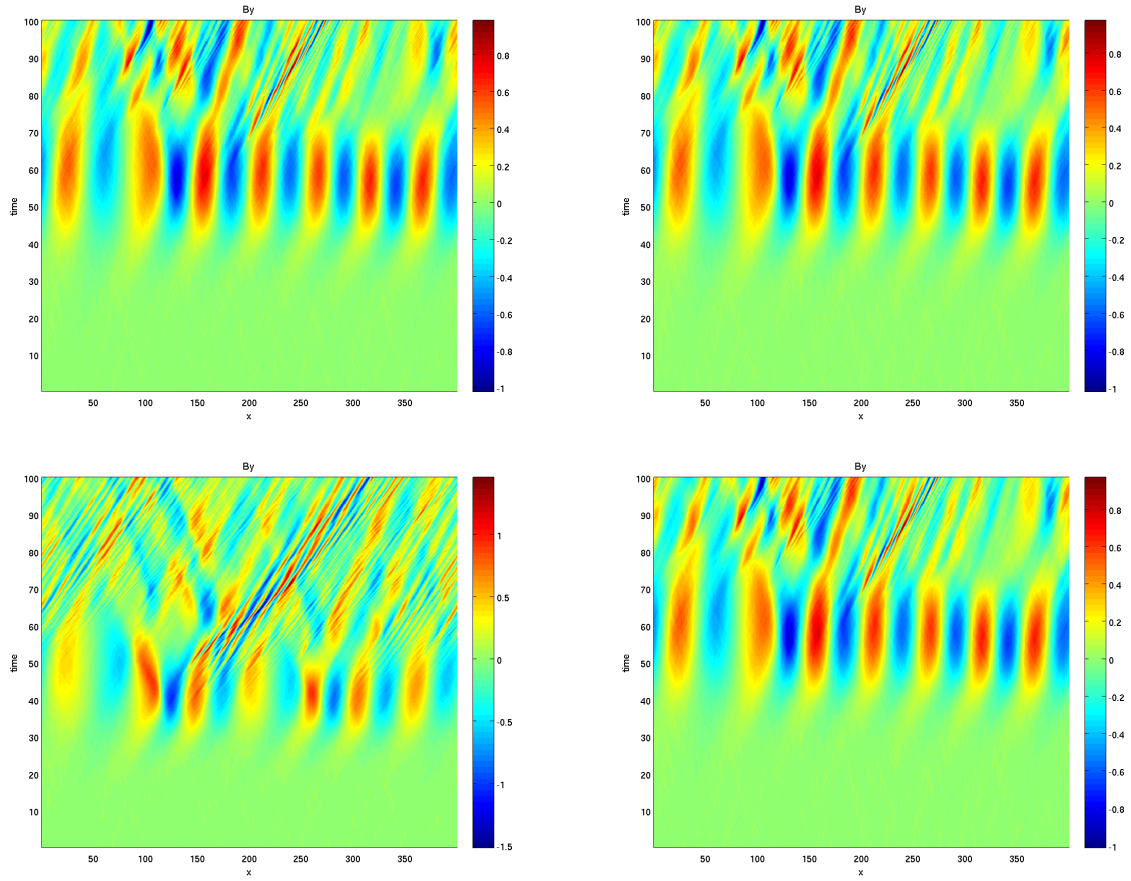

Figure 3.1: B_y evolution with Predictor-Corrector(top left), CAM-CL (top right), TVD (bottom left) and Velocity Extrapolation(bottom right) algorithms. In all the simulations an instability develops and in the linear phase we can observe waves propagating with 7 wavelengths in the simulation box.

an overall smaller reduction in the total energy in the system as shown in Fig. 3.3.

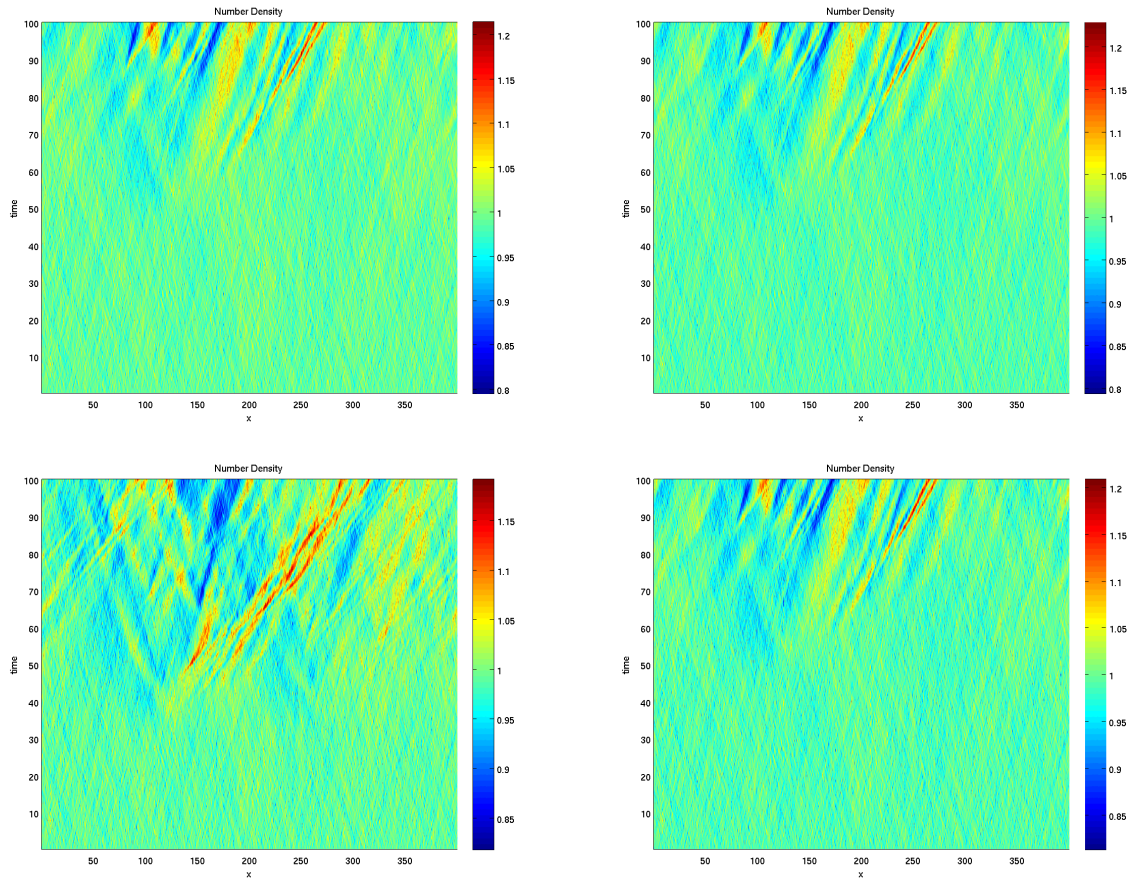

Figure 3.2: Number density evolution with Predictor-Corrector(top left), CAM-CL (top right), TVD (bottom left) and Velocity Extrapolation(bottom right) algorithms. The perturbation in the number density starts earlier in the TVD scheme due to the effect of artificial flux limiting at cells boundaries.

From the set of simulations we can conclude that TVD schemes performs better in some cases as predicted. In fact, when the gradients are steep or fluxes are strong the imposition of the diminishing of the total variation through limiters helps the simulation to stay more stable. However, the effect of limiters can be not desired when simulating instabilities, because these can add some artificial diffusion or excite the instability in a wrong way. In these cases all the other methods gave satisfactory results, but the CAM-CL is preferred for the execution time, stability, and energy conservation.

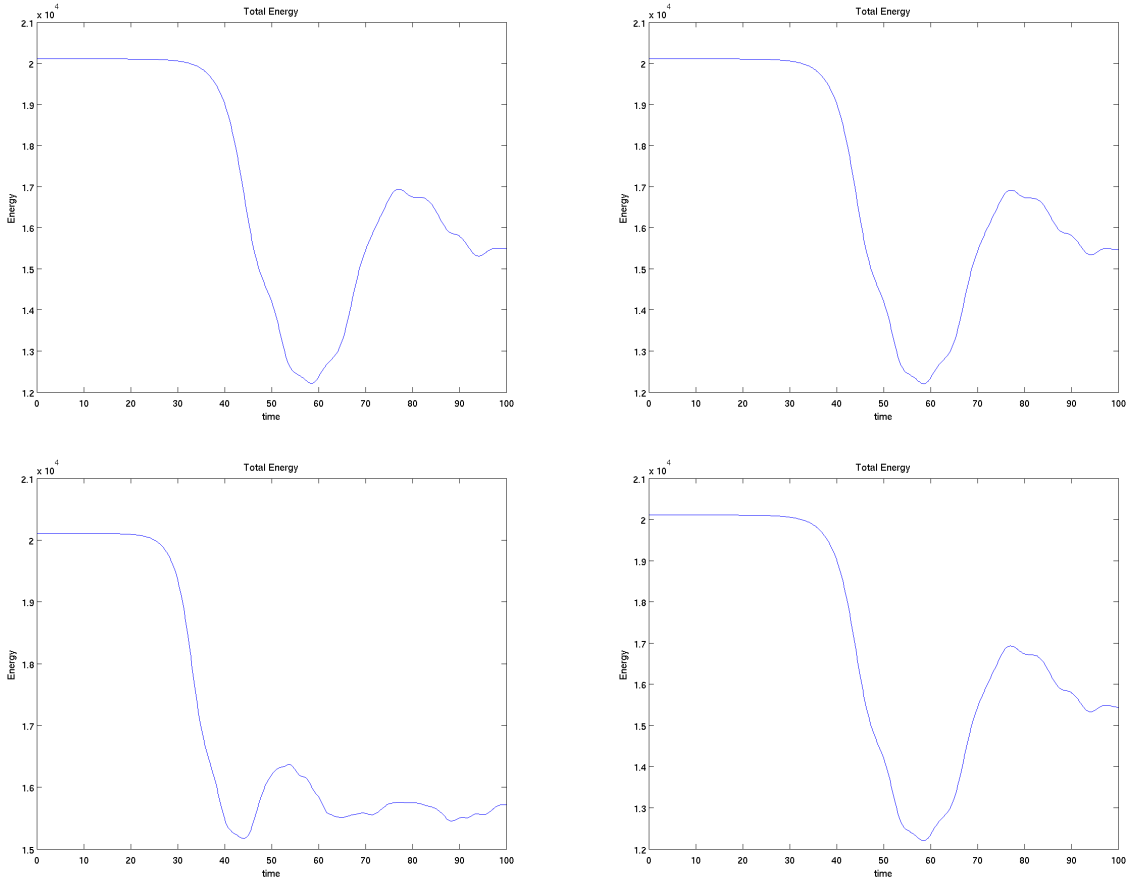

Figure 3.3: Total energy evolution with Predictor-Corrector(top left), CAM-CL (top right), TVD (bottom left) and Velocity Extrapolation(bottom right) algorithms. We can appreciate that the energy is well conserved for the first linear phaase of the instability growth. When nonlinear phenomena develop we have a big oscillation in the total energy which then keeps a different $\sim$constant value. The maximum variation of energy ranges between 25% for TVD method and 40% for the others, while the variation between constant values ranges between 22% for TVD and 23% for the others.

4 A Vlasov-Hybrid code with Hermite expansion of the distribution function

The work in this and the following chapters contains material submitted to the Journal of Computational Physics. It has been carried out in collaboration with Enrico Camporeale (Centrum Wiskunde Informatica, Amsterdam) and David Burgess (Queen Mary University of London). Enrico Camporeale provided governing equations for the solution of the Vlasov equation using expansion in Hermite weighted polynomials, and Francesco Boffa developed the Hermite-Vlasov-Hybrid numerical algorithm, and performed code development and testing.

In the following we present an Hermite-Vlasov-hybrid algorithm and code implemetation which uses the Hermite expansion of the distribution function presented in Camporeale et al. [2013a,b]. The expansion in the Hermite basis is motivated by several reasons. The basis is a completely orthogonal basis with respect to a Gaussian weight function. This makes it optimal to expand distribution functions with a Maxwellian form. In fact, an expansion which makes use of one single term in each velocity direction is capable of representing exactly a non-drifting Maxwellian distribution function. Also, due to the properties of the basis, there is a linear relation between the first order coefficients of the expansion and the moments of the distribution function. It is therefore possible to compute the moments easily, without the need of numerical integrations.

The use of a spectral representation of the distribution function allows us to reduce the number of "discretization" points in velocity space. In Chapter 2 we saw that modern Vlasov-hybrid simulations employ $\approx 50 - 60$ discretization point in each velocity direction and they still need improvements. In the following we will show how the Hermite expansion allowed us to strongly reduce this number.

4.1 Algorithm

The Hermite-Vlasov-hybrid (HVH) method we present here combines the solution of the Vlasov equation through expansion of the distribution function as a sum of Hermite functions, together with the Current Advance Method presented in Valentini et al. [2007]. The Vlasov equation resolves the protons which hence are treated kinetically, while electrons are treated as a massless fluid described only by their momentum equation. The plasma components are coupled via Maxwell's equations in which quasi-neutrality and Darwin approximations hold.

We solve a set of four equations:

- Vlasov equation for the distribution function:

$$\frac{\partial f_s}{\partial t} + \boldsymbol{v}_s \cdot \nabla f_s + \frac{q_s}{m_s}(\boldsymbol{E} + \boldsymbol{v}_s \times \boldsymbol{B}) \cdot \frac{\partial f_s}{\partial \boldsymbol{v}} = 0 \tag{4.1}$$

- momentum equation for electrons [Matthews, 1994]:

$$\boldsymbol{E} = -\boldsymbol{v}_i \times \boldsymbol{B} + \frac{1}{\mu_0\, e n_e}\boldsymbol{j} \times \boldsymbol{B} - \frac{\nabla p_e}{e n_e} + \eta \boldsymbol{j} \tag{4.2}$$

- Maxwell equations for the magnetic field, with the chosen assumptions:

$$\frac{\partial \boldsymbol{B}}{\partial t} = -\nabla \times \boldsymbol{E}, \tag{4.3}$$

$$\nabla \times \boldsymbol{B} = \mu_0 \boldsymbol{j} \tag{4.4}$$

Here f_s is the distribution function for ion species s; $\boldsymbol{v}_s$ is the bulk velocity of species s (particle charge q_s and mass m_s); $\boldsymbol{v}_i$ is the bulk ion velocity; $\boldsymbol{E}$ is the electric field; $\boldsymbol{B}$ is the magnetic field; n_i (n_e) is the ion (electron) density, and quasi-neutrality is assumed so $n = n_i = n_e$; p_e is the scalar electron pressure; η is the resistivity; $\boldsymbol{j}$ is the total current, where $\boldsymbol{j} = \boldsymbol{j}_i + \boldsymbol{j}_e = \sum_s \boldsymbol{j}_s + \boldsymbol{j}_e$.

4.1.1 Hermite decomposition

Quantities are normalized as follows: time is normalized to the inverse of the ion gyrofrequency Ω_i^{-1}, lengths to the ion inertial length $d_i = c/\omega_{pi}$, velocities to the Alfvén speed, electric and magnetic fields to a reference field B_0. The cyclotron frequency for species s is defined (with sign) as $\Omega_s = q_s B_0/(m_s)$ The Vlasov equation

for the species s then reads:

$$\frac{\partial f_s}{\partial t} + \boldsymbol{v}_s \cdot \frac{\partial f_s}{\partial \boldsymbol{x}} + \frac{\Omega_s}{\omega}(\boldsymbol{E} + \boldsymbol{v}_s \times \boldsymbol{B}) \cdot \frac{\partial f_s}{\partial \boldsymbol{v}} = 0. \tag{4.5}$$

The Hermite decomposition for the velocity dependent part of the distribution function employs the asymmetrically-weighted Hermite basis:

$$\Psi_n(\xi) = (\pi 2^n n!)^{-1/2} H_n(\xi) e^{-\xi^2}, \tag{4.6}$$

$$\Psi^n(\xi) = (2^n n!)^{-1/2} H_n(\xi), \tag{4.7}$$

where H_n is the n-th Hermite polynomial. The distribution function $f_s(\mathbf{x}, \mathbf{v}, t)$ is given by:

$$f_s(\mathbf{x}, \mathbf{v}, t) = \sum_{p,q,r} C^s_{p,q,r}(\mathbf{x}, t) \Psi_p(\xi_x) \Psi_q(\xi_y) \Psi_r(\xi_z), \tag{4.8}$$

with

$$\xi_x = (v_x - u_s)/\alpha_s \tag{4.9}$$

$$\xi_y = (v_y - v_s)/\beta_s \tag{4.10}$$

$$\xi_z = (v_z - w_s)/\gamma_s. \tag{4.11}$$

At this point u_s, v_s, w_s and $\alpha_s, \beta_s, \gamma_s$ represent six constant parameters for each kinetic species. They may be chosen depending on the initial conditions, and in principle they allow adaptivity and optimization of the basis [Delzanno, 2015]. For instance, for an initially non-drifting Maxwellian distribution, we might fix $u_s = v_s = w_s = 0$, and $\alpha_s, \beta_s, \gamma_s$ equal to, or reasonably close to the thermal velocity in the respective direction. The choice of these parameters is discussed in more length later. Note that in Eq. (4.8) one can choose independently the number of modes in each direction (i.e., the upper bounds for p, q, r in the summation).

The Hermite basis has the following properties ($\delta_{n,m}$ is the Kronecker delta):

$$\int_{-\infty}^{\infty} \Psi_n(\xi) \Psi^m(\xi) d\xi = \delta_{n,m}, \tag{4.12}$$

$$v_x \Psi_n(\xi_x) = \alpha \sqrt{\frac{n+1}{2}} \Psi_{n+1} + \alpha \sqrt{\frac{n}{2}} \Psi_{n-1} + u \Psi_n, \tag{4.13}$$

$$\frac{d\Psi_n(\xi_x)}{dv_x} = -\frac{1}{\alpha} \sqrt{2(n+1)} \Psi_{n+1}(\xi_x). \tag{4.14}$$

and similarly for the other directions.

The derivation of the Vlasov equation in Hermite space proceeds as follows: upon subsitution of Eq. (4.8) into (4.5) one multiplies Eq. (4.5) by $\Psi^l(\xi_x)\Psi^m(\xi_y)\Psi^n(\xi_y)$, and integrates over $d\xi_x d\xi_y d\xi_z$, by using the given properties. For simplicity we drop the s related to the different species and some variable dependency.

We proceed term by term in the Vlasov equation to find the corresponding expression for the coefficients in the Hermite expansion.

First term $\left(\frac{\partial f}{\partial t}\right)$

$$\iiint \sum_{p,q,r} \frac{\partial C_{p,q,r}}{\partial t} \Psi_p(\xi_x)\Psi_q(\xi_y)\Psi_r(\xi_z)\Psi^l(\xi_x)\Psi^m(\xi_y)\Psi^n(\xi_y) d\xi_x d\xi_y d\xi_z = \frac{\partial C_{l,m,n}}{\partial t}. \quad (4.15)$$

Second term:

Taking the x component only gives:

$$v_x \frac{\partial f}{\partial x} = v_x \sum_{p,q,r} \frac{\partial C_{p,q,r}}{\partial x} \Psi_p(\xi_x)\Psi_q(\xi_y)\Psi_r(\xi_z) = \sum_{p,q,r} \frac{\partial C_{p,q,r}}{\partial x} \left(\alpha\sqrt{\frac{p+1}{2}}\Psi_{p+1} + \alpha\sqrt{\frac{p}{2}}\Psi_{p-1} + u\Psi_p \right) \Psi_q\Psi_r, \quad (4.16)$$

so that

$$\iiint v_x \frac{\partial f}{\partial x} \Psi^l(\xi_x)\Psi^m(\xi_y)\Psi^n(\xi_y) d\xi_x d\xi_y d\xi_z = \alpha \left(\sqrt{\frac{l+1}{2}} \frac{\partial C_{l+1,m,n}}{\partial x} + \sqrt{\frac{l}{2}} \frac{\partial C_{l-1,m,n}}{\partial x} + \frac{u}{\alpha} \frac{\partial C_{l,m,n}}{\partial x} \right), \quad (4.17)$$

and similarly for the other components by permuting subscripts.

Third term (E field):

Taking the x component:

$$E_x \frac{\partial f}{\partial v_x} = E_x \sum_{p,q,r} C_{p,q,r} \left(-\frac{1}{\alpha}\sqrt{2(p+1)}\Psi_{p+1}(\xi_x) \right) \Psi_q(\xi_y)\Psi_r(\xi_z), \quad (4.18)$$

so that after integration

$$\iiint E_x \frac{\partial f}{\partial v_x} \Psi^l(\xi_x)\Psi^m(\xi_y)\Psi^n(\xi_y) d\xi_x d\xi_y d\xi_z \qquad = \qquad -\frac{\sqrt{2l}}{\alpha} E_x C_{l-1,m,n}, \quad (4.19)$$

and again similarly for other components.

Third term (v cross B)

For the x component:

$$\begin{aligned}(v_y B_z - v_z B_y)\frac{\partial f}{\partial v_x} = \sum_{p,q,r} C_{p,q,r} \left(-\frac{1}{\alpha}\sqrt{2(p+1)}\Psi_{p+1} \right) * \\ \left[B_z \left(\beta\sqrt{\frac{q+1}{2}}\Psi_{q+1} + \beta\sqrt{\frac{q}{2}}\Psi_{q-1} + v\Psi_q \right) \Psi_r \right] + \\ - \left[B_y \Psi_q \left(\gamma\sqrt{\frac{r+1}{2}}\Psi_{r+1} + \gamma\sqrt{\frac{r}{2}}\Psi_{r-1} + w\Psi_r \right) \right]. \quad (4.20)\end{aligned}$$

Upon integration there are three terms in B_y and three in B_z:

$$\begin{aligned}B_z \left[C_{l-1,m-1,n} \left(\frac{-\beta}{\alpha}\sqrt{lm} \right) + C_{l-1,m+1,n} \left(\frac{-\beta}{\alpha}\sqrt{l(m+1)} \right) + C_{l-1,m,n} \left(\frac{-v}{\alpha}\sqrt{2l} \right) \right] \\ -B_y \left[C_{l-1,m,n-1} \left(\frac{-\gamma}{\alpha}\sqrt{ln} \right) + C_{l-1,m,n+1} \left(\frac{-\gamma}{\alpha}\sqrt{l(n+1)} \right) + C_{l-1,m,n} \left(\frac{-w}{\alpha}\sqrt{2l} \right) \right] \quad (4.21)\end{aligned}$$

For the y component, by permuting subscripts:

$$\begin{aligned}(v_z B_x - v_x B_z)\frac{\partial f}{\partial v_y} = \sum_{p,q,r} C_{p,q,r} \left(-\frac{1}{\beta}\sqrt{2(q+1)}\Psi_{q+1} \right) * \\ \left[B_x \Psi_p \left(\gamma\sqrt{\frac{r+1}{2}}\Psi_{r+1} + \gamma\sqrt{\frac{r}{2}}\Psi_{r-1} + w\Psi_r \right) \right] - \\ \left[B_z \left(\alpha\sqrt{\frac{p+1}{2}}\Psi_{p+1} + \alpha\sqrt{\frac{p}{2}}\Psi_{p-1} + u\Psi_p \right) \Psi_r \right] \quad (4.22)\end{aligned}$$

And after integration:

$$B_x\left[C_{l,m-1,n-1}\left(\frac{-\gamma}{\beta}\sqrt{mn}\right)+C_{l,m-1,n+1}\left(\frac{-\gamma}{\beta}\sqrt{m(n+1)}\right)+C_{l,m-1,n}\left(\frac{-w}{\beta}\sqrt{2m}\right)\right]$$
$$-B_z\left[C_{l-1,m-1,n}\left(\frac{-\alpha}{\beta}\sqrt{lm}\right)+C_{l+1,m-1,n}\left(\frac{-\alpha}{\beta}\sqrt{(l+1)m}\right)+C_{l,m-1,n}\left(\frac{-u}{\beta}\sqrt{2m}\right)\right] \tag{4.23}$$

For the z component (permuting subscripts) we have:

$$(v_xB_y-v_yB_x)\frac{\partial f}{\partial v_z}=\sum_{p,q,r}C_{p,q,r}\left(-\frac{1}{\gamma}\sqrt{2(r+1)}\Psi_{r+1}\right)*$$
$$\left[B_y\Psi_q\left(\alpha\sqrt{\frac{p+1}{2}}\Psi_{p+1}+\alpha\sqrt{\frac{p}{2}}\Psi_{p-1}+u\Psi_p\right)\right]-$$
$$\left[B_x\left(\beta\sqrt{\frac{q+1}{2}}\Psi_{q+1}+\beta\sqrt{\frac{q}{2}}\Psi_{q-1}+v\Psi_q\right)\Psi_p\right] \tag{4.24}$$

And after integration:

$$B_y\left[C_{l-1,m,n-1}\left(\frac{-\alpha}{\gamma}\sqrt{nl}\right)+C_{l+1,m,n-1}\left(\frac{-\alpha}{\gamma}\sqrt{(l+1)n}\right)+C_{l,m,n-1}\left(\frac{-u}{\gamma}\sqrt{2n}\right)\right]$$
$$-B_x\left[C_{l,m-1,n-1}\left(\frac{-\beta}{\gamma}\sqrt{mn}\right)+C_{l,m+1,n-1}\left(\frac{-\beta}{\gamma}\sqrt{n(m+1)}\right)+C_{l,m,n-1}\left(\frac{-v}{\gamma}\sqrt{2n}\right)\right] \tag{4.25}$$

Combining all terms, we obtain the evolution equation for the coefficients of the Hermite expansion:

$$
\begin{aligned}
&\frac{\partial C_{l,m,n}}{\partial t}+ \\
&\qquad \alpha\left(\sqrt{\frac{l+1}{2}}\frac{\partial C_{l+1,m,n}}{\partial x}+\sqrt{\frac{l}{2}}\frac{\partial C_{l-1,m,n}}{\partial x}+\frac{u}{\alpha}\frac{\partial C_{l,m,n}}{\partial x}\right)+ \\
&\qquad \beta\left(\sqrt{\frac{m+1}{2}}\frac{\partial C_{l,m+1,n}}{\partial y}+\sqrt{\frac{m}{2}}\frac{\partial C_{l,m-1,n}}{\partial y}+\frac{v}{\beta}\frac{\partial C_{l,m,n}}{\partial y}\right)+ \\
&\qquad \gamma\left(\sqrt{\frac{n+1}{2}}\frac{\partial C_{l,m,n+1}}{\partial z}+\sqrt{\frac{n}{2}}\frac{\partial C_{l,m,n-1}}{\partial z}+\frac{w}{\gamma}\frac{\partial C_{l,m,n}}{\partial z}\right)+ \\
&\quad -\frac{\Omega}{\omega}\left[\frac{\sqrt{2l}}{\alpha}E_x C_{l-1,m,n}-\frac{\sqrt{2m}}{\beta}E_y C_{l,m-1,n}-\frac{\sqrt{2n}}{\gamma}E_z C_{l,m,n-1}\right]+ \\
&\qquad \frac{\Omega}{\omega}B_x\left[C_{l,m-1,n-1}\sqrt{mn}\left(\frac{\beta}{\gamma}-\frac{\gamma}{\beta}\right)+\right. \\
&\qquad C_{l,m+1,n-1}\left(\frac{\beta}{\gamma}\sqrt{n(m+1)}\right)+C_{l,m,n-1}\left(\frac{v}{\gamma}\sqrt{2n}\right)+ \\
&\qquad \left.-C_{l,m-1,n+1}\left(\frac{\gamma}{\beta}\sqrt{m(n+1)}\right)-C_{l,m-1,n}\left(\frac{w}{\beta}\sqrt{2m}\right)\right]+ \\
&\qquad \frac{\Omega}{\omega}B_y\left[C_{l-1,m,n-1}\sqrt{nl}\left(\frac{\gamma}{\alpha}-\frac{\alpha}{\gamma}\right)+\right. \\
&\qquad C_{l-1,m,n+1}\left(\frac{\gamma}{\alpha}\sqrt{l(n+1)}\right)+C_{l-1,m,n}\left(\frac{w}{\alpha}\sqrt{2l}\right)+ \\
&\qquad \left.-C_{l+1,m,n-1}\left(\frac{\alpha}{\gamma}\sqrt{n(l+1)}\right)-C_{l,m,n-1}\left(\frac{u}{\gamma}\sqrt{2n}\right)\right]+ \\
&\qquad \frac{\Omega_s}{\omega}B_z\left[C_{l-1,m-1,n}\sqrt{mn}\left(\frac{\alpha}{\beta}-\frac{\beta}{\alpha}\right)+\right. \\
&\qquad C_{l+1,m-1,n}\left(\frac{\alpha}{\beta}\sqrt{m(l+1)}\right)+C_{l,m-1,n}\left(\frac{u}{\beta}\sqrt{2m}\right)+ \\
&\qquad \left.-C_{l-1,m+1,n}\left(\frac{\beta}{\alpha}\sqrt{l(m+1)}\right)-C_{l-1,m,n}\left(\frac{v}{\alpha}\sqrt{2l}\right)\right]=0
\end{aligned}
\tag{4.26}
$$

As we will see in the next section, the first order coefficients are linearly related to the moments of the distribution functions. Therefore the equations for the low order coefficients are equivalent to the fluid equations.

Fluid moments

The evolution of the fields requires the particle moments, which are given by

$$n(\mathbf{x},t) = \iiint f(\mathbf{x},\mathbf{v},t)dv_x dv_y dv_z = \alpha\beta\gamma \iiint f d\xi_x d\xi_y d\xi_z$$
$$= \alpha\beta\gamma C_{0,0,0} \quad (4.27)$$

$$V_x(\mathbf{x},t) = \iiint v_x f(\mathbf{x},\mathbf{v},t)dv_x dv_y dv_z =$$
$$\alpha\beta\gamma \iiint \sum_{p,q,r} C_{p,q,r}(\mathbf{x},t) \left(\alpha\sqrt{\frac{p+1}{2}}\Psi_{p+1} + \alpha\sqrt{\frac{p}{2}}\Psi_{p-1} + u\Psi_p\right)$$
$$\Psi_q\Psi_r d\xi_x d\xi_y d\xi_z = \alpha\beta\gamma\left(\alpha\sqrt{\frac{1}{2}}C_{1,0,0} + uC_{0,0,0}\right) \quad (4.28)$$

and similarly:

$$V_y(\mathbf{x},t) = \alpha\beta\gamma\left(\beta\sqrt{\frac{1}{2}}C_{0,1,0} + vC_{0,0,0}\right) \quad (4.29)$$

$$V_z(\mathbf{x},t) = \alpha\beta\gamma\left(\gamma\sqrt{\frac{1}{2}}C_{0,0,1} + wC_{0,0,0}\right) \quad (4.30)$$

4.1.2 Initialization

For the simulation an initial particle distribution function $f_0(\boldsymbol{x},\boldsymbol{v})$ has to be specified, and all the initial Hermite coefficients needed for the expansion of the distribution function have to be computed. The fidelity of the expansion depends on the choice of parameters in the Hermite expansion. If the expansion uses P, Q, and R harmonics in the x, y, and z direction, respectively, the expression of the distribution function has $P \times Q \times R$ coefficients that have to be determined. At $t = 0$ we assume a distribution function in the form of a product of shifted Maxwellians:

$$f_0(\boldsymbol{x},\boldsymbol{v}) = \frac{W}{\pi^{\frac{3}{2}}V_{th,x}V_{th,y}V_{th,z}} \times$$
$$\exp\left\{-\left[\left(\frac{v_x - V_{sh,x}}{V_{th,x}}\right)^2 + \left(\frac{v_y - V_{sh,y}}{V_{th,y}}\right)^2 + \left(\frac{v_z - V_{sh,z}}{V_{th,z}}\right)^2\right]\right\} \quad (4.31)$$

The weight W specifies the relative density of the selected species, when the total density is normalized to 1. For the Hermite expansion we use the following set of substitutions:

$$\xi_i = \frac{v_i - v_{sh,i}}{\alpha_i}, \tag{4.32}$$

where i indicates one of the three directions x, y, z. The six parameters α_i and $v_{sh,i}$ (corresponding to α, γ, β and u, v, w in Section 4.1) are inputs to the code and their values are chosen at the start of the simulation to capture correctly the initial distribution function, and its subsequent evolution.

Usually when a Hermite expansion is used in plasma theory the α_i are chosen to be the same at the thermal velocities $V_{th,i}$. However, in the simulation they, together with the shift velocities $v_{sh,i}$, are parameters which have to be chosen to best capture correctly both the initial distribution function and its evolution during the simulation. One way to view this is that the choice of the α_i and $v_{sh,i}$ effectively defines the volume of velocity space for which the Hermite expansion contains information. Then the total number of Hermite harmonics PQR defines the level of detail that can be resolved in the distribution function during its evolution. In the tests we describe below we usually choose α_i to be slightly larger than the initial corresponding thermal velocity. But the choice is dependent on the problem being simulated. For example, if an initially cold distribution suffered strong heating (i.e., spreading in velocity space), the Hermite expansion parameters would have to be chosen to capture both the velocity space region of interest at the end of the simulation as well as to resolve the detail of the initial distribution function. Similar considerations arise for situations where the bulk velocity has large perturbations (i.e., the distribution function fluctuates over a volume in velocity space) or where there is resonant behaviour which might only affect a small region of velocity space. In general α_i should be chosen slightly larger than the thermal velocities if it is possible to foresee an increase in the latter.

Using the property of the Hermite basis:

$$\int_{-\infty}^{\infty} \Psi_n(\xi)\Psi^m(\xi)d\xi = \delta_{n,m}, \tag{4.33}$$

we can compute the Hermite coefficients from

$$\iiint_{-\infty}^{\infty} f(\boldsymbol{x}, \boldsymbol{v}, t)\Psi^p(\xi_x)\Psi^q(\xi_y)\Psi^r(\xi_z)d^3\xi = C_{p,q,r}, \tag{4.34}$$

where:

$$\Psi^n(\xi) = (2^n n!)^{-1/2} H_n(\xi), \tag{4.35}$$

We compute the initial $t = 0$ values of the Hermite coefficients with numerical integration (using Guassian quadrature routines from the `gsl` library). The current implementation of the code assumes an initial uniform bi-Maxwellian velocity space distribution function. The structure of the code allows perturbations to be added to this distribution function and to the magnetic field. Because of the perturbations the initial coefficients need to be computed by integration and cannot be evaluated analytically.

4.1.3 Time advancement scheme

The Hermite decomposition for the Vlasov equation is nested in the Current Advance Method (for the field advance) where the former is solved through a splitting of the Vlasov equation [Cheng and Knorr, 1976, Valentini et al., 2007] as follows:

$$\frac{\partial f}{\partial t} + \boldsymbol{v} \cdot \nabla f = 0 \tag{4.36}$$

$$\frac{\partial f}{\partial t} + (\boldsymbol{E} + \boldsymbol{v} \times \boldsymbol{B}) \cdot \frac{\partial f}{\partial \boldsymbol{v}} = 0 \tag{4.37}$$

In the first equation the velocity is considered as parameter, while in the second the position and the fields are considered as parameters. A second order accurate solution Strang [1968] is provided by a splitting scheme in the form :

$$f(\boldsymbol{x}, \boldsymbol{v}, t = N\Delta t) = \left[\Lambda_x(\Delta t/2)\Lambda_v(\Delta t)\Lambda_x(\Delta t/2)\right]^N \, f_0(\boldsymbol{x}, \boldsymbol{v}), \tag{4.38}$$

where $\Lambda_x(t) f(\boldsymbol{x}, \boldsymbol{v}, t)$ and $\Lambda_v(t) f(\boldsymbol{x}, \boldsymbol{v}, t)$ are the solutions at time t of the two previous equations, and $f_0(\boldsymbol{x}, \boldsymbol{v})$ is the initial condition for the distribution function at time $t = 0$

The space advancement and velocity advancement are treated differently. The space advancement involves spatial derivatives, i.e., cells are coupled with their neighbours. Attempting to solve the equation for space advancement implicitly we would have to invert a matrix of $N_{\text{cells}} \times P \times Q \times R$ rows and $N_{\text{cells}} \times P \times Q \times R$ columns. To avoid this computationally heavy work, we solve this operator explicitly using a 2^{nd} order Lax-Wendroff scheme [Press et al., 1992]. The velocity advancement instead involves only velocity derivatives, so the cells are not explicitly coupled; the code uses an implicit GMRES solver taken from the library `MGMRES` [Barrett et al.,

1994, Kelley, 1995, Saad, 2003].

Start-up

Before entering the regular advancement cycle, an initial start-up is required. Starting from the initial condition at $t = 0$, when all the quantities are known, we advect the distribution function by a $\Delta t/2$ using the Λ_x operator:

$$f^*(\boldsymbol{x}, \boldsymbol{v}, \Delta t/2) = \Lambda_x(\Delta t/2) f(\boldsymbol{x}, \boldsymbol{v}, 0). \tag{4.39}$$

Fields at $\Delta t/2$ are computed using an explicit scheme starting from the initial condition. Starting from $f^*(\boldsymbol{x}, \boldsymbol{v}, \Delta t/2)$ we advance the distribution function of Δt with the Λ_v operator:

$$\tilde{f}(\boldsymbol{x}, \boldsymbol{v}, \Delta t) = \Lambda_v(\Delta t) f^*(\boldsymbol{x}, \boldsymbol{v}, \Delta t/2). \tag{4.40}$$

The process is summarized in Fig. 4.1.

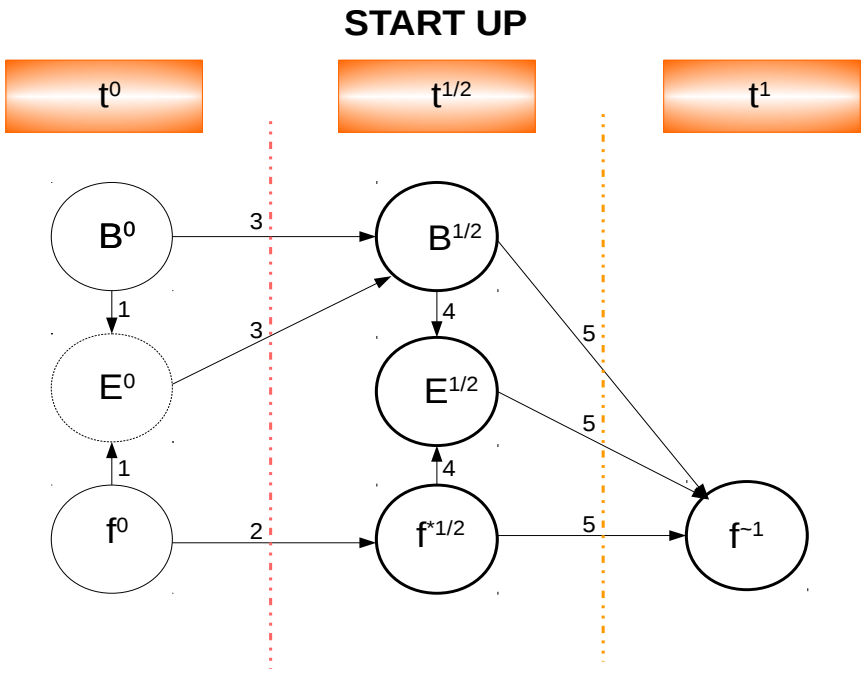

Figure 4.1: Start up scheme. The quantities in dashed circles are known at the beginning, the ones in dashed circles are intermediate quantities, the ones in bold circles are needed at the end.

All the quantities needed to start the computational cycle are now known.

Computational cycle

The quantities known are: $f^*(\boldsymbol{x}, \boldsymbol{v}, t - \Delta t/2)$, $\boldsymbol{E}(\boldsymbol{x}, t - \Delta t/2)$, $\boldsymbol{B}(\boldsymbol{x}, t - \Delta t/2)$ and $\tilde{f}(\boldsymbol{x}, \boldsymbol{v}, t)$, where here we use t to denote a generic full time step i.e. $N\Delta t$. We advance the distribution function in physical space of Δt:

$$f^*(\boldsymbol{x}, \boldsymbol{v}, t + \Delta t/2) = \Lambda_x(\Delta t)\tilde{f}(\boldsymbol{x}, \boldsymbol{v}, t). \tag{4.41}$$

To calculate the fields $\boldsymbol{E}(\boldsymbol{x}, t+\Delta t/2)$ and $\boldsymbol{B}(\boldsymbol{x}, t+\Delta t/2)$ we use the *CAM* method [Valentini et al., 2007]. We position the magnetic field and the electric field on a staggered grid. In this way it is more convenient to compute the respective derivatives. For the latter we need the electric field at t, and, because the electric field is a state quantity, to calculate this the magnetic field and moments have to be evaluated also at t. One can note that, at this stage in the computational cycle, $\tilde{f}$ has had a Δt advancement in the velocity space operator, but is only advanced to $t - \Delta t/2$ with the configuration space operator, whereas f^* has been further advanced in space by Δt to $t + \Delta t/2$. Thus we can use, as an approximation correct to the first in Δt order of the distribution function at time t:

$$f(\boldsymbol{x}, \boldsymbol{v}, t) = \frac{1}{2}(\tilde{f}(\boldsymbol{x}, \boldsymbol{v}, t) + f^*(\boldsymbol{x}, \boldsymbol{v}, t + \Delta t/2)). \tag{4.42}$$

In the same way we can find the moments at the full time step as averages between the 'star' moments and 'tilde' moments. First, the magnetic field at full step is obtained from:

$$\boldsymbol{B}(\boldsymbol{x}, t) = \boldsymbol{B}\left(\boldsymbol{x}, t - \Delta t\right) - \Delta t\left[\nabla \times \boldsymbol{E}\left(\boldsymbol{x}, t - \Delta t/2\right)\right]. \tag{4.43}$$

Now we have all the quantities at full time step and we can also evaluate the electric field, and we use this to obtain $\boldsymbol{B}(\boldsymbol{x}, t + \Delta t/2)$.

$$\boldsymbol{E}(\boldsymbol{x}, t) = -\boldsymbol{v_i}(\boldsymbol{x}, t)\times\boldsymbol{B}(\boldsymbol{x}, t) + \frac{1}{n_e(\boldsymbol{x}, t)}\left(\nabla \times \boldsymbol{B}(\boldsymbol{x}, t)\right)\times\boldsymbol{B}(\boldsymbol{x}, t) - \frac{\nabla p_e(\boldsymbol{x}, t)}{n_e(\boldsymbol{x}, t)} + \eta\boldsymbol{j}(\boldsymbol{x}, t) \tag{4.44}$$

$$\boldsymbol{B}(\boldsymbol{x}, t + \Delta t/2) = \boldsymbol{B}(\boldsymbol{x}, t - \Delta t/2) - \Delta t[\nabla \times \boldsymbol{E}(\boldsymbol{x}, t)]. \tag{4.45}$$

To perform the velocity advance we need $\boldsymbol{E}(\boldsymbol{x}, t + \Delta t/2)$, so the moments at

$t + \Delta t/2$. It is easy to show that:

$$n(\boldsymbol{x}, t + \Delta t/2) = n^*(\boldsymbol{x}, t + \Delta t/2), \tag{4.46}$$

while for the current we obtain an advance equation of the form:

$$\boldsymbol{j}(\boldsymbol{x}, t + \Delta t/2) = \boldsymbol{j}^* (\boldsymbol{x}, t + \Delta t/2) + \Delta t/2[n^* \boldsymbol{E}^* + \boldsymbol{j}^* \times \boldsymbol{B}], \tag{4.47}$$

where 'star' moments and fields are collected and computed from f^*.

Now we have all the quantities required to advance the distribution function in velocity space for Δt, thus concluding the computational cycle.

$$\tilde{f}(\boldsymbol{x}, \boldsymbol{v}, t + \Delta t) = \Lambda_v(\Delta t) f^*(\boldsymbol{x}, \boldsymbol{v}, t + \Delta t/2) \tag{4.48}$$

The computational cycle is summarized in Fig. 4.2.

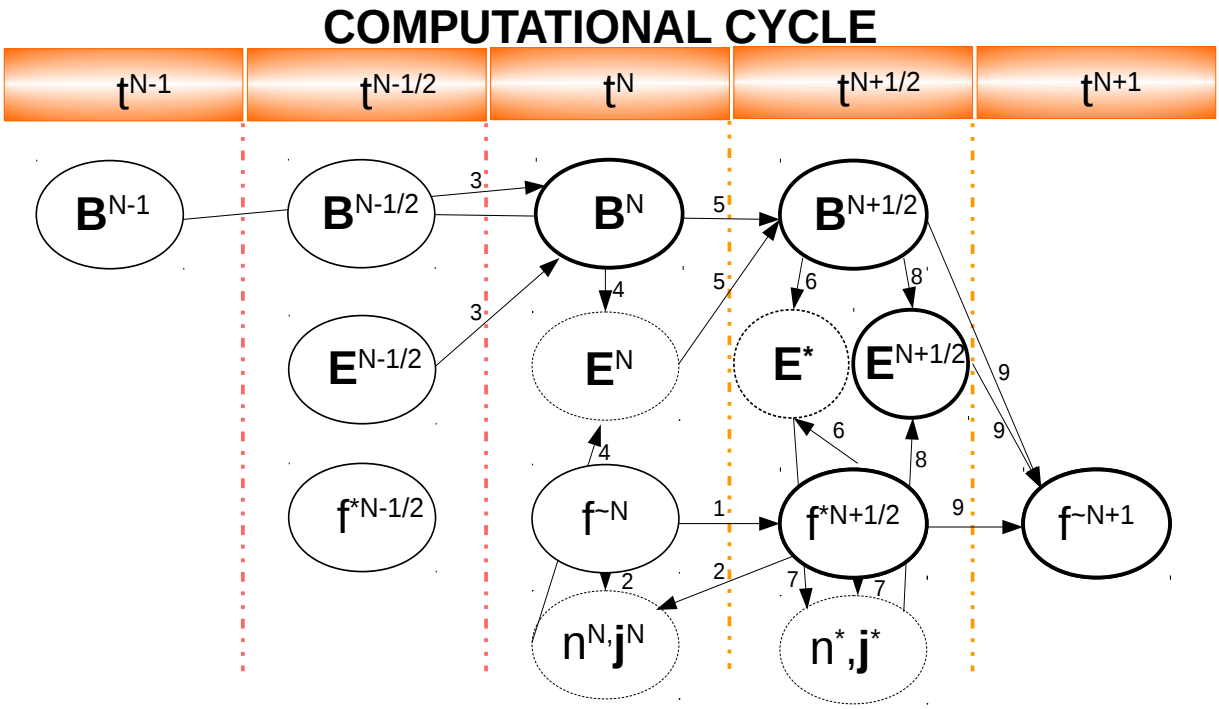

Figure 4.2: Computational cycle. The quantities in solid circles are known at the beginning, the ones in dashed circles are intermediate quantities, the ones in bold circles are needed at the end.

All the magnetic field advancements are performed using a cyclic leapfrog method described in Matthews [1994]. A Lax-Wendroff time advancement scheme is used to perform the physical space advancement [Press et al., 1992], which, although

not particularly sophisticated, has proved sufficiently accurate due to the order of the method and the capability to suppress mesh drifting instability which we will explain in more detail in the last chapter.

4.1.4 The collisional operator

The development of increasingly smaller phase space structures in a collisionless plasma is very well known in plasma physics and typically referred to as the filamentation process. A classical and well-studied example where filamentation occurs is linear Landau damping, i.e., the damping in time of an initial electric field perturbation due to wave-particle resonances. Any discretization of the velocity space is associated with a minimum wavelength that can be resolved, and, therefore, any numerical simulation of the filamentation process with fixed resolution is bound to fail after a certain time. Several fixes have been suggested in the literature in order to overcome the filamentation process in Vlasov simulation codes. They involve some form of filtering or smoothing of the high order moments of the distribution function, or, equivalently, the introduction of a weakly-collisional operator. Here we use a collisional operator modified from the 1D-1V case (since in 1D-1V the expansion only has coefficients in one velocity direction) considered in Camporeale et al. [2016] to be used in the 1D-3V case of our code. In particular we have that the collisional operator C for the coefficient l, m, n where P, Q, R are the total number of harmonics in the 3 directions, is [Delzanno, 2015]:

$$C[C_{l,m,n}] - \nu \left[\frac{l(l-1)(l-2)}{(P-1)(P-2)(P-3)} + \frac{m(m-1)(m-2)}{(Q-1)(Q-2)(Q-3)} + \frac{n(n-1)(n-2)}{(R-1)(R-2)(R-3)} \right] C_{l,m,n} \quad (4.49)$$

we add this to the equations for the coefficients, as an explicit term on the RHS. As we split the distribution function advancement in two parts, we add half of the operator both in the space and velocity advancement. We remark that this collisional operator should not be used when there are less 4 terms in the expansion for each velocity direction. In the tests of the code, we found that the collisional operator was virtually never used, due to the fact that it only operates on the high order Hermite functions. In our simulations the initial conditions were always given by small perturbations of a bi-Maxwellian. In this case the coefficients with high mode number are very close to zero from the beginning and they remain not important for all the simulation.

4.2 Implementation

The algorithm is divided in three parts:

- initialization
- start-up
- computational cycle (repeated)

We will now discuss these stages in more details.

4.2.1 Initialization

Here we describe the implementation of the algorithm which has been carried out using the *C++* programming language. The first stage involves the reading of the input data from *kvf* file, the initialization of all the classes with allocation of memory for the physical quantities and their initialization. The base initial condition class is *UniformIC*, from which all the other initial condition classes inherit. The children classes add perturbations in velocity space and magnetic field to the base class. The initialization is subdivided in the following steps:

- reading of initial condition type from *kvf* file;
- declaration of class for initial condition;
- setting of simulation parameters and other input data;
- initialization of the grid;
- allocation of memory for fields, electron fluid and total moments;
- initialization of magnetic field;
- initialization of electron fluid;
- allocation of memory for Vlasov Sets, objects which contains information about the distribution function of each ion species and partial moments, i.e. moments for single ion species;
- initialization of the coefficents of the distribution function;
- addition of perturbations in magnetic fields and coefficients, depending on the initial condition.

4.2.2 Start up

Once all the coefficients which describe the distribution function are initialized, we perform the following steps:

- moments computation at time zero
- electric field calculation at time zero
- space advancement of the distribution function of half time step and 'star' moments computation
- explicit fields advance to half time step
- velocity full time step advancement

We are now ready to start the computational cycle.

4.2.3 Computational cycle

The sequence of steps which are required to advance the time step is given by:

- 'tilde' moments computation
- space advancement or the distribution function of a full time step
- 'star' moments computation
- moments average at full time step
- magnetic field advancement to half time step and electric field prediction using 'star' moments
- current advancement
- electric field correction
- velocity advancement of the distribution function of full time step

All the quantities are updated and the cycle can start from the beginning for the next time step.

4.3 Test cases

In this section we describe a number of tests which demonstrate the Hermite-Vlasov-hybrid (HVH) method in a 1D-3V (periodic in space) implementation. We note that for all these tests the collisional operator is either not used or has little effect, as the initial distributions are already Maxwellian and remain close to Maxwellian through the simulation. Thus the only non-zero Hermite coefficients are those with small indices (< 2) and this is true for all the simulations shown. In this case the collisional operator does not affect those coefficients, but only the ones with larger indices which are equal to, or close to zero and which will not be changed by the use of the collisional operator.

4.3.1 "Quiet" Maxwellian

An initial test for any plasma code is a uniform Maxwellian equilibrium. Provided that the expansion parameters α_i are chosen to match the thermal velocity of the distribution function (in this case a uniform, stationary, isotropic Maxwellian) the numerical method introduces no perturbations, and all initially zero quantities remain zero throughout the simulation. Consequently the initial equilibrium is perfectly preserved. This is due to the Hermite decomposition perfectly capturing the distribution function, and its low-order moments in the low harmonics of the expansion, so that with no gradients in fields or low-order moments, the higher Hermite harmonics never change. This is a major advantage with respect to PIC, where even a quiet Maxwellian can have numerical heating or cooling due to particle noise (i.e. thermal velocities change in time).

As a more realistic test of a plasma with an isotropic Maxwellian distribution, we perturb the exact Maxwellian equilibrium with small amplitude random fluctuations in the magnetic field. We choose intial $\beta_i = 0.1$, $\gamma_e = 1.0$, where β_i and γ_e are respectively the ratio between ion pressure and the magnetic pressure, and the electron diabatic index, $T_{e,0} = 1$, a cell size of $\Delta x = 0.1$, and time step $\Delta t = 0.002$, where lengths are normalized to the ion inertial length, times to the inverse of ion cyclotron frequency and velocities to the Alfvén speed. We set a uniform mean magnetic field with $B_x = B_0 = 1$ in the x direction (the direction of the simulation) and we add random perturbations in B_y and B_z with a maximum magnitude of 1% of B_0. We run the simulation with 1000 cells for 30000 time steps. By choosing the mean magnetic field to be in the x direction, the consequent fluctuations will be parallel propagating, and, since the simulation is unidimensional, B_x is constant

(from $\nabla \cdot \boldsymbol{B} = 0$), and therefore all magnetic field fluctuations are transverse to the mean field direction. The ions have an isotropic Maxwellian distribution with $\beta_i = 0.1$. For the simulation shown, $\alpha_{x,y,z} = 0.25$ and a total of $10 \times 10 \times 10$ Hermite harmonics was used to capture both the initial distribution function and its subsequent velocity fluctuations.

Figure 4.3 shows the time-space evolution of the system over the simulation as colour maps of B_y, (similar to B_z) E_x, and density n. Propagating fluctuations over a range of wavelengths can be seen in all the field components, and also the density, which starts initially uniform. By taking the Fourier transform in time and space, we also show the dispersion properties of the plasma by plotting the power in frequency – wavevector ($\omega - k$) space for the B_y field component. The peaks in this representation trace out the dispersion relation of the plasma, and two modes can be identified corresponding to right-handed (whistler) and left-handed (Alfvén ion cyclotron) polarizations. As expected, while the right-handed mode propagates to larger k and ω, the left handed is damped as it approaches the ion cyclotron frequency.

We run some some other tests for the "Quiet" Maxwellian, where the parameters $\alpha_{x,y,z}$ were significanty smaller or bigger than the thermal velocities. In both cases the simulation fails to capture the dispersion relation correctly and the simulation diverges before the final time.

4.3.2 Two fluid waves

In order to test the code quantitatively for its wave propagation properties, especially at the transition from MHD to kinetic (dispersive) scales, we have simulated linear waves as derived in two fluid theory. An initially sinusoidal fluctuation was used with given wavelength, and with the mean magnetic field in the x direction. The initialization of the magnetic field and velocity components was taken from Zhao et al. [2014] adapted to parallel propagation, setting the angle between the wave vector and magnetic field to zero, i.e., $\theta_{kB} = 0$. We performed a set of simulations where we varied the wavelength of the initialized wave between 2 and 100 ion inertial lengths; the dimension of the simulation box was varied to be able to maintain periodic boundary conditions. We set $\beta_i = 0.1$, $\alpha_{x,y,z} = 0.05$, $\Delta x = 0.5$ and $\Delta t = 0.02$ and we run the simulation for 1000 steps using 8 Hermite functions in each direction. We used the simulation data to compute the actual wave velocity of propagation, k and ω of the propagating wave, and carried out simulations for both right- and left-hand polarized wave modes. Figure 4.4 shows k and ω measured from

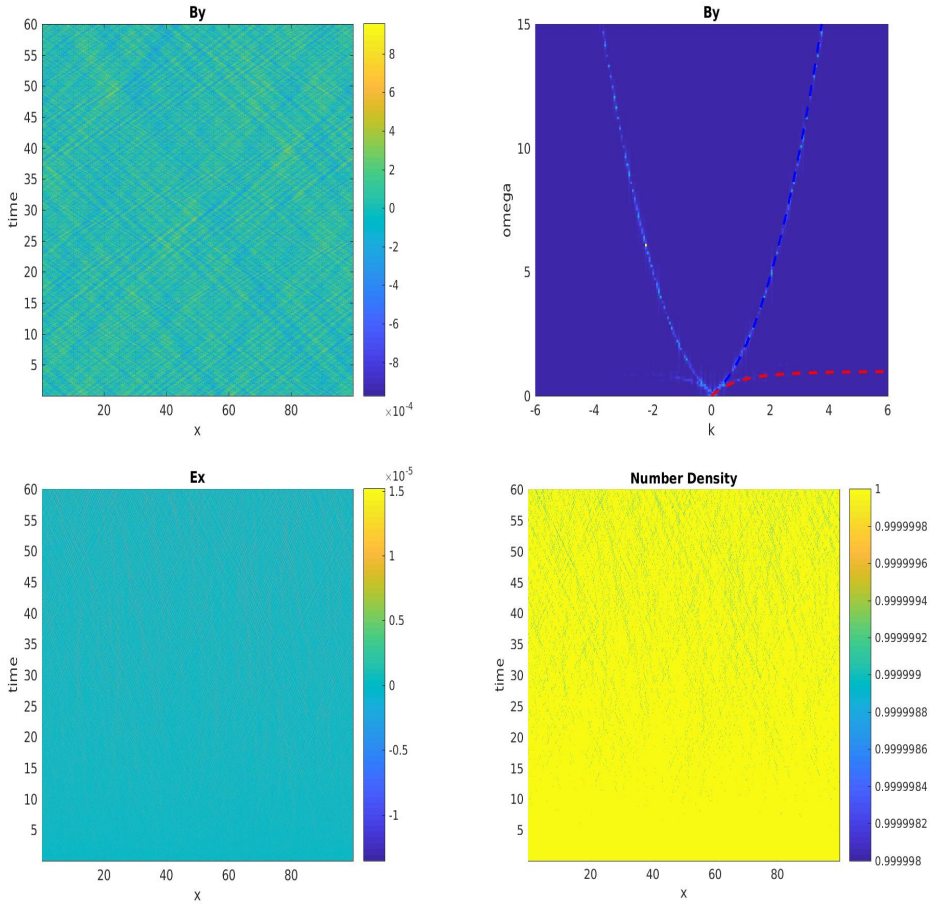

Figure 4.3: Time evolution of magnetic field component B_y (top left), its dispersion relation with dashed theory lines in blue (right hand circularly polarized mode) and red (left hand circularly polarized ,mode) (top right), evolution of electric field component E_x (bottom left) and evolution of number density n (bottom right).

the simulations, compared with the prediction of linear two-fluid theory [Zhao et al., 2014]. It is clear that the simulation code accurately reproduces the linear waves from two-fluid theory.

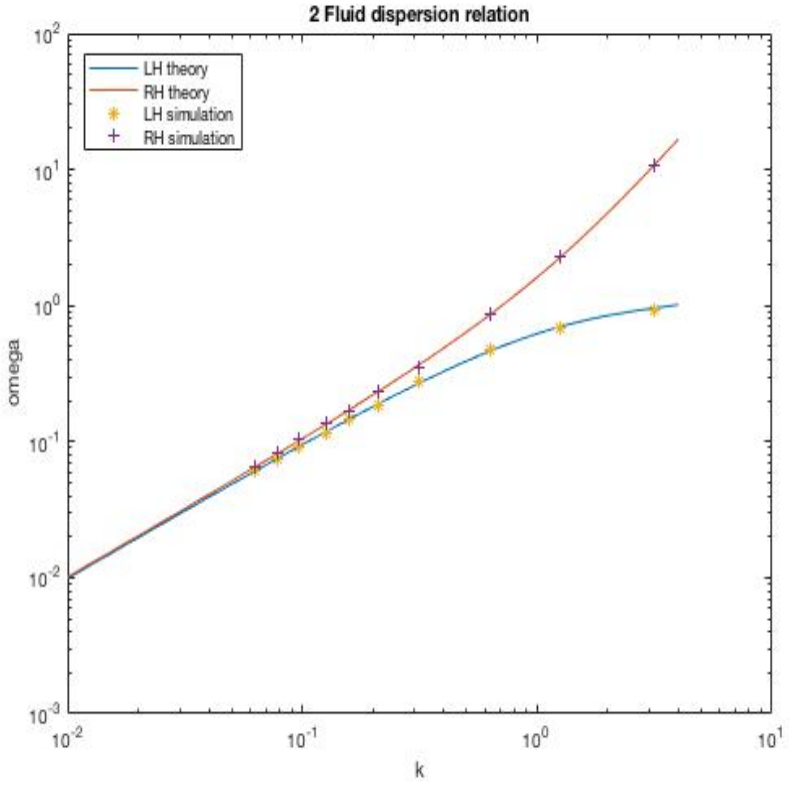

Figure 4.4: Comparison of dispersion properties (normalized frequency ω/Ω_i and wave vector kc/ω_i) of small amplitude waves between results from simulation data and two-fluids linear wave theory.

5 Ion temperature anisotropy instabilities

In this chapter we will focus on a type of plasma microinstability which happens due to ion temperature anisotropies. For more details we refer the reader to Gary [1993]. We consider here electromagnetic fluctuations in a homogeneous, magnetized plasma, admitting anisotropies in the ion distribution function. In particular the latter is made by a two-temperature (parallel and perpendicular) bi-Maxwellian, which allows the growth of such instabilities. Due to the nature of the hybrid algorithm we developed we focus on instabilities given by anisotropies in the ions temperature. In fact in this kind of codes the electrons are treated like fluids (i.e. their distribution function is in Maxwellian equilibrium) with a scalar pressure and the temperature is isotropic. Also, electron time scales are much smaller than those of ions and any associated instabilities happen on a time scale which is not observed with the hybrid approximation.

We will focus here mainly on instabilities with $\frac{T_\perp}{T_\parallel} > 1$, where the latter is called the temperature anisotropy ratio. This condition is commonly observed in space plasma. There are three instabilities of interest: ion firehose (driven by a parallel anisotropy $T_\perp/T_\parallel < 1$), mirror and Alfvén ion-cyclotron (AIC) (both driven by a perpendicular anisotropy $T_\perp/T_\parallel > 1$). Examples of all of these are observed in the solar wind [e.g., Hellinger et al., 2006, Matteini et al., 2012, Schwartz et al., 1996], the linear theory has been extensively investigated (see book by Gary [1993]), and numerous PIC simulations have been carried out covering the whole range of possible instabilities [e.g., Hellinger and Trávníček, 2008, McKean et al., 1994, Riquelme et al., 2015]. Observational data on solar wind have been collected in [Bale et al., 2009, Gary et al., 2001, Hellinger et al., 2006, Kasper et al., 2002, Matteini et al., 2013] and are shown in Fig. (5.1). We can see here that the proton cyclotron instability has more observational points compared to the proton firehose instability.

In collisionless plasmas there are multiple mechanisms which can generate temperature anisotropy, such as high Mach number shocks, plasma expansion or compression, and such plasmas can be linearly unstable to a range of plasma microin-

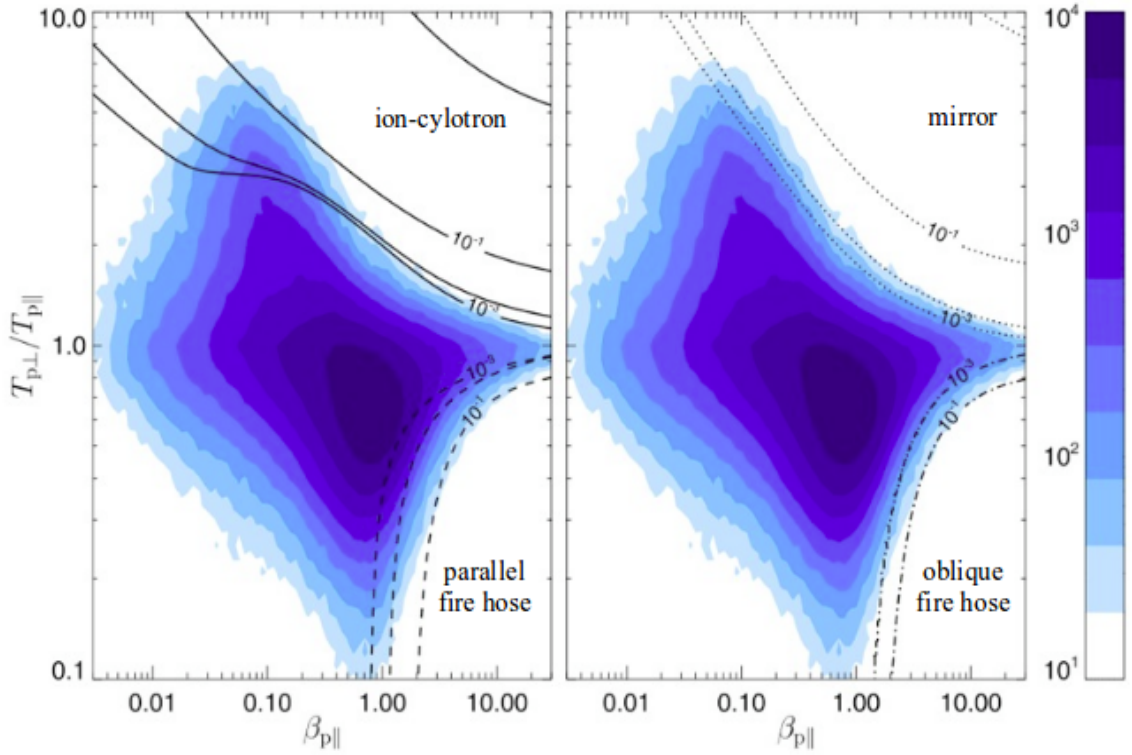

Figure 5.1: Observational data on temperature anisotropy instability showing the probability distribution of observations and the threshold for different types of instabilities. For each combination $\beta_{p,}$, $T_{p,\perp}/T_{p,\parallel}$ the graph reports then number of observations cases in the solar wind. The threshold for the different instabilities and iso-γ contours show that the ion-cyclotron instability is the most observed. Source: Hellinger et al. [2006]

stabilities. Consequently temperature anisotropy instabilities are a common feature of such plasmas, and have been extensively studied, particularly in the context of space plasmas.

This chapter is organized as follows: first we will show the three different types of ion anisotropy instabilities and discuss how to find the thresholds for those to develop. Then we will focus on the study of a particular instability, carrying out some simulations with the *HVH* code. Finally we will perform some comparisons with the *CAM-CL* PIC hybrid code of which we described the implementation in Chapter 3. Details are from [Gary, 1993].

5.1 The instabilities

In this section we present the three different ion anisotropy instabilities and show how to compute the thresholds for them to develop, which are the minimum values

of temperature anisotropy ratio which give a linear growth rate > 0.

5.1.1 The ion firehose instability

The ion firehose instability can develop in a plasma with β_i large enough and $T_{\parallel,i} > T_{\perp,i}$. The ions resonate with this instability at a resonance frequency comparable to the ions cyclotron frequency, i.e. when the ions move at a velocity $\approx \Omega_i/k$ where k is the wave number of the propagating wave, energy is transferred from the particles to the wave, making therefore the wave growing, and it can have maximum growth rate for parallel propagation (parallel firehose instability) or for oblique propagation (oblique firehose instability). In this direction it is right-hand circularly polarized and when the anisotropy increases it evolves out of the magnetosonic/whistler wave. The electrons are nonresonant, which means the growth rate does not depend on T_e/T_i.

5.1.2 The ion cyclotron anisotropy instability (AIC)

The ion cyclotron anisotropy instability may grow in a plasma where $T_{\perp,i} > T_{\parallel,i}$ if $\beta_i < 6$ and $T_e \approx T_i$. It has maximum growth rate for parallel propagation and in this direction it is left hand circularly polarized. If the anisotropy is increased the instability evolves into the Alfvén proton cyclotron wave. Also in this case the electrons are non resonant so their temperature does not influence the growth rate.

5.1.3 The mirror instability

Another type of instability which might also occur for $T_{\perp,i} > T_{\parallel,i}$ is the mirror instability. It was first described by Chandrasekhar et al., [Chandrasekhar, 1958]. The mode is Landau resonant, i.e. energy is transferred from the particles to the wave, for $\omega_r = 0$ for uniform plasmas. The maximum growth rate is for directions oblique to the background magnetic field. The fluctuations of the magnetic field are substantially different from the previous two cases as they have an important longitudinal component (i.e. $\delta\boldsymbol{B} = \delta\boldsymbol{B}_\perp + \delta\boldsymbol{B}_\parallel$). However, Gary [Gary et al., 1976],[Gary, 1992] used linear theory to show that in a plasma with equal electrons and ions temperatures and bi-Maxwellian distributions the ion cyclotron anisotropy has a lower threshold (for $\beta_i \leq 6$) and the latter has a large growth rate in many cases. Therefore the mirror instability is less frequently observed.

5.1.4 Instability thresholds

The linear growth rate $\gamma(\boldsymbol{k})$ for these instabilities is a function of the temperature anisotropy ratio and the plasma beta. In particular, considering an instability driven by an anisotropy in the j^{th} species, $\gamma(\boldsymbol{k}) = \gamma(\beta_{\parallel,j}, R_j)$, where $R_j = T_{\perp,j}/T_{\parallel,j}$ Maruca [2012]. Considering the plane having these two dimensionless parameters as coordinates, we can separate it in two regions: one stable and one unstable. The separation is done finding the line which has $\gamma_{max}(\beta_{\parallel,j}, R_j) = 0$. The region which has

$$\gamma_{max}(\beta_{\parallel,j}, R_j) > 0$$

is considered unstable. A value of $\gamma_{max} = 10^{-3}\Omega_i$ is generally considered as the minimum for the instability to develop and is used to find the threshold. The latter is a curve (ideally monotonic) in the plane $(\beta_{\parallel,j}, R_j)$ which defines a minimum value of R_j for every values of $\beta_{\parallel,j} > 0$ for the instability to develop. Notice that γ_{max} is given in term of the ion cyclotron frequency and can be seen as the inverse of the time that takes for the instability to affect the plasma. The minimum value of 10^{-3} for γ_{max} for the propagation to be considered unstable is purely conventional. However this value allows the instability to be observable in times of interest.

The threshold curves are found through data fitting. In literature we can find different types of fitting.

Samsonov et al. [2001] give a relation of the type:

$$\frac{T_{\perp,i}}{T_{\parallel,i}} = 1 + \frac{a}{\beta^b_{\parallel,i}}, \tag{5.1}$$

where:

- $a \approx 0.45$, $b \approx 0.40$ for ion cyclotron instability;
- $a \approx 0.74$, $b \approx 0.73$ for mirror instability;

The AIC is observed in fast solar wind Gary et al. [2001] and in slow solar wind Hellinger et al. [2006]. The former is often composed of beam and core components and core ions (neglecting the beam component) do not follow the previous relations. Marsch et al. [2004] give a relation for core ion population:

$$\frac{T_{\perp,c}}{T_{\parallel,c}} \approx \frac{a}{\beta^b_{\parallel,c}}, \tag{5.2}$$

with $a \approx 1.16$ and $b \approx 0.55$, but it is not well understood.

For parallel and oblique firehose instabilities R_j is smaller than one so a assumes negative values and the threshold gives the maximum value of R_j for the instability to develop. Gary et al. give the same formulation:

$$R_i = 1 + \frac{a}{\beta_{\parallel,i}^b}, \tag{5.3}$$

where $a \approx -0.66$ and $b \approx 0.56$.

Hellinger et al. [2006] give a single formulation now depending on three parameters:

$$\frac{T_{\perp,i}}{T_{\parallel,i}} = 1 + \frac{a}{(\beta_{\parallel,i} - \beta_0)^b}, \tag{5.4}$$

- $a \approx 0.43$, $b \approx 0.42$ and $\beta_0 \approx -0.0004$ for ion cyclotron instability;
- $a \approx 0.77$, $b \approx 0.76$ and $\beta_0 \approx -0.016$ for mirror instability;
- $a \approx -0.47$, $b \approx 0.53$ and $\beta_0 \approx 0.59$ for parallel firehose instability;
- $a \approx -1.4$, $b \approx 1.0$ and $\beta_0 \approx -0.11$ for oblique firehose instability;

The latter threshold lines are shown in Fig.(5.2). On the left panel we can see the lines for instabilities with $\frac{T_{\perp,i}}{T_{\parallel,i}} > 1$. We have used a log-log plot because the value of R_i grows rapidly for very small beta. We can see that for small beta the limit for the AIC is lower than the one of the mirror instability, so the former can develop more easily. When β approaches the value of 6 we notice an inversion, i.e. the threshold for the mirror instability becomes lower as we previously mentioned.

5.2 A proton cyclotron instability study

Any linear instability grows from some pre-existing, or assumed fluctuations, and for PIC simulations that is usually the initial particle noise, which for standard PIC methods limits the dynamic range of instability growth unless an exceptionally large number of particles per cell is used [e.g., Florinski et al., 2016]. Since it has no initial noise (so that the level of initial fluctuations is a simulation parameter) the Vlasov-Hybrid code is particularly suitable to simulate low growth rate instabilities such as the ones which arise in turbulence when an ion temperature anisotropy is created by the turbulent flows compressing or expanding the plasma [e.g., Hellinger et al., 2017].

Here, as a test of the HVH method, we study the evolution of the AIC instability driven by a perpendicular temperature anisotropy. This has a growth rate which

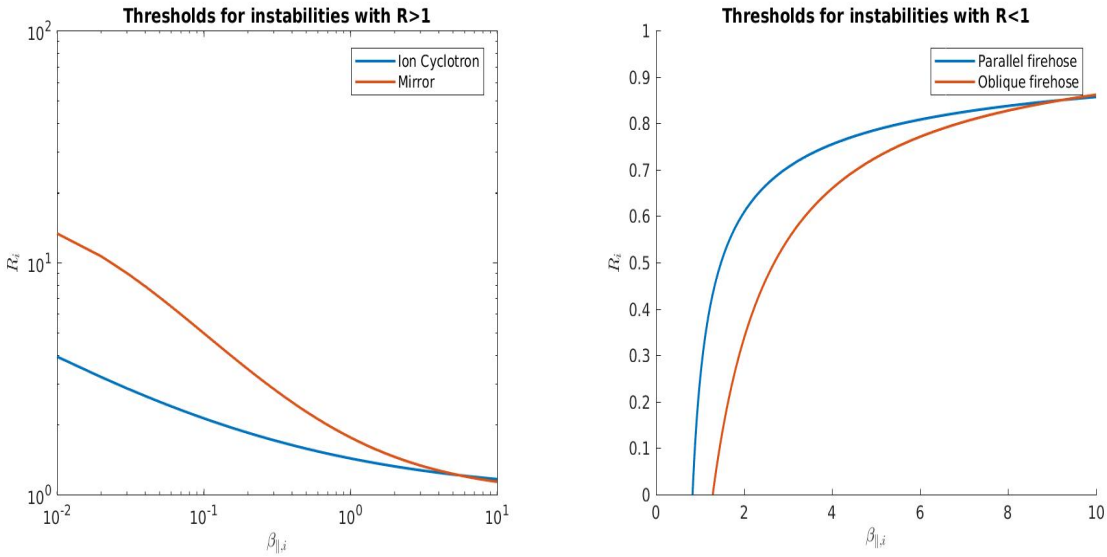

Figure 5.2: Left panel: threshold lines for ion cyclotron and mirror instabilities, which are unstable above the threshold's lines; right panel: threshold lines for parallel and oblique firehose instabilities, which are unstable below the threshold's lines. The lines are obtained with the formulation given by Hellinger et al. [2006].

maximises at parallel propagation $\boldsymbol{k} \cdot \boldsymbol{B} = 0$, and in this case there is no competition with the mirror mode which has $\boldsymbol{k}$ oblique to $\boldsymbol{B}$. The unstable wave is on the left-hand ion-cyclotron branch, and the magnetic fluctuations are circularly polarized. The maximum growth rate decreases with decreasing temperature anisotropy ratio, and the wavelength corresponding to maximum growth is of the order of 5 – 20 ion inertial lengths, and decreases with increasing temperature anisotropy ratio. Thus for low growth rates, when the anisotropy is small, the wavelength of maximum growth is of the order of 10 c/ω_{pi}, which puts this instability squarely in the domain of hybrid simulations, which typically have a cell size of 0.5 c/ω_{pi}.

We show results for both the linear (growth) and nonlinear (saturation) stages of an AIC instability for $\frac{T_{perp}}{T_{par}} = 2.5$ and $\beta_{i,\|} = 1.0$. For this value of $\beta_{i,\|}$ the threshold condition is $R_i = 1.43$ which is fully satisfied. Using a linear wave solver [Camporeale and Burgess, 2017] we find the wave vector k_m of the fastest growing mode and the correspond growth rate γ_m of the instability. For the chosen simulation parameters $k_m = 0.545344\ w_{pi}/c$ and $\gamma_m = 0.102827\ \Omega_i$. For the simulation we set the domain to be 5 times the wavelength corresponding to k_m (i.e., mode 5). We initialize the magnetic field with small-amplitude random fluctuations in order to seed the growth of the instability.

Figure 5.3 shows the early-time period in the simulation where there is exponential

growth of the wave amplitude, i.e., the system behaves as expected for a linear instability. The time-space evolution of the field component B_y shows the growth of a propagating mode. The growth of the mode can be seen in the left-hand panel which shows the natural log of the field amplitude averaged over all cells plotted against time. Initially the growth is slower than exponential, due to the effects of the initial conditions, and the fact that different modes maybe growing, or indeed damping. Eventually, after $40\Omega^{-1}$ the growth becomes exponential as the system is dominated by a single mode, which is the most rapidly growing one. The dominant mode in the simulation is mode 5, as expected from k_m. The measured amplitude growth rate from the simulation was found to be very close to the linear theory prediction, with $\gamma_m[\text{sim}] = 0.1023\ \Omega_i$.

For the simulation shown we used Hermite expansion parameters of $\alpha_{x,y,z} = 1.0$ and a total of $10 \times 10 \times 10$ harmonics. For a fixed number of harmonics the error on the growth rate increased as $\alpha_{x,y,z}$ increased, so that for $\alpha_{x,y,z} = 1.2$ the error on the linear growth rate was about 10%. Reducing significantly $\alpha_{x,y,z}$ again produced errors in the growth rate, and, for sufficiently small values, the instability was not even properly captured, since the initial distribution was not accurately modelled. Note that since the temperature anisotropy implies a lower thermal velocity in the x direction, it would be a possibility to try to use different values for the $\alpha_{x,y,z}$ to reflect the anisotropy of the distribution. However, it was found that more accurate and reliable results were found when the $\alpha_{x,y,z}$ all had the same value. This is particular relevant to the later, nonlinear stage of the instability where the temperature anisotropy is reduced as the growth saturates.

Fixing $\alpha_{x,y,z} = 1.0$, we varied the maximum number of Hermite harmonics in the decomposition, to test convergence. Using the linear growth rate as a metric of goodness, we found convergence as the number of harmonics was increased from $6 \times 6 \times 6$. However, increasing this beyond $10 \times 10 \times 10$ the error on $\gamma_m[\text{sim}]$ starts to grow. We believe this is due to errors in the matrix inversion. In fact when we have 10 functions in each direction we have a $10 \times 10 \times 10 = 1000$ squared matrix to invert. Increasing to a $12 \times 12 \times 12 = 1728$ squared matrix to solve, leads to the use of a very large number of elements. Since our initial condition is a bi-Maxwellian all the coefficients of high order are very close to 0 ($< 10^{-16}$) and practically zero. Thus, there is a point where the error introduced in the inversion of the matrix when increasing the number of functions is predominant compared to the improvement in the representation of the distribution function. We denote that the theoretical convergence properties of GMRES methods state that after m iterations, where m is the size of the matrix to invert, the method should give the exact solution. However

these kinds of methods are usually truncated after few iterations and it is possible that even remaining below a certain value for the error, the error is amplified.

Figure 5.4 shows the evolution of the instability to later times, showing (in the left panel) how the growth saturates around time 120 Ω_i^{-1}. This corresponds to the time that the temperature anisotropy of the ion distribution starts to be reduced by nonlinear wave-particle interactions (right-hand plot). This type of behaviour is expected from comparable PIC-hybrid simulations, although the initial level of fluctuations is much higher in the PIC case, and so saturation is reached much earlier in the simulation.

We compared simulations with 6^3 and 10^3 expansion functions - energy conservation is good in all cases, varying from a relative error on total energy of 10^{-7} to 10^{-8} increasing number of harmonics.

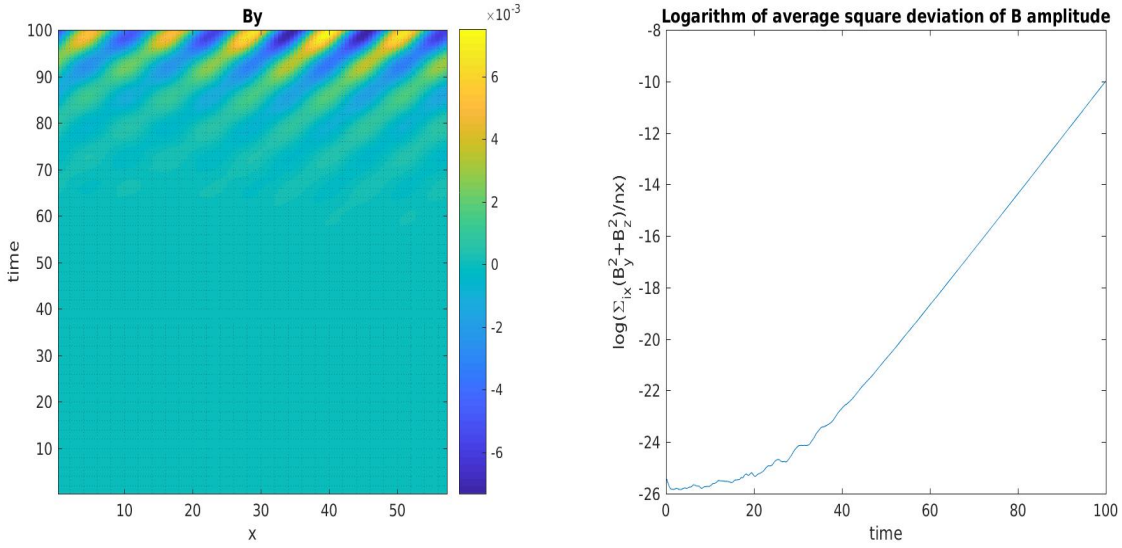

Figure 5.3: Left panel: time evolution of magnetic field in y direction; right panel: logarithm of average square deviation of magnetic field amplitude . The simulation is run for 5000 time steps i.e. 100 Ω_{ci}^{-1}.

5.2.1 Influence of Hermite parameters

In the previous paragraph we stated that the error on the linear growth rate depends on the $\alpha_{x,y,z}$ parameters. Here we want to underline how this is a weakness of the method and how it is extremely important to carefully choose the alphas.

In Tab. 5.1 we show the error on the linear growth rate varying the Hermite parameters. We notice that the error changes of 2-3 order of magnitudes for small variations of the parameters. In Fig. 5.2.1 we show the evolution of the magnetic

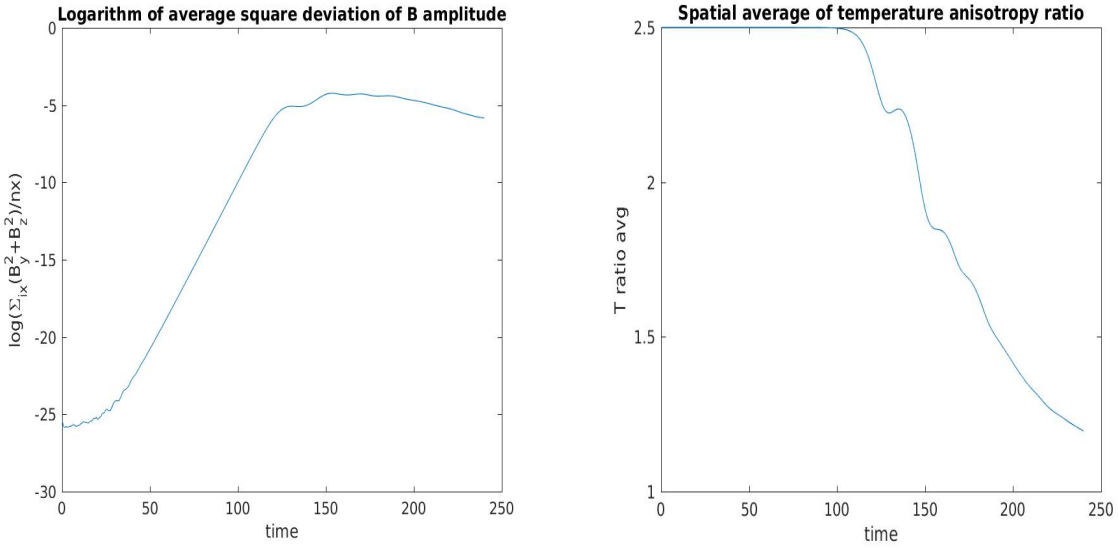

Figure 5.4: Left panel: logarithm of average square deviation of magnetic field amplitude; right panel: cell averaged temperature anisotropy ratio. The simulation is run for 12000 time steps i.e. 240 Ω_{ci}^{-1}.

α_x	α_y	α_z	γ	$_a$	E_r
1.2	1.2	1.2	0.1130525	0.010225	9.95%
1	1	1	0.102863	0.000036	0.04%
0.9	0.9	0.9	0.099949	0.002878	2.80%
0.85	0.85	0.85	0.100796	0.002031	1.98%
0.7071	1.118	1.118	0.094708	0.009119	8.87%

Table 5.1: Linear growth rate, relative and absolute errors varying the Hermite parameters. The theoretical value is $\gamma_m = 0.102827$.

field for a short and a longer simulation with $\alpha_{x,y,z} = 0.85$. We can see that the predominant mode here has 6 wavelengths in the simulation domain, while 5 are expected from theory.

We conclude that to capture the physics properly one has to choose the parameters very carefully. The code can achieve very impressive results if the choice is correct.

5.3 Comparisons with PIC hybrid simulations

We chose the *CAM-CL* PIC hybrid algorithm we implemented to perform some comparisons. Temperature anisotropy instabilities are particular sensitive to the initial noise. While in the *HVH* code we add some perturbations in the magnetic field to be capable to observe any quantity evolution, here we need to carefully reduce

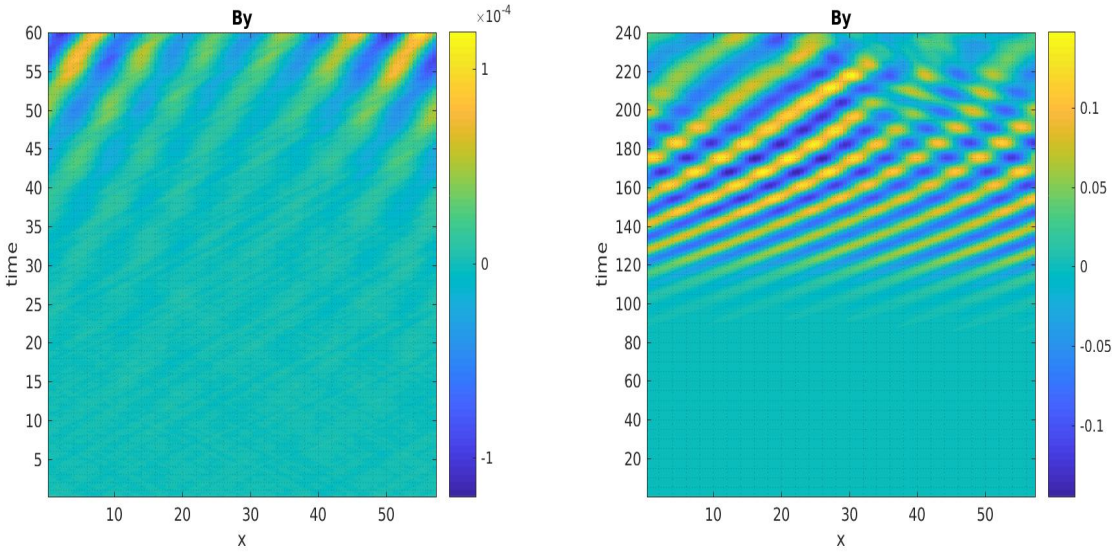

Figure 5.5: Left panel: magnetic field evolution - early stages; right panel: magnetic field evolution - longer simulation. Both simulations are run with $\alpha_{x,y,z} = 0.85$.

the initial particle noise to be able to reproduce the instability with precision. We performed a set of simulations with analogous initial condition as in the previous section, but now varying the number of particles per cell from 100 to 1000000 and calculated the linear growth rate and compared it with the theoretical value.

Ppc	γ	E_a	E_r
100	0.0044	0.0984	95.69%
1000	0.0026	0.1002	97.45%
10000	0.0052	0.0976	94.92%
100000	0.0126	0.0902	87.72%
500000	0.0815	0.0213	20.71%
1000000	0.0880	0.0148	14.39%

Table 5.2: Linear growth rate, relative and absolute errors varying the number of particles per cell. The theoretical value is $\gamma_m = 0.102827$.

In Tab. 5.2 we can see that the absolute error reaches the values that we obtained in the worst cases with the *HVH* code only when we go to a very large number of particles per cell and the simulations become cpu and memory expensive. This is very important mainly if we want to carry out multidimensional simulations. In fact it would clearly not be possible to use such large numbers of particles per cells on a 3D domain discretized in N_c^3, where N_c is the number of cells in a 1D simulation.

However, the *CAM-CL* code is capable to capture the instability. In Fig. 5.6 and

Fig. 5.7 we show the magnetic field and the logarithm of average square deviation of magnetic field amplitude for simulations with 10^3 particles per cells and 10^6 particles per cells. There are two things that we notice:

- the PIC is capable to capture perturbations travelling in both positive and negative directions conversely to the *HVH* which amplifies only perturbations travelling in the positive direction. We think that this is due to the difference in the initial condition: while in the PIC we have noise in the velocity distribution, in our code we input some artificial noise in the magnetic field. This difference implies also a difference in the balance of the initial modes.

- the values of initial noise are reflected in the initial value of the average magnetic field amplitude. Its interesting that in the *HVH* code the noise is several orders of magnitude smaller.

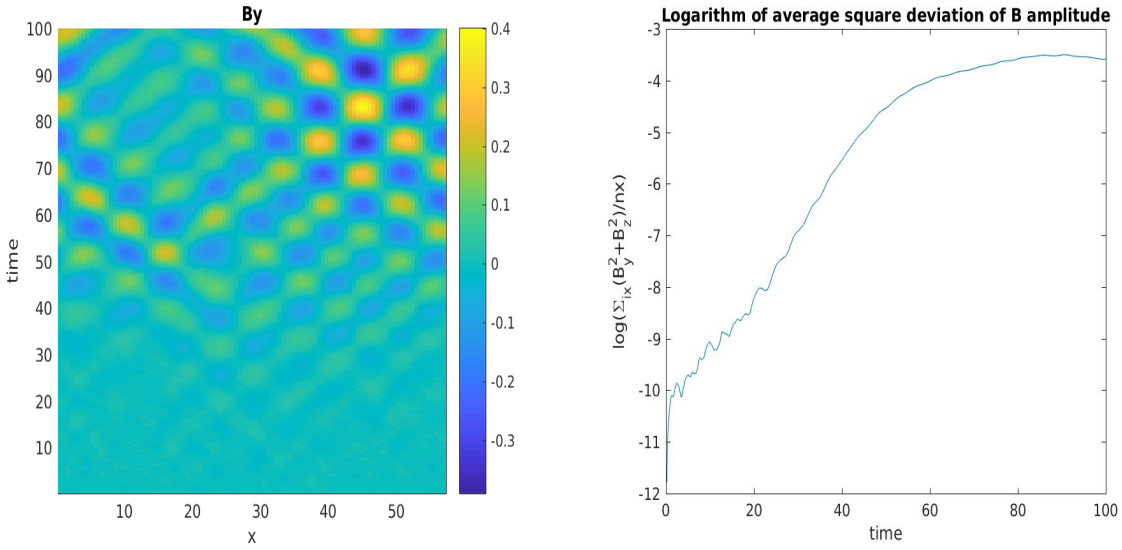

Figure 5.6: Left panel: magnetic field evolution; right panel: logarithm of average square deviation of magnetic field amplitude. The simulation is run with the *CAM-CL* code using 10^3 particles per cell.

We conclude that the code we present in this document has better performance in terms of dynamic range and error on the linear growth rate of the selected instability. To achieve the same results with a PIC hybrid code we need simulations which are more costly in terms of CPU and memory.

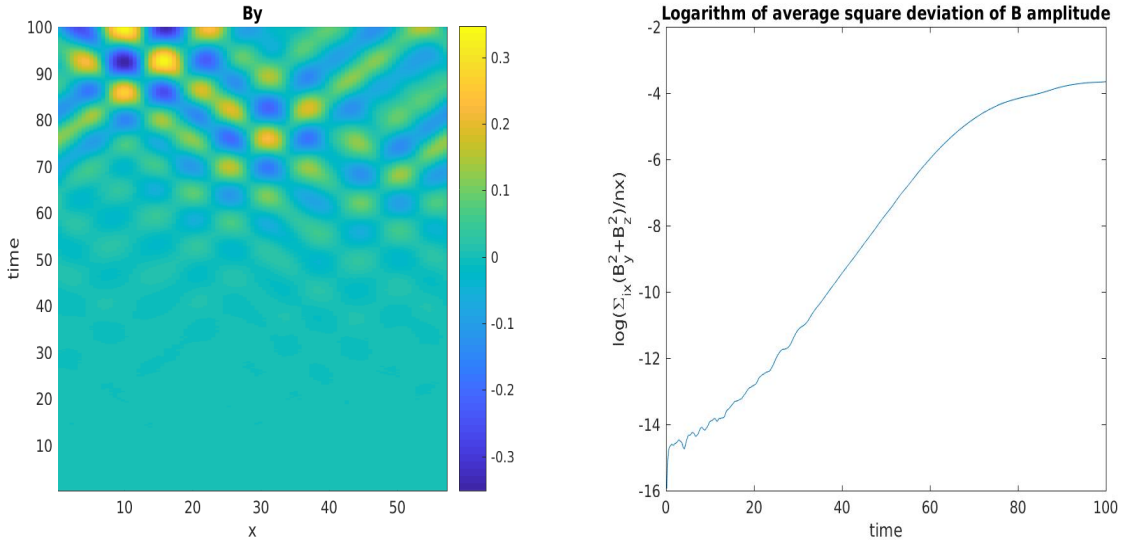

Figure 5.7: Left panel: magnetic field evolution; right panel: logarithm of average square deviation of magnetic field amplitude. The simulation is run with the *CAM-CL* code using 10^6 particles per cell.

6 Ion/ion beam instabilities

In this chapter we will consider another type of plasma instability, given by the presence of different components in the plasma. In fact, any time two plasma components stream through each other in direction parallel to the background magnetic field, an instability can arise [Gary, 1991]. This is due to the non-Maxwellian character of the sum of the distribution functions which can enhance plasma fluctuations and scattering between wave and particles.

Here we allow each component to have a Maxwellian distribution function with some drift velocity $\boldsymbol{v}_{0,s}$. We consider the drift velocity to be parallel or antiparallel to the background magnetic field $\boldsymbol{B}_0$. We will show that when the drift velocity between two components becomes greater than a certain threshold an instability can develop. These kind of instabilities are not clearly distinguishable as ion-driven low frequency and electron-driven high frequency. The different species interact between themselves and a relative drift between any component can cause an instability. However, since the code developed and described in this document can take into account only multiple ion species, we will simplify our study to ion/ion beam instabilities, i.e. the ones growing in the presence of two ion species generally named as core (the one more dense) and beam (the one less dense) and one electron species.

In the solar wind different ion populations streaming into each other were first observed in the 1970s [Feldman et al., 1973, 1974]. Their origin was not clear but they first hypothesized it to be associated with filling in of regions of density rarefaction caused by high velocity streams. In this less dense plasma regions the breakup and merging of thin high-velocity filaments would yield to double streaming in the solar wind. Bame et al. [1975] observed that in such events the core temperature anisotropy ratio changes significantly from being $\frac{T_\perp}{T_\parallel} < 1$ before the time of maximum velocity gradient to $\frac{T_\perp}{T_\parallel} > 1$ afterwards.

More recently Gary et al. [2015] used observations of events happened in 2005 to understand whether enhanced magnetic fluctuations in the solar wind are generated at the Sun and transported or are local phenomena arising in the interplanetary medium. He concluded that ion/ion instabilities are one of the local sources, to-

gether with ion temperature anisotropies, of these fluctuations measured by the Wind spacecraft.

The theory has been extensively studied since the first observations. Perkins [1976] investigated the propagation of waves quasi-perpendicular to the magnetic field. Threshold conditions for the parallel propagating instability growth have been shown by Gary [1991], Gary et al. [1984, 1985] and Gnavi et al. [1996] and we will report them later in this chapter. Verscharen and Chandran [2013] showed how the threshold conditions are reduced for oblique modes with $\boldsymbol{k} \times \boldsymbol{B} \neq 0$.

Hybrid simulations have been carried out in both mono and multi dimensional configurations. Gary et al. [1986] showed that the instability saturation is due to a reduction in the beam-core relative drift speed and an increase of the beam temperature anisotropy ratio. Winske and Omidi [1992], Winske and Quest [1986] carried out mono and bi-dimensional hybrid simulations showing that for propagation at $\theta \approx 0$ the instability is dominated by electromagnetic effects and large amplitude waves. 2D simulations reproduced an overall reduction of the magnetic field fluctuations. Daughton et al. [1999] used bi-dimensional hybrid simulations to show that the enhanced fluctuating fields arising in the instability cause a reduction in the core-beam relative drift velocity. More recently Muñoz et al. [2017] used a tri-dimensional hybrid code which takes into account the electron mass (see Chapter 3), *CHIEF*, to simulate this quasi-1D problem. The simulations used 1024 particles per cell for the core and 512 for the beam with large relative drift velocity ($v_0 = 10 v_A$), reproducing result in good agreement with linear theory.

This chapter is divided as follows: first we will have a look at the three ion/ion instabilities and their thresholds. Then we will show some results for simulations of two ion/ion right hand resonant instabilities with different growth rates and finally compare these with PIC hybrid simulations.

6.1 The instabilities

Here we focus on ion/ion instabilities with small beam density (weak beam) and relatively high drift velocity. We call $\boldsymbol{v}_0 = \boldsymbol{v}_{0,b} - \boldsymbol{v}_{0,c}$ the relative drift velocity between beam and core and we impose $\boldsymbol{v}_{0,s} \times \boldsymbol{B} = 0$. Three electromagnetic instabilities can grow from this configuration [Gary et al., 1984]:

- the ion/ion right-hand resonant instability;
- the ion/ion left-hand resonant instability;

- the ion/ion nonresonant instability.

To describe these instabilities it is important to define three different regimes:

- cool beam: if $0 < v_b \ll v_{0,b}$, where v_b is the beam's thermal velocity;
- warm beam: if $v_{0,b} \sim v_b$;
- hot beam: if $v_{0,b} \ll v_b$.

6.1.1 The ion/ion right-hand resonant instability

For a cool isotropic beam the instability with lower threshold (i.e., the one more likely to develop) is the ion/ion right-hand resonant instability. The instability is resonant, which means the phase velocity lies in the region of velocity space at high ion's concentration, therefore allowing the energy transfer between particles and waves. Starting from $v_0 = 0$, where there is no distinction between beam and core the mode is associated with the right hand circularly polarized magnetosonic/whistler wave with positive helicity. In the long wavelength limit it satisfies:

$$\omega_r = kv_A, \tag{6.1}$$

while it makes a transition to whistler dispersion for smaller wavelengths. The instability which evolves from this mode is dispersive for long wavelengths, and near wave numbers of maximum growth rate it satisfies:

$$\omega_r = k_z v_{0,b} - \Omega_{ci} \tag{6.2}$$

The instability is beam resonant. Since $\omega_r > 0$ $k_z > 0$ and $v_{0,b} > 0$ it propagates in the direction of the beam. For instabilities with beam densities such that $0.01 \leq n_b/n_e \leq 0.10$, $\omega_r \simeq \gamma$ so:

$$\frac{\gamma_m}{\Omega_{ci}} \simeq (\frac{n_b}{2n_e})^{1/3} \tag{6.3}$$

6.1.2 The ion/ion left-hand resonant instability

In the presence of a hot beam another type of ion/ion instability can arise. This instability evolves out of the ion/cyclotron wave with $\omega_r > 0$. It has a modest growth rate so the ω_r stays positive increasing $\boldsymbol{v}_0$. This implies that the developing mode is left hand circularly polarized and propagates in the same direction of the

beam. The latter is resonant, while electrons and core are nonresonant [Goldstein et al., 1983]

The faster growing mode arises for $\boldsymbol{k} \times \boldsymbol{B}_0 = 0$ [Gary et al., 1984, Smith et al., 1985], but it has been shown that for oblique propagation there are local maxima in the growth rate.

6.1.3 The ion/ion nonresonant instability

In the presence of a cool fast ion beam a firehose like instability may arise with all the three components nonresonant. This instability has a direction of propagation which is antiparallel to the beam, negative helicity and small phase speed. The latter implies that it is not meaningful to use the polarization to identify this mode. In fact a small change in the frame of reference can invert the polarization. For large drift velocity and small beam densities [Winske and Leroy, 1984] give a formulation for the maximum growth rate:

$$\frac{\gamma_m}{\Omega_{ci}} \simeq \frac{n_b}{2n_e}\frac{v_0}{v_A}, \tag{6.4}$$

where v_A is the Alfvén velocity. From this expression we can see that the ion/ion nonresonant instability can have maximum growth rate larger than other instabilities.

6.1.4 Instability thresholds

We show here the thresholds for the development of the right hand resonant and non-resonant instabilities. In Fig. 6.1 the solid line represents the minimum value for v_0, varying the beam to ion density ratio, for the right hand resonant instability to develop. Under this line the configuration is considered stable. The dashed line is the threshold for the right hand non-resonant. Between these two lines only the former can arise, while above the dashed line they can both develop. The dotted line represents the value of the relative drift velocity for which the two instabilities have the same growth rate.

We can observe that the threshold for the resonant instability satisfies $v_A < v_0 < 2v_A$, while for the non-resonant v_0 needs to be much larger, particularly when n_b becomes small. The β of the core does not influence the limiting value, especially at $0.2 < \beta_c < 5.0$ [Gary et al., 1985], which are the values of interest for our simulations.

Figure 6.2 shows the dependency of the thresholds on the beam to core ("main" in the figure) temperature ratio. For both right hand resonant and nonresonant

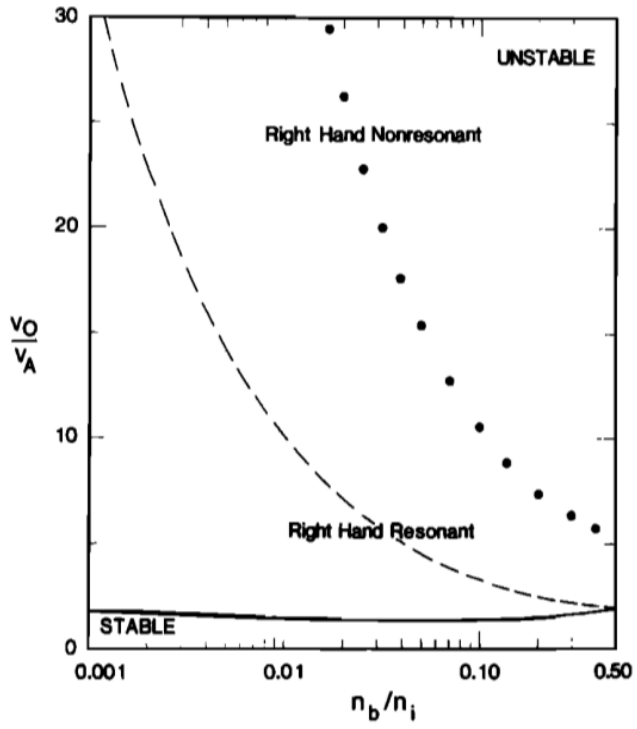

Figure 6.1: Thresholds for the ion/ion right hand resonant (solid line) and non-resonant (dashed line) instability. The graph gives the minimum value of the beam-core relative velocity drift as function of the ratio between beam density and total ion density, for which the instability grows. The minimum linear growth rate considered for the intability to grow is $\gamma_m = 10^{-4}$. The dotted line represents the line of equal maximum growth rate between the two instabilities. Source: Gary et al. [1986].

three values of $\frac{T_b}{T_m}$ are considered (1, 10 and 100). While for the nonresonant case the threshold lines are very close to each other, therefore largely dependent of this parameter, for the resonant case there is a noticeable reduction of the threshold with increasing beam temperature.

6.2 Ion/ion cool beam instabilities study

To further test our Hermite Vlasov-Hybrid code we simulated a set of ion/ion instabilities in which the beam is assumed to be cool i.e. $0 < v_b \ll v_{0,b}$. We fixed the beam density $n_b/n_e = 0.1$ and we chose 2 different values for $v_{0,b}$.

We used the linear solver [Camporeale and Burgess, 2017] to find the wave vector k_m of the fastest growing mode and the corresponding maximum growth rate γ_m. From the linear solver we could notice, as expected, that only the ion/ion right hand

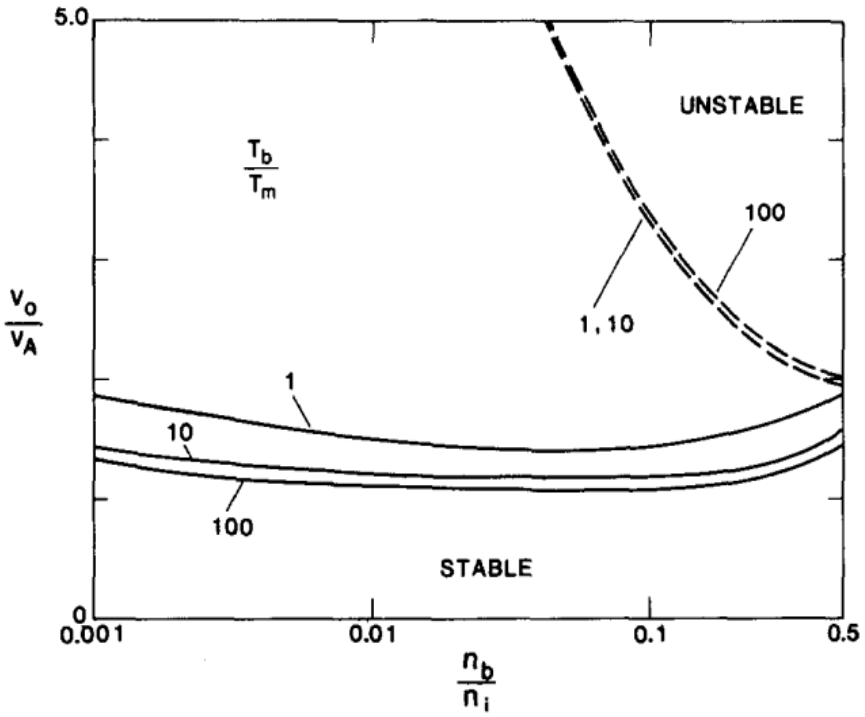

Figure 6.2: Thresholds for the ion/ion right hand resonant (solid line) and non-resonant (dashed line) instability for different value of beam to core ("main" in the figure) temperature ratio. Source: Gary et al. [1985].

resonant mode was present. From the wave vector we found the wavelength of the faster growing mode and we multiplied it for an integer number to obtain the size of the domain to select the desired mode.

For all the simulations we set $\beta_b = \beta_c = \beta_e = 1$ with isotropic Maxwellian distribution functions for core and beam. The thermal velocities in perpendicular and parallel direction are for both ion components $V_{th,\perp} = V_{th,\parallel} = 0.70710678$ and we set the parameters of the Hermite expansion $\alpha_{x,y,z} = 0.75$. We use 10 Hermite function in each velocity direction, a time step of $\Delta t = 0.02\Omega_{ci}^{-1}$ and cell sizes varying around $\Delta x = 0.5 d_i$ to correctly discretize the domain which has as size a multiple of the wavelength.

We report separately the results for the different simulations.

6.2.1 Low growth rate ion/ion right hand resonant instability

We set $v_{0,b} = 2$, and with the linear solver we found a value of $k_m = 0.6028$, which implies $\lambda_m = 10.423$, where λ_m is the wavelength of the fastest growing mode and we

therefore set the domain size to be $5\lambda_m$ and find the cell size $\Delta x = 0.521167$ dividing the domain in 100 cells. We let the simulation run for 6000 time steps and computed the linear growth rate and compared it with the result from the linear solver. The value found is $\gamma_{m,sim} = 0.0690$ against a theoretical value of $\gamma_{m,th} = 0.0666$, with a relative error of 3.6%.

In Fig. 6.3 we can see the evolution of B_y (left panel) and we can see that the mode which grows has exactly 5 wavelengths in our domain. In the right panel we can observe the logarithm of the average square deviation of the magnetic field amplitude. We can appreciate that the level of initial noise is very low and we can see the linear phase starting at $t \simeq 80\Omega_{ci}^{-1}$.

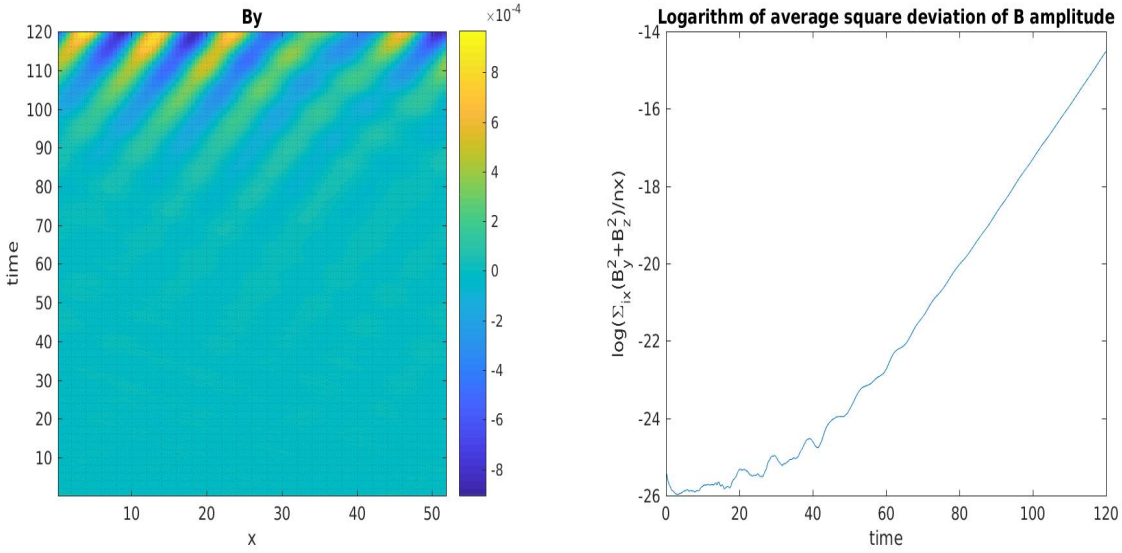

Figure 6.3: Ion/ion instability with $v_{0,b} = 2$. Left panel: time evolution of magnetic field in y direction; right panel: logarithm of average square deviation of magnetic field amplitude . The simulation is run for 6000 time steps i.e. 120 Ω_{ci}^{-1}.

6.2.2 Medium-High growth rate ion/ion right hand resonant instability

Here we set $v_{0,b} = 3$, a value which lies between the ion/ion right hand resonant and the ion/ion nonresonant thresholds. With the linear solver we found a value of $k_m = 0.4711$, which means $\lambda_m = 13.337$ and we set the domain size to be $4\lambda_m$ and find the cell size $\Delta x = 0.53349$ dividing the domain in 100 cells. We let the simulation run for 4000 time steps and compute the linear growth rate and compare

it with the result from the linear solver. The value found is $\gamma_{m,sim} = 0.1983$ against a theoretical value of $\gamma_{m,th} = 0.2240$, with a relative error of 11.5%.

In Fig 6.4 we can see the evolution of B_y (left panel) and we can see that the mode which grows has exactly 4 wavelengths in our domain. In the right panel we can observe the logarithm of the average square deviation of the magnetic field amplitude. In this case we can see that the value gets very close to 0, but the saturation does not happen. We believe that this is due to the changes in the distribution function which happen while the instability develops. In fact beam and core exchange energy and the distribution functions suffer important modifications. When these changes are too large the Hermite polynomial expansion is no longer able to approximate the distribution function and the instability does not stop growing. To improve this we suggest as future work the implementation of adaptivity in the parameters of the Hermite expansion.

We remark that in recent Vlasov-Hybrid simulation with physical discretisation of the velocity space, the number of grid points for each velocity direction is between 51 and 61 and they still lack of accuracy.

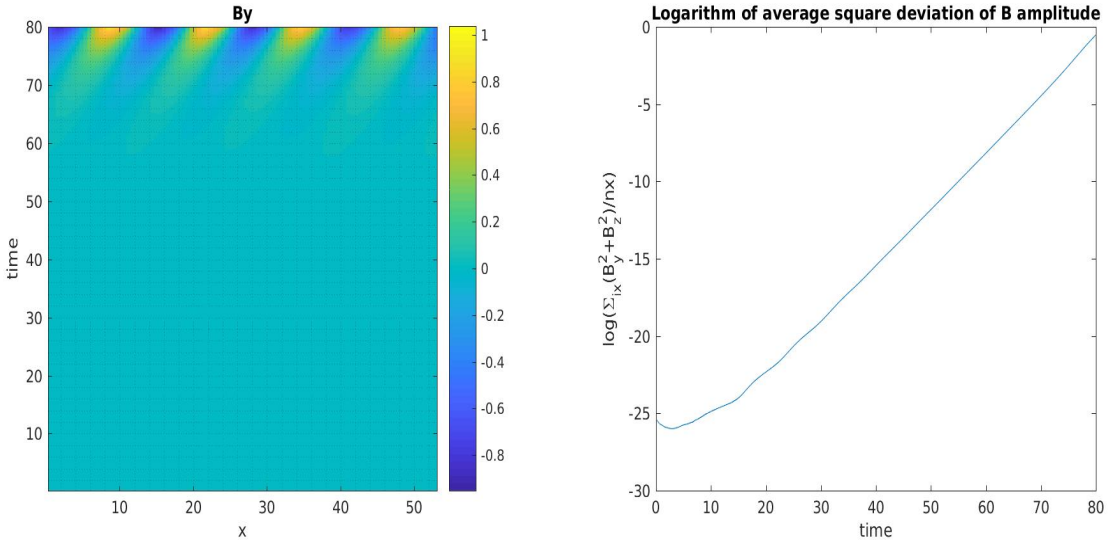

Figure 6.4: Ion/ion instability with $v_{0,b} = 3$. Left panel: time evolution of magnetic field in y direction; right panel: logarithm of average square deviation of magnetic field amplitude . The simulation is run for 4000 time steps i.e. 80 Ω_{ci}^{-1}.

6.3 Comparisons with PIC hybrid simulations

We have simulated the same two instabilities using the *CAM-CL* algorithm. We report here results from simulations which make use of 10^5 particles per cell. However, we remark that it is possible to use this large number of particles per cell only for mono-dimensional simulations.

From Fig. 6.5 and Fig. 6.6 we can observe that in this case the PIC hybrid code is not capable of capturing the right mode properly. In fact we have the growth of a superposition of different modes even before saturation. We computed the growth rate and we found that for the case with $v_{0,b} = 2$ the relative error to the value expected from linear theory is 19.5%, which is much larger than what we obtained with the *HVH* code (3.6%). However, when the growth rate of the simulated instability increases, in the case $v_{0,b} = 3$, we found a value closer to the one expected from theory, with a relative error of 5.2%. Moreover, the particle in cell hybrid algorithm is capable of simulating the saturation phase of the instability which is not properly reproduced by the *HVH*.

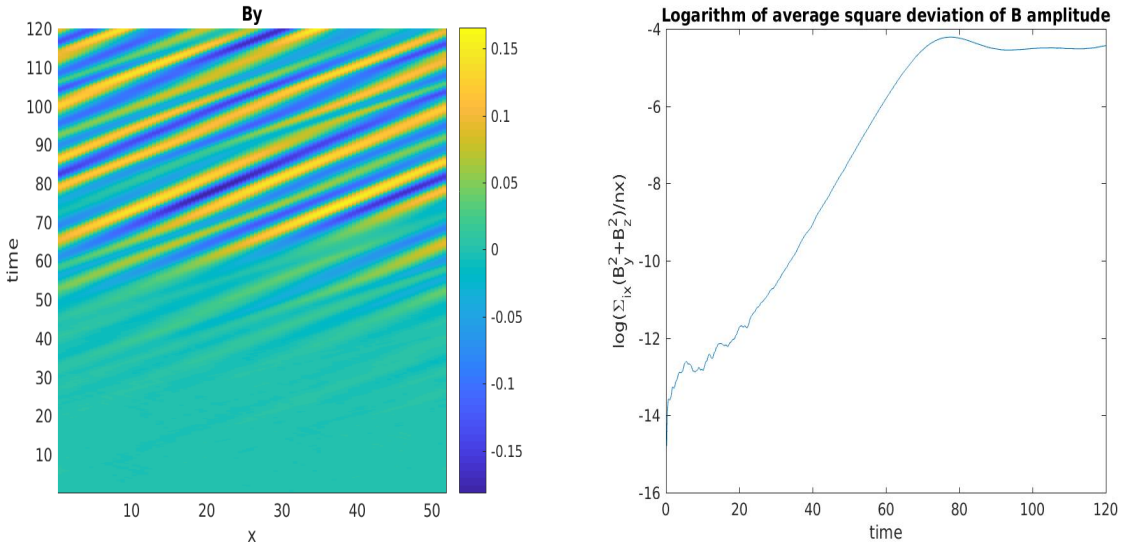

Figure 6.5: Ion/ion instability with $v_{0,b} = 2$. Left panel: time evolution of magnetic field in y direction; right panel: logarithm of average square deviation of magnetic field amplitude . The simulation is run with the *CAM-CL* algorithm for 6000 time steps i.e. 120 Ω_{ci}^{-1}.

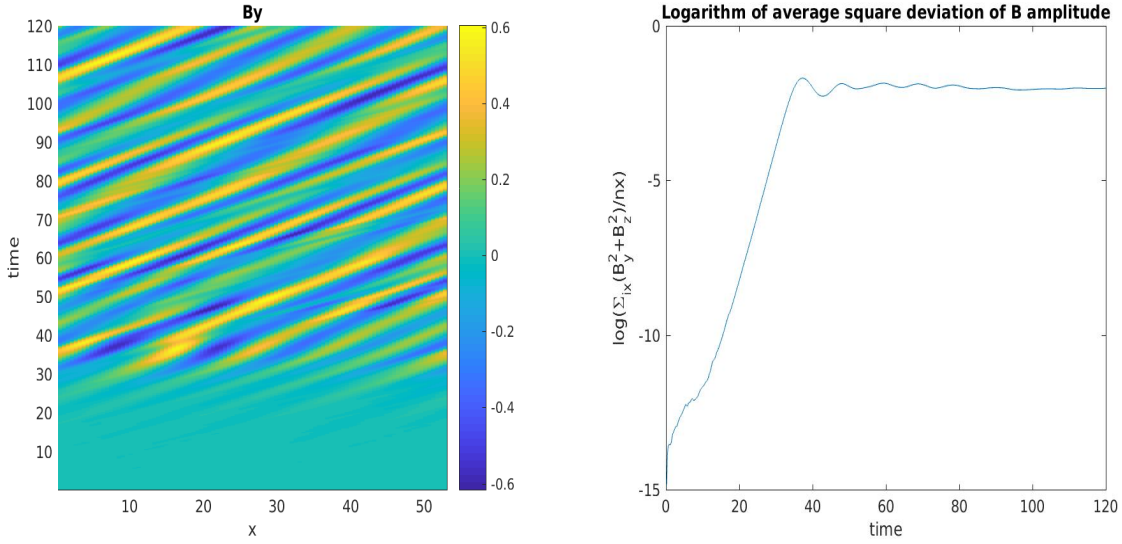

Figure 6.6: Ion/ion instability with $v_{0,b} = 3$. Left panel: time evolution of magnetic field in y direction; right panel: logarithm of average square deviation of magnetic field amplitude . The simulation is run with the *CAM-CL* algorithm for 6000 time steps i.e. 120 Ω_{ci}^{-1}.

7 Bi-dimensional implementation

The Hermite-Vlasov-Hybrid code has been extended to the 2D case making use of the structure of the 1D code and using the `PETSc` external library for the parallelization.

Here we first describe the algorithm for the bi-dimensional Hermite-Vlasov-Hybrid code, pointing out the few differences from the mono dimensional code, then we show the implementation with some details about the domain decomposition, parallelization and how the input file changes. Some preliminary results are also presented.

The work described in this chapter has been entirely done as support of this Ph.D. thesis by the candidate.

7.1 The 2D model

The algorithm adopted is the same as for the mono-dimensional case, but now the equations are solved on a rectangular grid in the $x - y$ plane. We describe the algorithm here for clarity and then we discuss just the equations which have changed.

The method combines the solution of the Vlasov equation through expansion of the distribution function as a sum of Hermite functions, together with the Current Advance Method presented in Valentini et al. [2007]. The Vlasov equation resolves the protons which hence are treated kinetically, while electrons are treated as a massless fluid described only by their momentum equation. The plasma components are coupled via Maxwell's equations in which the quasi-neutrality and Darwin approximations hold.

We solve a set of three equations:

- Vlasov equation for the distribution function:

$$\frac{\partial f_s}{\partial t} + \boldsymbol{v}_s \cdot \nabla f_s + \frac{q_s}{m_s}(\boldsymbol{E} + \boldsymbol{v}_s \times \boldsymbol{B}) \cdot \frac{\partial f_s}{\partial \boldsymbol{v}} = 0 \tag{7.1}$$

- momentum equation for electrons [Matthews, 1994]:

$$\boldsymbol{E} = -\boldsymbol{v}_i \times \boldsymbol{B} + \frac{1}{\mu_0\, e n_e}\boldsymbol{j} \times \boldsymbol{B} - \frac{\nabla p_e}{e n_e} + \eta \boldsymbol{j} \tag{7.2}$$

- Maxwell equations for the magnetic field, with the chosen assumptions:

$$\frac{\partial \boldsymbol{B}}{\partial t} = -\nabla \times \boldsymbol{E}, \tag{7.3}$$

$$\nabla \times \boldsymbol{B} = \mu_0 \boldsymbol{j} \tag{7.4}$$

Again f_s is the distribution function for species s; $\boldsymbol{v}_s$ is the bulk velocity of species s (particle charge q_s and mass m_s); $\boldsymbol{v}_i$ is the bulk ion velocity; $\boldsymbol{E}$ is the electric field; $\boldsymbol{B}$ is the magnetic field; n_i (n_e) is the ion (electron) density, and quasi-neutrality is assumed so $n = n_i = n_e$; p_e is the scalar electron pressure; η is the resistivity; $\boldsymbol{j}$ is the total current, where $\boldsymbol{j} = \sum_s \boldsymbol{j}_s$.

As we can see we have the same equations in vectorial form as for the mono-dimensional case. However, while in the 1D case the quantities were allowed to vary only in one physical direction, here they can vary along x and y directions, so we retain both x and y derivatives and neglect derivatives with respect to z.

7.1.1 Hermite decomposition

The Hermite decomposition acts on velocity space only, therefore it remains unchanged from the mono-dimensional case. We remind the reader to Section 4.1.1 for details. We report here the final equation for the coefficients of the distribution function, where we have neglected the derivatives along the z direction:

$$
\begin{aligned}
&\frac{\partial C_{l,m,n}}{\partial t}+ \\
&\alpha\left(\sqrt{\frac{l+1}{2}}\frac{\partial C_{l+1,m,n}}{\partial x}+\sqrt{\frac{l}{2}}\frac{\partial C_{l-1,m,n}}{\partial x}+\frac{u}{\alpha}\frac{\partial C_{l,m,n}}{\partial x}\right)+ \\
&\beta\left(\sqrt{\frac{m+1}{2}}\frac{\partial C_{l,m+1,n}}{\partial y}+\sqrt{\frac{m}{2}}\frac{\partial C_{l,m-1,n}}{\partial y}+\frac{v}{\beta}\frac{\partial C_{l,m,n}}{\partial y}\right)+ \\
&-\frac{\Omega}{\omega}\left[\frac{\sqrt{2l}}{\alpha}E_x C_{l-1,m,n}-\frac{\sqrt{2m}}{\beta}E_y C_{l,m-1,n}-\frac{\sqrt{2n}}{\gamma}E_z C_{l,m,n-1}\right]+ \\
&\frac{\Omega}{\omega}B_x\left[C_{l,m-1,n-1}\sqrt{mn}\left(\frac{\beta}{\gamma}-\frac{\gamma}{\beta}\right)+\right. \\
&C_{l,m+1,n-1}\left(\frac{\beta}{\gamma}\sqrt{n(m+1)}\right)+C_{l,m,n-1}\left(\frac{v}{\gamma}\sqrt{2n}\right)+ \\
&\left.-C_{l,m-1,n+1}\left(\frac{\gamma}{\beta}\sqrt{m(n+1)}\right)-C_{l,m-1,n}\left(\frac{w}{\beta}\sqrt{2m}\right)\right]+ \\
&\frac{\Omega}{\omega}B_y\left[C_{l-1,m,n-1}\sqrt{nl}\left(\frac{\gamma}{\alpha}-\frac{\alpha}{\gamma}\right)+\right. \\
&C_{l-1,m,n+1}\left(\frac{\gamma}{\alpha}\sqrt{l(n+1)}\right)+C_{l-1,m,n}\left(\frac{w}{\alpha}\sqrt{2l}\right)+ \\
&\left.-C_{l+1,m,n-1}\left(\frac{\alpha}{\gamma}\sqrt{n(l+1)}\right)-C_{l,m,n-1}\left(\frac{u}{\gamma}\sqrt{2n}\right)\right]+ \\
&\frac{\Omega_s}{\omega}B_z\left[C_{l-1,m-1,n}\sqrt{mn}\left(\frac{\alpha}{\beta}-\frac{\beta}{\alpha}\right)+\right. \\
&C_{l+1,m-1,n}\left(\frac{\alpha}{\beta}\sqrt{m(l+1)}\right)+C_{l,m-1,n}\left(\frac{u}{\beta}\sqrt{2m}\right)+ \\
&\left.-C_{l-1,m+1,n}\left(\frac{\beta}{\alpha}\sqrt{l(m+1)}\right)-C_{l-1,m,n}\left(\frac{v}{\alpha}\sqrt{2l}\right)\right]=0
\end{aligned}
\tag{7.5}
$$

7.1.2 Fluid moments

The computation of the fluid moments of the distribution function involves integrals over the velocity space which is unchanged from the monodimensional case. Therefore we compute densities and velocities in the same way:

$$
n(\mathbf{x},t)=\alpha\beta\gamma C_{0,0,0} \tag{7.6}
$$

$$V_x(\mathbf{x},t) = \alpha\beta\gamma\left(\alpha\sqrt{\frac{1}{2}}C_{1,0,0} + uC_{0,0,0}\right) \tag{7.7}$$

$$V_y(\mathbf{x},t) = \alpha\beta\gamma\left(\beta\sqrt{\frac{1}{2}}C_{0,1,0} + vC_{0,0,0}\right) \tag{7.8}$$

$$V_z(\mathbf{x},t) = \alpha\beta\gamma\left(\gamma\sqrt{\frac{1}{2}}C_{0,0,1} + wC_{0,0,0}\right) \tag{7.9}$$

7.1.3 Time advancement scheme

The time advancement scheme works similarly to the mono-dimensional case. We report it here again for completeness, underlining the differences in the operators when present.

The Hermite decomposition for the Vlasov equation is nested in a Current Advance Method where the former is solved through a splitting of the Vlasov equation [Cheng and Knorr, 1976, Valentini et al., 2007] into two different ones which are solved separately:

$$\frac{\partial f}{\partial t} + \boldsymbol{v}\cdot\nabla f = 0 \tag{7.10}$$

$$\frac{\partial f}{\partial t} + (\boldsymbol{E} + \boldsymbol{v}\times\boldsymbol{B})\cdot\frac{\partial f}{\partial \boldsymbol{v}} = 0 \tag{7.11}$$

In the first equation the velocity is considered as parameter, while in the second the position and the fields are considered as parameters. A second order accurate solution is provided by a splitting scheme in the form:

$$f(\boldsymbol{x},\boldsymbol{v},t = N\Delta t) = \left[\Lambda_{xy}(\frac{\Delta t}{2})\Lambda_v(\Delta t)\Lambda_{xy}(\frac{\Delta t}{2})\right]^N f_0(\boldsymbol{x},\boldsymbol{v}), \tag{7.12}$$

where $\Lambda_{xy}(t)f(\boldsymbol{x},\boldsymbol{v},t)$ and $\Lambda_v(t)f(\boldsymbol{x},\boldsymbol{v},t)$ are the solutions at time t of the two previous equations, and $f_0(\boldsymbol{x},\boldsymbol{v})$ is the initial condition for the distribution function at time $t = 0$

7.1.4 Λ_{xy} operator and mesh drifting instability

In our time scheme advancement the distribution is advanced separately with a spatial operator Λ_x and a velocity operator Λ_v. These advancements are leapfrogged in time: to spatially advance the coefficients of the distribution function of a time step the coefficient advanced with the velocity operator to next half time step are used and vice versa. When the equations to be solved are non-linear this can lead to

a numerical instability called the mesh drifting instability. The latter can arise due to the decoupling between adjacent mesh points in the grid as shown in Fig. 7.1.

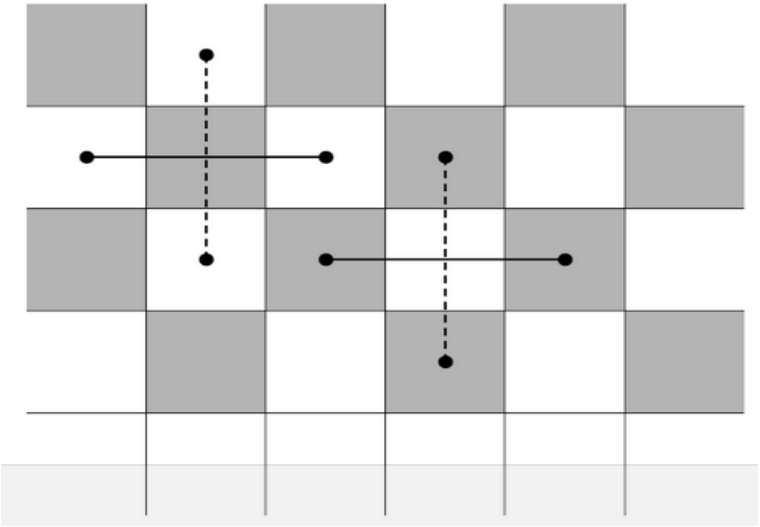

Figure 7.1: Decoupling in leapfrogged scheme. The cells on black colour are coupled with themselves and the cells in white colours are coupled with themselves also. Source: Press et al. [1992]

To overcome this instability we implemented four different explicit methods:

- two versions of the Lax-Wendroff scheme;
- a 4^{th} order Runge-Kutta scheme;
- a Lax-Friedrichs scheme.

Here we will give more details about the Lax-Wendroff schemes, while the Runge-Kutta and the Lax-Friedrichs follow standard implementations.

Lax-Wendroff version 1

In the bi-dimensional case the Λ_x operator now includes derivatives in x and y direction. In particular the operator involves the solution of the following PDE:

$$\frac{\partial C_{l,m,n}}{\partial t} + \alpha \left(\sqrt{\frac{l+1}{2}} \frac{\partial C_{l+1,m,n}}{\partial x} + \sqrt{\frac{l}{2}} \frac{\partial C_{l-1,m,n}}{\partial x} + \frac{u}{\alpha} \frac{\partial C_{l,m,n}}{\partial x} \right) + \beta \left(\sqrt{\frac{m+1}{2}} \frac{\partial C_{l,m+1,n}}{\partial y} + \sqrt{\frac{m}{2}} \frac{\partial C_{l,m-1,n}}{\partial y} + \frac{v}{\beta} \frac{\partial C_{l,m,n}}{\partial y} \right) = 0. \quad (7.13)$$

We attempted to solve this equation using a Lax-Wendroff single-step 2D split method. If we split the Λ_x operator in two parts:

$$\frac{\partial C_{l,m,n}}{\partial t} + \alpha \left(\sqrt{\frac{l+1}{2}} \frac{\partial C_{l+1,m,n}}{\partial x} + \sqrt{\frac{l}{2}} \frac{\partial C_{l-1,m,n}}{\partial x} + \frac{u}{\alpha} \frac{\partial C_{l,m,n}}{\partial x} \right) = 0, \tag{7.14}$$

$$\frac{\partial C_{l,m,n}}{\partial t} + \beta \left(\sqrt{\frac{m+1}{2}} \frac{\partial C_{l,m+1,n}}{\partial y} + \sqrt{\frac{m}{2}} \frac{\partial C_{l,m-1,n}}{\partial y} + \frac{v}{\beta} \frac{\partial C_{l,m,n}}{\partial y} \right) = 0, \tag{7.15}$$

we can solve the first equation over a time step to find an intermediate solution. Then we put the intermediate solution in the second equation and we solve it over another time step to find the final solution after one full time step. This is possible because this equation involves only the advection operator which is linear, so we can apply superposition principle: we can advect along $(v_x, 0, 0)$ for a full time step and then advect along $(0, v_y, 0)$ for the same time step to obtain the same result that we would have advecting for a full time step along $(v_x, v_y, 0)$.

Let us consider the classic 1D advection equation:

$$\frac{\partial u}{\partial t} = -A \frac{\partial u}{\partial x}. \tag{7.16}$$

If we take a second order Taylor-series expansion of the solution at time $t + \Delta t$ we have:

$$u(x, t + \Delta t) = u(x, t) + \Delta t \frac{\partial u}{\partial t} + \frac{1}{2} (\Delta t)^2 \frac{\partial^2 u}{\partial t^2} \tag{7.17}$$

Taking the temporal derivative of the former:

$$\frac{\partial^2 u}{\partial t^2} = -A \frac{\partial}{\partial t} \frac{\partial u}{\partial x} = A^2 \frac{\partial^2 u}{\partial x^2}, \tag{7.18}$$

and substituting into the Taylor expansion we have:

$$u(x, t + \Delta t) = u(x, t) - \Delta t A \frac{\partial u}{\partial x} + \frac{1}{2} (\Delta t)^2 A^2 \frac{\partial^2 u}{\partial x^2}. \tag{7.19}$$

Getting back to the equation for the distribution function, after splitting it we can write:

$$\frac{\partial f(\boldsymbol{x}, \boldsymbol{v}, t)}{\partial t} = -v_x \frac{\partial f(\boldsymbol{x}, \boldsymbol{v}, t)}{\partial x} \tag{7.20}$$

$$\frac{\partial f(\boldsymbol{x}, \boldsymbol{v}, t)}{\partial t} = -v_y \frac{\partial f(\boldsymbol{x}, \boldsymbol{v}, t)}{\partial y}. \tag{7.21}$$

We substitute here the Taylor expansion in each direction. The terms containing the second derivative contains terms $v_x^2 \frac{\partial^2 f(\boldsymbol{x},\boldsymbol{v},t)}{\partial x^2}$ and $v_y^2 \frac{\partial^2 f(\boldsymbol{x},\boldsymbol{v},t)}{\partial y^2}$. Starting from Eq. (4.12) it is easy to show that:

$$v_x^2 \Psi_n(\xi_x) = v_x \left(\alpha \sqrt{\frac{n+1}{2}} \Psi_{n+1} + \alpha \sqrt{\frac{n}{2}} \Psi_{n-1} + u \Psi_n \right) = \alpha^2 \sqrt{\frac{n+1}{2}}$$
$$\left(\sqrt{\frac{n+2}{2}} \Psi_{n+2} + \sqrt{\frac{n+1}{2}} \Psi_n + \frac{u}{\alpha} \Psi_{n+1} \right) + \alpha^2 \sqrt{\frac{n}{2}} \left(\sqrt{\frac{n}{2}} \Psi_n + \sqrt{\frac{n-1}{2}} \Psi_{n-2} + \frac{u}{\alpha} \Psi_{n-1} \right) +$$
$$+ u\alpha \sqrt{\frac{n+1}{2}} \Psi_{n+1} + u\alpha \sqrt{\frac{n}{2}} \Psi_{n-1} + u^2 \Psi_n, \quad (7.22)$$

and a similar term can be obtained for the y equation. Projecting the equations containing the Taylor expansion into p, q, r Hermite functions and approximating the spatial derivatives with a second order central difference scheme we obtain the final formulation for the spatial operator:

$$C^*_{i,j,l,m,n} = C^t_{i,j,l,m,n} - \frac{\Delta t}{2\Delta x} \alpha [\sqrt{\frac{l+1}{2}} (C^t_{i+1,j,l+1,m,n} - C^t_{i-1,j,l+1,m,n}) +$$
$$+ \sqrt{\frac{l}{2}} (C^t_{i+1,j,l-1,m,n} - C^t_{i+1,j,l-1,m,n}) + \frac{u}{\alpha} (C^t_{i+1,j,l,m,n} - C^t_{i-1,j,l,m,n})] +$$
$$+ \frac{(\Delta t)^2}{2(\Delta x)^2} [\alpha^2 \sqrt{\frac{l+1}{2}} \sqrt{\frac{l+2}{2}} (C^t_{i+1,j,l+2,m,n} - 2C^t_{i,j,l+2,m,n} + C^t_{i-1,j,l+2,m,n}) +$$
$$+ 2\alpha u \sqrt{\frac{l+1}{2}} (C^t_{i+1,j,l+1,m,n} - 2C^t_{i,j,l+1,m,n} + C^t_{i-1,j,l+1,m,n}) + (\alpha^2 \frac{l+1}{2} + \alpha^2 \frac{l}{2} + u^2)$$
$$(C^t_{i+1,j,l,m,n} - 2C^t_{i,j,l,m,n} + C^t_{i-1,j,l,m,n}) + 2\alpha u \sqrt{\frac{l}{2}} (C^t_{i+1,j,l-1,m,n} - 2C^t_{i,j,l-1,m,n} + C^t_{i-1,j,l-1,m,n}) +$$
$$+ \alpha^2 \sqrt{\frac{l}{2}} \sqrt{\frac{l-1}{2}} (C^t_{i+1,j,l-2,m,n} - 2C^t_{i,j,l-2,m,n} + C^t_{i-1,j,l-2,m,n})], \quad (7.23)$$

$$C^{t+\Delta t}_{i,j,l,m,n} = C^{*}_{i,j,l,m,n} - \frac{\Delta t}{2\Delta y}\beta[\sqrt{\frac{m+1}{2}}(C^{*}_{i,j+1,l,m+1,n} - C^{*}_{i,j-1,l,m+1,n}) +$$
$$+ \sqrt{\frac{m}{2}}(C^{*}_{i,j+1,l,m-1,n} - C^{*}_{i,j-1,l,m-1,n}) + \frac{v}{\beta}(C^{*}_{i,j+1,l,m,n} - C^{*}_{i,j-1,l,m,n})] +$$
$$+ \frac{(\Delta t)^2}{2(\Delta y)^2}[\beta^2\sqrt{\frac{m+1}{2}}\sqrt{\frac{m+2}{2}}(C^{*}_{i,j+1,l,m+2,n} - 2C^{*}_{i,j,l,m+2,n} + C^{*}_{i,j-1,l,m+2,n}) +$$
$$+ 2\beta v\sqrt{\frac{m+1}{2}}(C^{*}_{i,j+1,l,m+1,n} - 2C^{*}_{i,j,l,m+1,n} + C^{*}_{i-1,j,l,m+1,n}) + (\beta^2\frac{m+1}{2} + \beta^2\frac{m}{2} + v^2)$$
$$(C^{*}_{i,j+1,l,m,n} - 2C^{*}_{i,j,l,m,n} + C^{*}_{i,j-1,l,m,n}) + 2\beta v\sqrt{\frac{m}{2}}(C^{*}_{i,j+1,l,m-1,n} - 2C^{*}_{i,j,l,m-1,n} + C^{*}_{i,j-1,l,m-1,n}) +$$
$$+ \beta^2\sqrt{\frac{m}{2}}\sqrt{\frac{m-1}{2}}(C^{*}_{i,j+1,l,m-2,n} - 2C^{*}_{i,j,l,m-2,n} + C^{*}_{i,j-1,l,m-2,n})]. \quad (7.24)$$

Unfortunately, this scheme was not able to stop the mesh drifting instability development. We observed the growth of instability even with a simple quiet Maxwellian initial condition.

Lax-Wendroff version 2

The second version of the Lax-Wendroff that we implemented follows the 1D implementation that we used of our 1D3V code [Press et al., 1992]. We first applied the splitting of the x and y directions then the 1D Lax-Wendroff scheme for each direction.

This scheme also was not able to stop the mesh drifting instability developing.

4^{th} order Runge-Kutta

We implemented a standard 4^{th} order Runge-Kutta method described in Press et al. [1992]. We will not report the details. Again, the method was not able to stop the mesh drifting instability developing.

Lax-Friedrichs

The simple Lax-Friedrichs scheme allowed us to overcome the mesh drifting instability. This has been implemented using the normal 2D equation where the starting point to update $C_{i,j,l,m,n}$ is $0.25(C_{i,j+1,l,m,n} + C_{i,j-1,l,m,n} + C_{i+1,j,l,m,n} + C_{i-1,j,l,m,n})$ instead of $C_{i,j,l,m,n}$ itself. However, this method introduced numerical dissipation and we observed the damping of each oscillation that we imposed in the system.

The Λ_v operator, seen in Eq. (7.11), does not involve spatial derivatives. For this reason it is solved implicitly using the same matrix of the 1D code where now B_x is no longer constant.

7.1.5 Start-up and computational cycle

The start-up and computational cycle follow the 1D implementation, with the changes that we reported in the previous sections.

7.1.6 Fields calculations

In 1D all the derivatives along y and z directions are zero and to satisfy $\nabla \cdot \boldsymbol{B} = 0$, so the derivative of the magnetic field along x has to vanish, i.e., $B_x = const$ in all the domain. Since the temporal evolution of the magnetic field depends on the curl of the electric field the x component is also constant in time. Here the derivative along y direction is not zero any more, allowing the magnetic field to vary both in space and time in all the directions. However, it can be easily verified that if $\nabla \cdot \boldsymbol{B} = 0$ at $t = 0$ the solution of Faraday's and Ampère's equations imposes that the divergence of $\boldsymbol{B}$ remains zero, because of the use of the staggered $\boldsymbol{E}$ and $\boldsymbol{B}$ grid.

The electric and magnetic fields are still computed and advanced respectively using Eqs. (7.2 to 7.4) where now also the derivatives along y are included.

7.1.7 The collisional operator

Again, the collisional operator is the same used in the 1D3V version of our code. In particular we have that the collisional operator C for the coefficient l, m, n where P, Q, R are the total number of harmonics in the 3 directions, is:

$$C[C_{l,m,n}] - \nu \left[\frac{l(l-1)(l-2)}{(P-1)(P-2)(P-3)} + \frac{m(m-1)(m-2)}{(Q-1)(Q-2)(Q-3)} + \frac{n(n-1)(n-2)}{(R-1)(R-2)(R-3)} \right] C_{l,m,n} \quad (7.25)$$

we add this to the equations for the coefficients, as an explicit term on the RHS. As we split the distribution function advancement in two parts, we add half of the operator both in the space and velocity advancement.

7.2 Code implementation

The code implementation follows the same scheme as the 1D3V case. The only difference is the parallelization. In this section we will first briefly describe domain decomposition, then we will show how the parallelization is implemented and finally we will give some information about the *PETSc* library that we used for the parallel communication. *PETSc* is based on *MPI* the parallel *Message Passing Interface* library.

7.2.1 Domain decomposition

Domain decomposition is responsible for the subdivision of the grid in a number of nonoverlapping subdomains specified by the user by command line parameter. The number of subdomains in each direction has to be specified in the program input file. The number of processor in the x direction times the number of processors in the y direction has to be equal to the total number of processors parsed by the command line, which launches the parallel *MPI* job.

The actual domain subdivision works in the following way:

- the input file is read by each processor; each processor knows the total number of cells in each direction, the number of processors in each direction and the cell size;
- each processor, depending on its rank (i.e. the processor number), computes the number of points in each direction in its nonoverlapping subdomain and the coordinates of its delimiting points $(x_{min}, y_{min}), (x_{max}, y_{max})$;
- each processor adds a stencil of 1 overlapping nodes, i.e. ghost points, for each side of its subdomain. These points will contain the values of fields, momenta, coefficients of the distribution function of the neighbouring grid points lying on the neighbouring processors, which are used to compute derivatives and need to be updated with parallel communication each time they are updated on the single processors;
- memory for all the variables is locally allocated on each processor.

In Fig 7.2 we show a schematic domain decomposition of a 2D grid in four nonoverlapping subdomains, where ghost points have been added in red. In our code the subdomain in the bottom-left is assigned to the processor with $rank = 0$, the next subdomain on the right is assigned to the processor with $rank = 1$, growing until

reaching the subdomain on the left border of the domain which is assigned to the processor with $rank = N_{proc,x} - 1$, where $N_{proc,x}$ is the number of processors in the x direction. The processor with $rank = N_{proc,x}$ manages the subdomain on the left of second row starting from the bottom and so on until reaching the subdomain on the top right which is assigned to the processor with $rank = N_{proc,x} * N_{proc,y} - 1$.

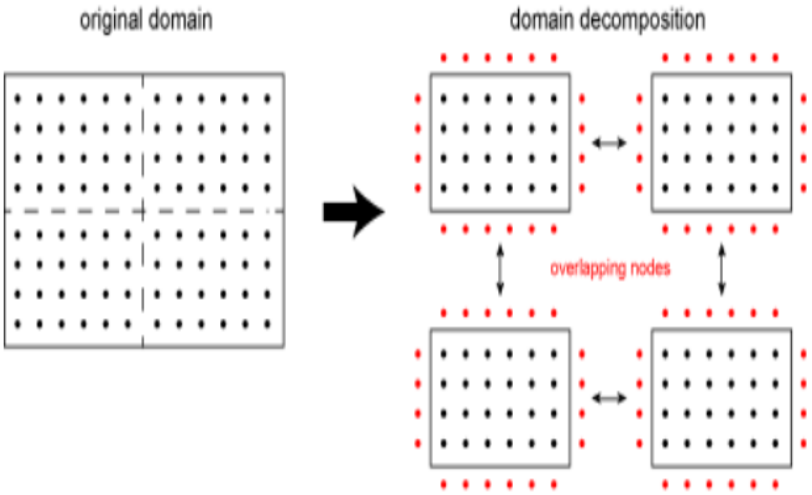

Figure 7.2: Simple 2D domain decomposition among four processors. Ghost points (overlapping nodes) are marked in red, actual points in black. Source: *http://www.k-wave.org/sc15.php*

7.2.2 Parallelization

As described in the previous paragraph, the rectangular grid is subdivided into small subdomains and each of them is assigned to a processor. The number of the latters in each direction is defined by the user and set in the *kvf* program input file. In each processor space is allocated for all the quantities for the actual grid points plus a single element stencil of ghost points. The *communication* class encapsulates *PETSc* library and makes use of the 2D *PETSc* object to exchange the informations concerning the ghost points. Three instances of the *communication* class are created:

- one for the fields and it has 3 degrees of freedom for the three directions of the fields. It can be used to communicate both electric and magnetic fields, one at a time;

- one for the moments and it has 7 degrees of freedom to communicate all the quantities stored in the class *QMoments*;

- one for the coefficients of the distribution function and it has $nvx * nvy * nvz$ degrees of freedom where the latters are the number of Hermite functions in each direction.

PETSc functions take care also of imposing boundary conditions and the communication is performed every time a boundary condition should be set. The class has a simple public interface which allows the user to initialize the relative object with desired parameters (in particular the number of degrees of freedom) and to perform parallel communication and update of ghost elements through the call to a single function which accepts as input a pointer to the local data and after the parallel communication updates the ghost elements in the local data.

The remaining part of the code is the same as in the sequential case, but each process solves the problem on a sub-domain as previously stated.

7.2.3 PETSc library

PETSc , *Portable, Extensible Toolkit for Scientific Computation* is a suite of data structures and routines that provide the building blocks for the implementation of large scale application codes on parallel (and serial) computers. The information reported here is taken from Balay et al. [2018]. See it for additional guidelines. It is a hierarchically organized library, which, by using object-oriented programming, enables users to employ the level of abstraction that is most appropriate for a particular problem, providing enormous flexibility. *PETSc* uses *MPI* standard for all message-passing communication. The library contains modules to deal with:

- index sets (IS), including permutations, for indexing into vectors, renumbering, etc;
- vectors (Vec);
- matrices (Mat) (generally sparse);
- managing interactions between mesh data structures and vectors and matrices (DM);
- over fifteen Krylov subspace methods (KSP);
- dozens of preconditioners, including multi-grid, block solvers, and sparse direct solvers (PC);
- nonlinear solvers (SNES);

- time steppers for solving time-dependent (nonlinear) PDEs, including support for differential algebraic equations (TS).

PETSc is designed to allow the user to solve PDEs on parallel computers using an uniform approach to each problem. It is interesting to consider the relations between the different libraries in Fig.(7.2.3).

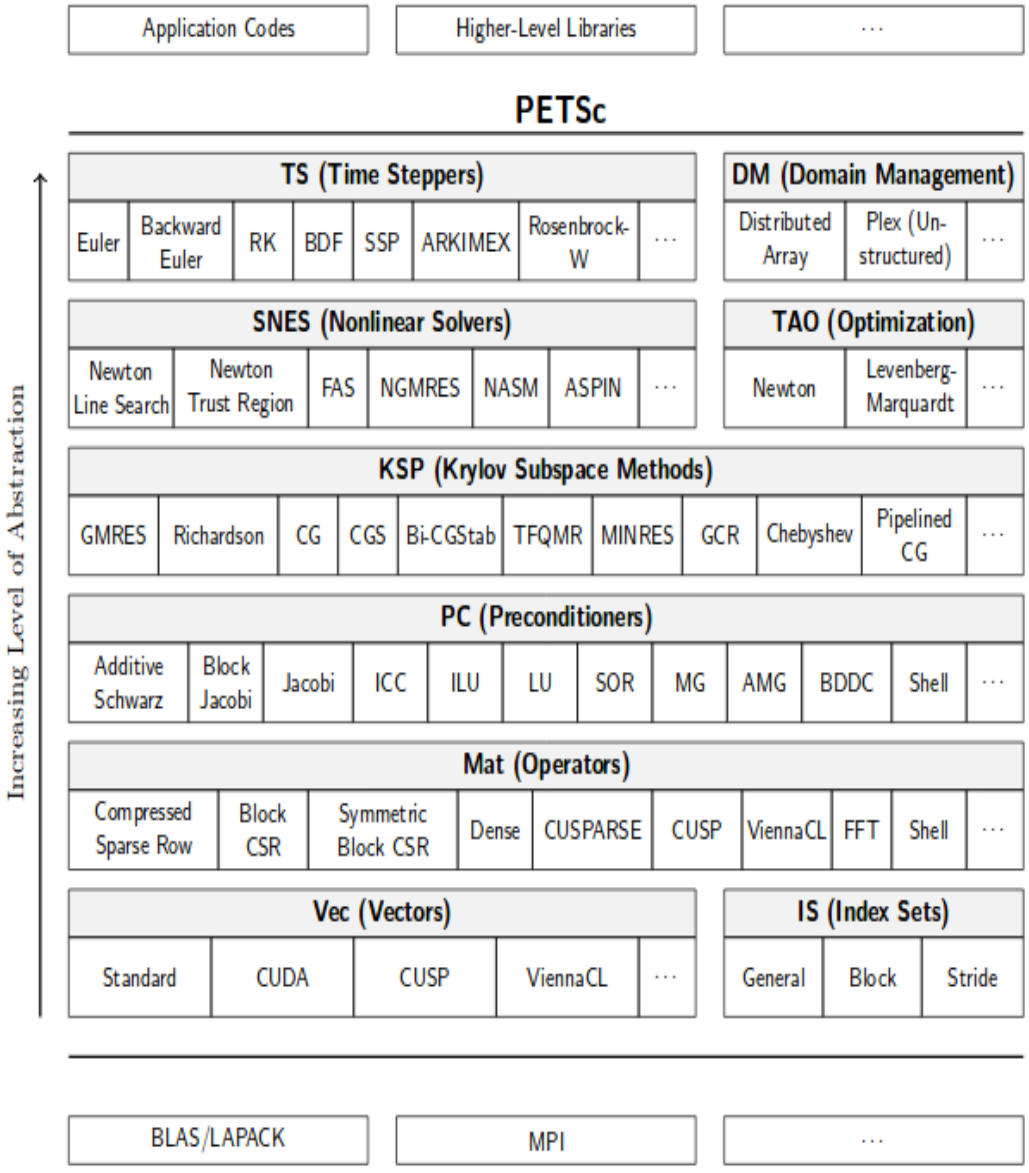

Figure 7.3: Relations among the different *PETSc* libraries. On top we can find the ones with higher level of abstraction, which then decreases going down the page.

In our 2D Hermite Vlasov-Hybrid code we encapsulate *PETSc* in the class *communication*. The latter makes use of 2D distributed arrays of DM class to perform

the parallel communication.

7.3 A quiet Maxwellian test

In this section we present a test that we performed on the implementation of the 2D3V Hermite-Vlasov-hybrid algorithm. We run the same test with the different schemes for the Λ_x advancement and the only one which did not diverge was the Lax-Friedrichs. However this scheme introduced numerical dissipation which damped the perturbations in the magnetic field away.

We carried out a simulation on a 160×160 cells grid, with $\Delta_x = \Delta_y = 0.5d_i$, setting the initial conditions to an isotropic quiet Maxwellian with $\beta = 0.1$. We chose the Hermite parameters $\alpha_{x,y,z} = 0.25$ and approximated the distribution function with a summation over 8 Hermite functions in each direction. In order to respect $\nabla\cdot\boldsymbol{B} = 0$ we imposed $\nabla\cdot\boldsymbol{B}^{t_0} = 0$. If this is satisfied resolving Faraday's and Ampère's laws implies that the divergence of the magnetic field is kept null at any time in the simulation. We achieved this by randomly perturbing only the z component of the magnetic field and leaving B_x and B_y constant. However this perturbation yields perturbations in the other components as well right after the first time step, in a manner to maintain $\nabla\cdot\boldsymbol{B} = 0$. We run the simulation for 5000 time steps of $0.01\Omega_i^{-1}$.

In Fig. 7.4 we show the magnetic field in the y direction at the beginning of the simulation, after one time step, in the top-left panel and after 1000 time steps in the top-right panel. In the bottom-left panel we take a slice of the domain imposing $y = const$ and we plot the temporal evolution of B_y in a (x,t) graph. In the bottom-right panel we show the dispersion relation in the x direction. At $t = 0.01\Omega_i^{-1}$ the perturbations in B_y are generated as expected. After 1000 time steps we see the perturbation damped and the peaks are reduced to half of the value at the beginning of the simulation. The damping become even more visible from the two bottom panels. In the left one we can see that at the end of the simulation the oscillations become negligible if compared to the initial ones. In the dispersion relation we can see that the left hand circularly polarized wave dispersion is absent. The latter is in fact more damped by nature than the right hand circularly polarized wave and the simulation is not able to capture it. Also, the right hand wave is damped for increasing values of k.

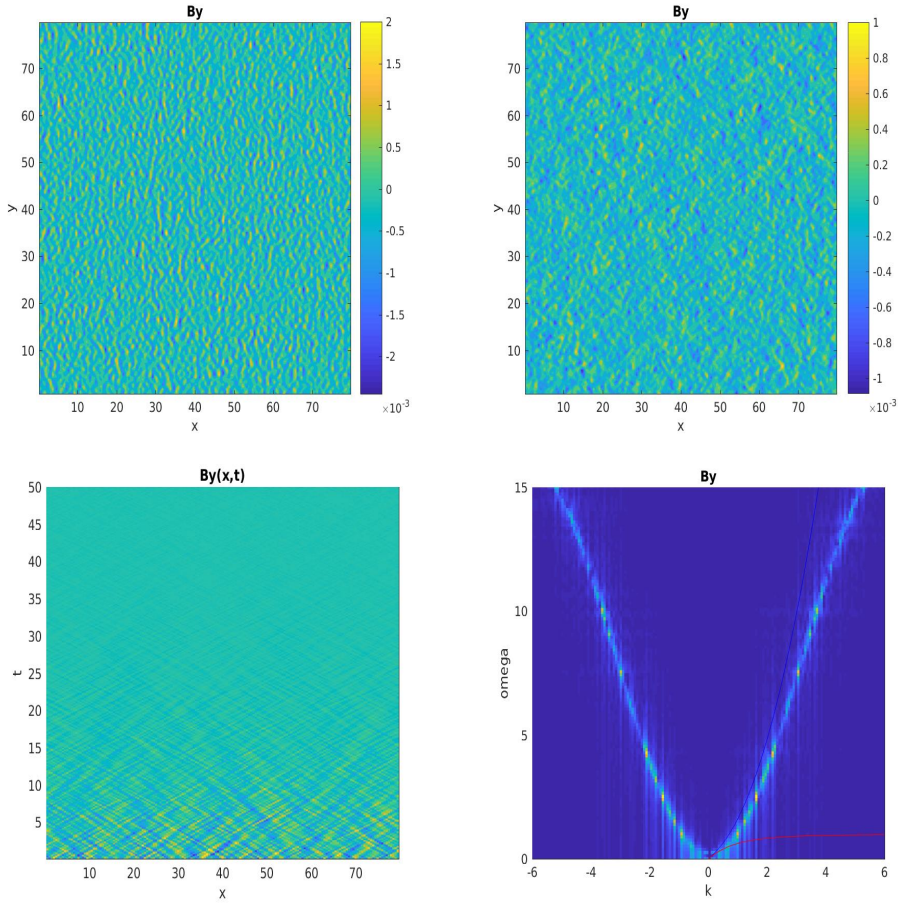

Figure 7.4: B_y after the first time step (top-left panel); B_y after 1000 time steps (top-right panel); $B_y(x,t)$ at constant y (bottom-right panel); dispersion relation of B_y along k_x (bottom-right panel).

Summary

We have described a 2D implementation of the Hermite-Vlasov-hybrid code. We have had mixed results. Using the Lax-Friedrichs scheme we have simulated the evolution of a quiet Maxwellian we uniform random perturbations in the magnetic field perpendicular to the simulation box. We obtained a wave dispersion for the right hand circularly polarized mode which partially agrees with the theoretical expectations.

However, the fluctuations are damped, presumably due to our choice of the numerical scheme, being too dissipative. Further work is required to provide a more accurate, less dissipative, stable scheme.

8 Conclusions and further work

In this work we have described the development of a new hybrid algorithm for the study of low growth rate instabilities. Due to the sensitivity to the initial noise of these type of instabilities we implemented a Vlasov-hybrid code which has zero intrinsic initial noise. To reduce the computational time we reduced the discretization points in velocity space by an expansion of the distribution function using the Hermite basis.

In the Introduction and the following two chapters we gave information about the solar wind, about the theoretical and numerical plasma models, about the study of turbulence problems using hybrid codes and about existing PIC-hybrid algorithms. Making use of these we developed a suite of codes that we used to compare the different time advancement algorithms. We decided that the *Current Advance Method* is the one performing best if we consider computational time and accuracy together.

In Chapter 4 we used the *Current Advance Method* to implement a 1D3V Hermite-Vlasov-hybrid code using the *C++* programming language. We validated our code performing a set of tests and comparing them with the results obtained with a linear solver. In particular we first used a quiet Maxwellian initial condition, adding random perturbations in a constant magnetic field. We followed the evolution of the magnetic field and plotted the dispersion relation. The result was in perfect agreement with the linear solver. Then we simulated a set of parallel propagating Alfvén waves both left hand and right hand circularly polarized, varying the wavelengths between 2 and 100 ion inertial lengths. For each wave we computed the ω calculating graphically the wave phase velocity and multiplying it by k. We compared the results with the ones obtained with the linear solver, finding excellent agreement for all the range of wavelengths.

In Chapter 5 we performed a ion temperature anisotropy instability simulation study. We observed the growth of a mode with wave number equal to the one expected from theory. We computed the linear growth rate and we found an error respect to theoretical prediction of 0.5%. We performed a parametric study, varying the parameters of the Hermite expansion and we observed that the method is very sensitive to the choice of those. We then compared the results to PIC-hybrid simula-

tions. We varied the number of particles per cell between the small number of 100 to the large value of 1000000, which had a high computational cost, reaching an error of $\approx 14\%$. This number of particles would not be possible in a multi dimensional simulation.

In Chapter 6 we simulated two ion/ion right hand resonant instabilities with small and medium growth rates. Again we compared with the results from linear solver and from PIC simulations. The Vlasov-hybrid code was capable to capture the mode with maximum linear growth rate, while in the PIC-hybrid simulations we observed the development of a superposition of waves with small and large wavelengths. For the simulation with small expected growth rate the our code performed better than the PIC-hybrid with errors of 3.6% and 19.5% respectively. Conversely in the simulation with medium growth rate the PIC-hybrid performed better with an error of 5.2% against the value of 11.5% obtained with our code. The PIC-hybrid code was capable of capturing the saturation phase of the instability while in our code this phase is not reached and the instability keeps growing. We believe that this is due to the shift and relaxation of the velocity distribution functions of the two populations which makes the initial Hermite parameters inadequate to describe the true distribution function itself.

In Chapter 7 we implemented a 2D3V version of the code. We described its parallelization using the *PETSc* library. While in the 1D3V we were able to overcome the mesh drifting instability using a Lax-Wendroff scheme for the Λ_{xy} advancement, here this method was not able to stop the growth of the numerical instability. We implemented two versions of the Lax-Wendroff scheme and in both cases we observed the numerical instability growing. We implemented a 4^{th} order Runge-Kutta time advancement scheme for the Λ_{xy} operator but this did not eliminate the instability. We then implemented a simple Lax-Friedrichs scheme. This method was able to stop the mesh drifting instability. However, we observed a significant damping in the magnetic field perturbations. We were not able to capture the dispersion of the left hand circularly polarized mode which is already damped by nature. However we had a proof of concept of the method.

In the future we are considering to implement an adaptive scheme which will be able to change the Hermite parameters following variations in the distribution function to be capable of simulating more complex problems. In order to achieve this it is necessary to first define a criterion to decide whether the Hermite parameters used at certain time are valid or not. If they are not valid a change of basis will have to be performed, which will change the values of all the coefficients of the distribution function. Then the new optimal parameters will be computed and set

in place of the old ones.

Also, a priority is to solve the mesh drifting instability problem. One way would be to employ a semi implicit scheme. Fully implicit methods are not recommended here due to the coupling between the cells. In fact for every cell we are updating 1000 Hermite coefficient every time step. Since the Λ_{xy} operator contains spatial derivatives, therefore making each cell coupled to all the others, we would need to invert huge matrices, particularly when we want to perform multidimensional simulations. Another way would be to solve this operator using a high order flux conserving finite volume method.

References

O. Alexandrova, J. Saur, C. Lacombe, A. Mangeney, J. Mitchell, S. J. Schwartz, and P. Robert. Universality of solar-wind turbulent spectrum from mhd to electron scales. *Phys. Rev. Lett.*, 103:165003, Oct 2009. doi: 10.1103/PhysRevLett.103.165003. URL https://link.aps.org/doi/10.1103/PhysRevLett.103.165003.

Akio Arakawa and Vivian R. Lamb. A potential enstrophy and energy conserving scheme for the shallow water equations. 109, 02 1981.

Satish Balay, Shrirang Abhyankar, Mark F. Adams, Jed Brown, Peter Brune, Kris Buschelman, Lisandro Dalcin, Victor Eijkhout, William D. Gropp, Dinesh Kaushik, Matthew G. Knepley, Dave A. May, Lois Curfman McInnes, Richard Tran Mills, Todd Munson, Karl Rupp, Patrick Sanan, Barry F. Smith, Stefano Zampini, Hong Zhang, and Hong Zhang. PETSc users manual. Technical Report ANL-95/11 - Revision 3.9, Argonne National Laboratory, 2018. URL http://www.mcs.anl.gov/petsc.

S. D. Bale, J. C. Kasper, G. G. Howes, E. Quataert, C. Salem, and D. Sundkvist. Magnetic fluctuation power near proton temperature anisotropy instability thresholds in the solar wind. *Phys. Rev. Lett.*, 103:211101, Nov 2009. doi: 10.1103/PhysRevLett.103.211101. URL https://link.aps.org/doi/10.1103/PhysRevLett.103.211101.

S. J. Bame, J. R. Asbridge, W. C. Feldman, S. Peter Gary, and Michael D. Montgomery. Evidence for local ion heating in solar wind high speed streams. *Geophysical Research Letters*, 2(9):373–375, 1975. doi: 10.1029/GL002i009p00373. URL https://agupubs.onlinelibrary.wiley.com/doi/abs/10.1029/GL002i009p00373.

S. J. Bame, D. J. McComas, B. L. Barraclough, J. L. Phillips, K. J. Sofaly, J. C. Chavez, B. E. Goldstein, and R. K. Sakurai. The ULYSSES solar wind plasma experiment. , 92:237–265, January 1992.

R. Barrett, M. Berry, T. Chan, J. Demmel, J. Donato, J. Dongarra, V. Eijkhout, R. Pozo, C. Romine, and H. van der Vorst. *Templates for the Solution of Linear Systems: Building Blocks for Iterative Methods*. Society for Industrial and Applied Mathematics, 1994. doi: 10.1137/1.9781611971538. URL http://epubs.siam.org/doi/abs/10.1137/1.9781611971538.

K. W. Behannon and N. F. Ness. Magnetic storms in the earth's magnetic tail. *Journal of Geophysical Research*, 71(9):2327–2351, 1966. ISSN 2156-2202. doi: 10.1029/JZ071i009p02327. URL http://dx.doi.org/10.1029/JZ071i009p02327.

L. Biermann. Kometenschweife und solare Korpuskularstrahlung. , 29:274, 1951.

C.K. Birdsall and A.B. Langdon. *Plasma Physics via Computer Simulation*. Series in Plasma Physics and Fluid Dynamics. Taylor & Francis, 2004. ISBN 9780750310253. URL https://books.google.co.uk/books?id=S2lqgDTm6a4C.

Stanislav Boldyrev and Jean Carlos Perez. Spectrum of kinetic-alfvn turbulence. *The Astrophysical Journal Letters*, 758(2):L44, 2012. URL http://stacks.iop.org/2041-8205/758/i=2/a=L44.

Jay P Boris and David L Book. Flux-corrected transport. i. shasta, a fluid transport algorithm that works. *Journal of Computational Physics*, 11(1):38 – 69, 1973. ISSN 0021-9991. doi: https://doi.org/10.1016/0021-9991(73)90147-2. URL http://www.sciencedirect.com/science/article/pii/0021999173901472.

J.P. Boris, R.A. Shanny, United States. Office of Naval Research, and Naval Research Laboratory. *Proceedings: Fourth Conference on Numerical Simulation of Plasmas, November 2, 3, 1970*. Naval Research Laboratory, 1970. URL https://books.google.co.uk/books?id=zqxSAQAACAAJ.

R. Bruno and L. Trenchi. Radial Dependence of the Frequency Break between Fluid and Kinetic Scales in the Solar Wind Fluctuations. , 787:L24, June 2014. doi: 10.1088/2041-8205/787/2/L24.

Roberto Bruno and Vincenzo Carbone. The solar wind as a turbulence laboratory. *Living Reviews in Solar Physics*, 10(1):2, May 2013. ISSN 1614-4961. doi: 10.12942/lrsp-2013-2. URL https://doi.org/10.12942/lrsp-2013-2.

Huishan Cai and Ding Li. Magnetic reconnection with pressure tensor in electron magnetohydrodynamics. *Physics of Plasmas*, 16(5):052107, 2009. doi: 10.1063/1.3122050. URL https://doi.org/10.1063/1.3122050.

E. Camporeale and D. Burgess. Comparison of linear modes in kinetic plasma models. *J. Plasma Phys.*, 83(2):535830201, April 2017. doi: 10.1017/S0022377817000277.

E. Camporeale, G. L. Delzanno, B. K. Bergen, and J. D. Moulton. On the velocity space discretization for the Vlasov-Poisson system: comparison between Hermite spectral and Particle-in-Cell methods. Part 1: semi-implicit scheme. *ArXiv e-prints*, November 2013a.

E. Camporeale, G. L. Delzanno, B. K. Bergen, and J. D. Moulton. On the velocity space discretization for the Vlasov-Poisson system: comparison between Hermite spectral and Particle-in-Cell methods. Part 2: fully-implicit scheme. *ArXiv e-prints*, December 2013b.

E. Camporeale, G. L. Delzanno, B. K. Bergen, and J. D. Moulton. On the velocity space discretization for the Vlasov-Poisson system: Comparison between implicit Hermite spectral and Particle-in-Cell methods. *Computer Physics Communications*, 198:47–58, January 2016. doi: 10.1016/j.cpc.2015.09.002.

J. A. Carrillo and F. Vecil. Nonoscillatory interpolation methods applied to vlasov-based models. *SIAM Journal on Scientific Computing*, 29(3):1179–1206, 2007. doi: 10.1137/050644549. URL https://doi.org/10.1137/050644549.

S. S. Cerri, S. Servidio, and F. Califano. Kinetic Cascade in Solar-wind Turbulence: 3D3V Hybrid-kinetic Simulations with Electron Inertia. *ApJ. Lett.*, 846: L18, September 2017. doi: 10.3847/2041-8213/aa87b0.

S. S. Cerri, M. W. Kunz, and F. Califano. Dual Phase-space Cascades in 3D Hybrid-VlasovMaxwell Turbulence. , 856:L13, March 2018. doi: 10.3847/2041-8213/aab557.

S.S. Cerri, L. Franci, F. Califano, S. Landi, and P. Hellinger. Plasma turbulence at ion scales: a comparison between particle in cell and eulerian hybrid-kinetic approaches. *Journal of Plasma Physics*, 83(2):705830202, 2017. doi: 10.1017/S0022377817000265.

S. Chandrasekhar. The stability of the pinch. *Proceedings of the Royal Society of London A: Mathematical, Physical and Engineering Sciences*, 245(1243):435–455, 1958. ISSN 0080-4630. doi: 10.1098/rspa.1958.0094. URL http://rspa.royalsocietypublishing.org/content/245/1243/435.

C. H. K. Chen, L. Leung, S. Boldyrev, B. A. Maruca, and S. D. Bale. Ionscale spectral break of solar wind turbulence at high and low beta. *Geophysical Research Letters*, 41(22):8081–8088, 2014. doi: 10.1002/2014GL062009. URL https://agupubs.onlinelibrary.wiley.com/doi/abs/10.1002/2014GL062009.

C. Z. Cheng and G. Knorr. The integration of the Vlasov equation in configuration space. *Journal of Computational Physics*, 22:330–351, November 1976. doi: 10.1016/0021-9991(76)90053-X.

Jianhua Cheng, Scott E. Parker, Y Chen, and Dmitri A. Uzdensky. A second-order semi-implicit f method for hybrid simulation. 245:364375, 07 2013.

Yingda Cheng, Andrew J. Christlieb, and Xinghui Zhong. Energy-conserving discontinuous galerkin methods for the vlasov-maxwell system. *J. Comput. Phys.*, 279(C):145–173, December 2014. ISSN 0021-9991. doi: 10.1016/j.jcp.2014.08.041. URL http://dx.doi.org/10.1016/j.jcp.2014.08.041.

P. J. Coleman, C. P. Sonett, D. L. Judge, and E. J. Smith. Some preliminary results of the pioneer v magnetometer experiment. *Journal of Geophysical Research*, 65(6):1856–1857. doi: 10.1029/JZ065i006p01856. URL https://agupubs.onlinelibrary.wiley.com/doi/abs/10.1029/JZ065i006p01856.

P. J. Coleman, Leverett Davis, and C. P. Sonett. Steady component of the interplanetary magnetic field: Pioneer v. *Phys. Rev. Lett.*, 5:43–46, Jul 1960. doi: 10.1103/PhysRevLett.5.43. URL https://link.aps.org/doi/10.1103/PhysRevLett.5.43.

P. J. Coleman, Jr. Turbulence, Viscosity, and Dissipation in the Solar-Wind Plasma. , 153:371, August 1968. doi: 10.1086/149674.

William Daughton, S. Peter Gary, and Dan Winske. Electromagnetic proton/proton instabilities in the solar wind: Simulations. *Journal of Geophysical Research: Space Physics*, 104(A3):4657–4667, 1999. doi: 10.1029/1998JA900105. URL https://agupubs.onlinelibrary.wiley.com/doi/abs/10.1029/1998JA900105.

G. L. Delzanno. Multi-dimensional, fully-implicit, spectral method for the Vlasov-Maxwell equations with exact conservation laws in discrete form. *Journal of Computational Physics*, 301:338–356, November 2015. doi: 10.1016/j.jcp.2015.07.028.

W. C. Feldman, J. R. Asbridge, S. J. Bame, and M. D. Montgomery. Double ion streams in the solar wind. *Journal of Geophysical Research*, 78(13):2017–2027, 1973. doi: 10.1029/JA078i013p02017. URL https://agupubs.onlinelibrary.wiley.com/doi/abs/10.1029/JA078i013p02017.

W. C. Feldman, J. R. Asbridge, S. J. Bame, and M. D. Montgomery. Interpenetrating solar wind streams. *Reviews of Geophysics*, 12(4):715–723, 1974. doi: 10.1029/RG012i004p00715. URL https://agupubs.onlinelibrary.wiley.com/doi/abs/10.1029/RG012i004p00715.

Francis Filbet, Eric Sonnendrcker, and Pierre Bertrand. Conservative numerical schemes for the vlasov equation. *Journal of Computational Physics*, 172(1):166 – 187, 2001. ISSN 0021-9991. doi: https://doi.org/10.1006/jcph.2001.6818. URL http://www.sciencedirect.com/science/article/pii/S0021999101968184.

V. Florinski, J. Heerikhuisen, J. Niemiec, and A. Ernst. The IBEX Ribbon and the Pickup Ion Ring Stability in the Outer Heliosheath. I. Theory and Hybrid Simulations. *ApJ.*, 826:197, August 2016. doi: 10.3847/0004-637X/826/2/197.

Luca Franci, Simone Landi, Lorenzo Matteini, Andrea Verdini, and Petr Hellinger. High-resolution hybrid simulations of kinetic plasma turbulence at proton scales. *The Astrophysical Journal*, 812(1):21, 2015a. URL http://stacks.iop.org/0004-637X/812/i=1/a=21.

Luca Franci, Andrea Verdini, Lorenzo Matteini, Simone Landi, and Petr Hellinger. Solar wind turbulence from mhd to sub-ion scales: High-resolution hybrid simulations. *The Astrophysical Journal Letters*, 804(2):L39, 2015b. URL http://stacks.iop.org/2041-8205/804/i=2/a=L39.

Luca Franci, Petr Hellinger, Lorenzo Matteini, Andrea Verdini, and Simone Landi. Two-dimensional hybrid simulations of kinetic plasma turbulence: Current and vorticity vs proton temperature. *AIP Conference Proceedings*, 1720(1):040003, 2016a. doi: 10.1063/1.4943814. URL https://aip.scitation.org/doi/abs/10.1063/1.4943814.

Luca Franci, Simone Landi, Lorenzo Matteini, Andrea Verdini, and Petr Hellinger. Plasma beta dependence of the ion-scale spectral break of solar wind turbulence: High-resolution 2d hybrid simulations. *The Astrophysical Journal*, 833 (1):91, 2016b. URL http://stacks.iop.org/0004-637X/833/i=1/a=91.

Luca Franci, Silvio Sergio Cerri, Francesco Califano, Simone Landi, Emanuele Papini, Andrea Verdini, Lorenzo Matteini, Frank Jenko, and Petr Hellinger. Magnetic reconnection as a driver for a sub-ion-scale cascade in plasma turbulence. *The Astrophysical Journal Letters*, 850(1):L16, 2017. URL http://stacks.iop.org/2041-8205/850/i=1/a=L16.

Luca Franci, Simone Landi, Andrea Verdini, Lorenzo Matteini, and Petr Hellinger. Solar wind turbulent cascade from mhd to sub-ion scales: Large-size 3d hybrid particle-in-cell simulations. *The Astrophysical Journal*, 853(1):26, 2018. URL http://stacks.iop.org/0004-637X/853/i=1/a=26.

A. Friedman, A.B. Langdon, and B.I. Cohen. A direct method for implicit particle-in-cell simulation. *Comments on Plasma Physics and Controlled Fusion*, 6:225 – 236, 1955.

M. Fujimoto. *Instabilities in the magnetopause velocity shear layer*. PhD thesis, University of Tokyo, 1991.

S. P. Gary. Electromagnetic ion/ion instabilities and their consequences in space plasmas - A review. , 56:373–415, May 1991. doi: 10.1007/BF00196632.

S. P. Gary. *Theory of Space Plasma Microinstabilities*. September 1993.

S. Peter Gary. The mirror and ion cyclotron anisotropy instabilities. *Journal of Geophysical Research: Space Physics*, 97(A6):8519–8529, 1992. doi: 10.1029/92JA00299. URL https://agupubs.onlinelibrary.wiley.com/doi/abs/10.1029/92JA00299.

S. Peter Gary, Hui Li, Sean O'Rourke, and Dan Winske. Proton resonant firehose instability: Temperature anisotropy and fluctuating field constraints. *Journal of Geophysical Research: Space Physics*, 103(A7):14567–14574. doi: 10.1029/98JA01174. URL https://agupubs.onlinelibrary.wiley.com/doi/abs/10.1029/98JA01174.

S. Peter Gary, M. D. Montgomery, W. C. Feldman, and D. W. Forslund. Proton temperature anisotropy instabilities in the solar wind. *Journal of Geophysical Research*, 81(7):1241–1246, 1976. doi: 10.1029/JA081i007p01241. URL https://agupubs.onlinelibrary.wiley.com/doi/abs/10.1029/JA081i007p01241.

S. Peter Gary, Charles W. Smith, Martin A. Lee, Melvyn L. Goldstein, and David W. Forslund. Electromagnetic ion beam instabilities. *The Physics of Fluids*, 27(7):1852–1862, 1984. doi: 10.1063/1.864797. URL https://aip.scitation.org/doi/abs/10.1063/1.864797.

S. Peter Gary, Christian D. Madland, and Bruce T. Tsurutani. Electromagnetic ion beam instabilities: Ii. *The Physics of Fluids*, 28(12):3691–3695, 1985. doi: 10.1063/1.865101. URL https://aip.scitation.org/doi/abs/10.1063/1.865101.

S. Peter Gary, Christian D. Madland, David Schriver, and Dan Winske. Computer simulations of electromagnetic cool ion beam instabilities. *Journal of Geophysical Research: Space Physics*, 91(A4):4188–4200, 1986. doi: 10.1029/JA091iA04p04188. URL https://agupubs.onlinelibrary.wiley.com/doi/abs/10.1029/JA091iA04p04188.

S. Peter Gary, Ruth M. Skoug, John T. Steinberg, and Charles W. Smith. Proton temperature anisotropy constraint in the solar wind: Ace observations. *Geophysical Research Letters*, 28(14):2759–2762, 2001. doi: 10.1029/2001GL013165. URL https://agupubs.onlinelibrary.wiley.com/doi/abs/10.1029/2001GL013165.

S. Peter Gary, Lan K. Jian, Thomas W. Broiles, Michael L. Stevens, John J. Podesta, and Justin C. Kasper. Iondriven instabilities in the solar wind: Wind observations of 19 march 2005. *Journal of Geophysical Research: Space Physics*, 121(1):30–41, 2015. doi: 10.1002/2015JA021935. URL https://agupubs.onlinelibrary.wiley.com/doi/abs/10.1002/2015JA021935.

G. Gnavi, L. Gomberoff, F. T. Gratton, and R. M. O. Galvo. Electromagnetic ion-beam instabilities in a cold plasma. *Journal of Plasma Physics*, 55(1):7786, 1996. doi: 10.1017/S0022377800018675.

Melvyn L. Goldstein, Charles W. Smith, and William H. Matthaeus. Large amplitude mhd waves upstream of the jovian bow shock. *Journal of Geophysical Research: Space Physics*, 88(A12):9989–9999, 1983. doi: 10.1029/JA088iA12p09989. URL https://agupubs.onlinelibrary.wiley.com/doi/abs/10.1029/JA088iA12p09989.

G. E. Hale. On the Probable Existence of a Magnetic Field in Sun-Spots. , 28:315, November 1908. doi: 10.1086/141602.

Francis H. Harlow. A machine calculation method for hydrodynamic problems. *Los Alamos Scientific Laboratory report*, LAMS-1956, 1955.

Francis H. Harlow. Pic and its progeny. *Computer Physics Communications*, 48(1):1 – 10, 1988. ISSN 0010-4655. doi: https://doi.org/10.1016/0010-4655(88)90017-3. URL http://www.sciencedirect.com/science/article/pii/0010465588900173.

D. S. Harned. Quasineutral hybrid simulation of macroscopic plasma phenomena. *Journal of Computational Physics*, 47:452–462, September 1982. doi: 10.1016/0021-9991(82)90094-8.

P. Hellinger and P. M. Trávníček. Oblique proton fire hose instability in the expanding solar wind: Hybrid simulations. *J. Geophys. Res.*, 113(A12):A10109, October 2008. doi: 10.1029/2008JA013416.

P. Hellinger, P. Trávníček, J. C. Kasper, and A. J. Lazarus. Solar wind proton temperature anisotropy: Linear theory and WIND/SWE observations. *Geophys. Res. Lett.*, 33:L09101, May 2006. doi: 10.1029/2006GL025925.

P. Hellinger, S. Landi, L. Matteini, A. Verdini, and L. Franci. Mirror Instability in the Turbulent Solar Wind. *ApJ.*, 838:158, April 2017. doi: 10.3847/1538-4357/aa67e0.

Petr Hellinger, Lorenzo Matteini, Simone Landi, Andrea Verdini, Luca Franci, and Pavel M. Trvnek. Plasma turbulence and kinetic instabilities at ion scales in the expanding solar wind. *The Astrophysical Journal Letters*, 811(2):L32, 2015. URL `http://stacks.iop.org/2041-8205/811/i=2/a=L32`.

M. Hesse, D. Winske, and M. M. Kuznetsova. Hybrid modeling of collisionless reconnection in two-dimensional current sheets: Simulations. *J. Geophys. Res.*, 100:21815–21826, November 1995. doi: 10.1029/95JA01559.

Michael Hesse and Dan Winske. Hybrid simulations of collisionless reconnection in current sheets. *Journal of Geophysical Research: Space Physics*, 99(A6):11177–11192, 1994. ISSN 2156-2202. doi: 10.1029/94JA00676. URL `http://dx.doi.org/10.1029/94JA00676`.

D.W Hewett and C.W Nielson. A multidimensional quasineutral plasma simulation model. *Journal of Computational Physics*, 29(2):219 – 236, 1978. ISSN 0021-9991. doi: https://doi.org/10.1016/0021-9991(78)90153-5. URL `http://www.sciencedirect.com/science/article/pii/0021999178901535`.

Samuel T. Jones and Scott E. Parker. Including electron inertia without advancing electron flow. *Journal of Computational Physics*, 191(1):322 – 327, 2003. ISSN 0021-9991. doi: https://doi.org/10.1016/S0021-9991(03)00305-X. URL `http://www.sciencedirect.com/science/article/pii/S002199910300305X`.

Justin C. Kasper, Alan J. Lazarus, and S. Peter Gary. Wind/swe observations of firehose constraint on solar wind proton temperature anisotropy. *Geophysical Research Letters*, 29(17):20–1–20–4, 2002. doi: 10.1029/2002GL015128. URL `https://agupubs.onlinelibrary.wiley.com/doi/abs/10.1029/2002GL015128`.

C.T. Kelley. *Iterative Methods for Linear and Nonlinear Equations*. SIAM, 1995. ISBN 9780898713527.

A. Kolmogorov. The Local Structure of Turbulence in Incompressible Viscous Fluid for Very Large Reynolds' Numbers. *Akademiia Nauk SSSR Doklady*, 30:301–305, 1941.

Robert H. Kraichnan. Inertialrange spectrum of hydromagnetic turbulence. *The Physics of Fluids*, 8(7):1385–1387, 1965. doi: 10.1063/1.1761412. URL https://aip.scitation.org/doi/abs/10.1063/1.1761412.

M. M. Kuznetsova, M. Hesse, and D. Winske. Kinetic quasi-viscous and bulk flow inertia effects in collisionless magnetotail reconnection. *J. Geophys. Res.*, 103: 199–214, January 1998. doi: 10.1029/97JA02699.

Giovanni Lapenta. Particle simulations of space weather. *Journal of Computational Physics*, 231(3):795 – 821, 2012. ISSN 0021-9991. doi: https://doi.org/10.1016/j.jcp.2011.03.035. URL http://www.sciencedirect.com/science/article/pii/S0021999111001860. Special Issue: Computational Plasma Physics.

A. S. Lipatov. Hybrid codes with finite electron mass. In J. Büchner, C. T. Dum, and M. Scholer, editors, *Space Plasma Simulation*, page 66, 2001.

A. Mangeney, F. Califano, C. Cavazzoni, and P. Travnicek. A Numerical Scheme for the Integration of the Vlasov-Maxwell System of Equations. *Journal of Computational Physics*, 179:495–538, July 2002. doi: 10.1006/jcph.2002.7071.

S. Markidis, E. Camporeale, D. Burgess, Rizwan-Uddin, and G. Lapenta. Parsek2D: An Implicit Parallel Particle-in-Cell Code. In N. V. Pogorelov, E. Audit, P. Colella, and G. P. Zank, editors, *Numerical Modeling of Space Plasma Flows: ASTRONUM-2008*, volume 406 of *Astronomical Society of the Pacific Conference Series*, page 237, April 2009.

E. Marsch, X.Z. Ao, and C.Y. Tu. On the temperature anisotropy of the core part of the proton velocity distribution function in the solar wind. *Journal of Geophysical Research: Space Physics*, 109(A4), 2004. doi: 10.1029/2003JA010330. URL https://agupubs.onlinelibrary.wiley.com/doi/abs/10.1029/2003JA010330.

R.G. Marsden and E.J. Smith. Ulysses: A summary of the first high-latitude survey. *Advances in Space Research*, 19(6):825 – 834, 1997. ISSN 0273-1177. doi: https://doi.org/10.1016/S0273-1177(97)00286-X. URL http://www.sciencedirect.com/science/article/pii/S027311779700286X. The Heliosphere at Solar Minimum and Beyond.

B.A. Maruca. *Instability-Driven Limits on Ion Temperature Anisotropy in the Solar Wind: Observations and Linear Vlasov Theory*. PhD thesis, Harvard University, 2012.

M. Matsumoto, Y. Kajimura, H. Usui, I. Funaki, and I. Shinohara. Application of a total variation diminishing scheme to electromagnetic hybrid particle-in-cell plasma simulation. *Computer Physics Communications*, 183:2027–2034, October 2012. doi: 10.1016/j.cpc.2012.04.021.

L. Matteini, P. Hellinger, S. Landi, P. M. Trávníček, and M. Velli. Ion Kinetics in the Solar Wind: Coupling Global Expansion to Local Microphysics. *Space Sci. Rev.*, 172:373–396, November 2012. doi: 10.1007/s11214-011-9774-z.

L. Matteini, S. Landi, M. Velli, and W. H. Matthaeus. Proton temperature anisotropy and magnetic reconnection in the solar wind: Effects of kinetic instabilities on current sheet stability. *The Astrophysical Journal*, 763(2):142, 2013. URL http://stacks.iop.org/0004-637X/763/i=2/a=142.

Alan P. Matthews. Current advance method and cyclic leapfrog for 2d multispecies hybrid plasma simulations. *Journal of Computational Physics*, 112(1):102 – 116, 1994. ISSN 0021-9991. doi: https://doi.org/10.1006/jcph.1994.1084. URL http://www.sciencedirect.com/science/article/pii/S0021999184710849.

D. J. McComas, S. J. Bame, P. Barker, W. C. Feldman, J. L. Phillips, P. Riley, and J. W. Griffee. *Solar Wind Electron Proton Alpha Monitor (SWEPAM) for the Advanced Composition Explorer*, pages 563–612. Springer Netherlands, Dordrecht, 1998. ISBN 978-94-011-4762-0. doi: 10.1007/978-94-011-4762-0_20. URL https://doi.org/10.1007/978-94-011-4762-0_20.

David Mccomas, R Goldstein, John Gosling, and R M. Skoug. Ulysses' second orbit: Remarkably different solar wind. 97:99–103, 05 2001.

M. E. McKean, D. Winske, and S. P. Gary. Two-dimensional simulations of ion anisotropy instabilities in the magnetosheath. *J. Geophys. Res.*, 99:11141–11154, June 1994. doi: 10.1029/93JA03025.

J. D. Mihalov, D. S. Colburn, R. G. Currie, and C. P. Sonett. Configuration and reconnection of the geomagnetic tail. *Journal of Geophysical Research*, 73(3): 943–959, 1968. ISSN 2156-2202. doi: 10.1029/JA073i003p00943. URL http://dx.doi.org/10.1029/JA073i003p00943.

P. A. Muñoz, N. Jain, P. Kilian, and J. Büchner. A new hybrid code (CHIEF) implementing the inertial electron fluid equation without approximation. *ArXiv e-prints*, December 2017.

Norman F. Ness. The earth's magnetic tail. *Journal of Geophysical Research*, 70 (13):2989–3005, 1965. ISSN 2156-2202. doi: 10.1029/JZ070i013p02989. URL http://dx.doi.org/10.1029/JZ070i013p02989.

Norman F. Ness. The geomagnetic tail. *Reviews of Geophysics*, 7(1-2):97–127, 1969. ISSN 1944-9208. doi: 10.1029/RG007i001p00097. URL http://dx.doi.org/10.1029/RG007i001p00097.

Norman F. Ness and Leonard F. Burlaga. Spacecraft studies of the interplanetary magnetic field. *Journal of Geophysical Research: Space Physics*, 106 (A8):15803–15817, 2001. doi: 10.1029/2000JA000118. URL https://agupubs.onlinelibrary.wiley.com/doi/abs/10.1029/2000JA000118.

E. N. Parker. Dynamics of the Interplanetary Gas and Magnetic Fields. , 128:664, November 1958. doi: 10.1086/146579.

Joseph T. Parker and Paul J. Dellar. Fourierhermite spectral representation for the vlasovpoisson system in the weakly collisional limit. *Journal of Plasma Physics*, 81(2):305810203, 2015. doi: 10.1017/S0022377814001287.

G. Parks. *Physics Of Space Plasmas: An Introduction, Second Edition*. Avalon Publishing, 2003. ISBN 9780813341309. URL `https://books.google.co.uk/books?id=yY8rvgAACAAJ`.

T. Passot and P.L. Sulem. A Landau fluid model for dispersive magnetohydrodynamics. *Physics of Plasmas*, 11:5173–5189, 2004.

F. W. Perkins. Ionstreaming instabilities: Electromagnetic and electrostatic. *The Physics of Fluids*, 19(7):1012–1020, 1976. doi: 10.1063/1.861597. URL `https://aip.scitation.org/doi/abs/10.1063/1.861597`.

J. J. Podesta, D. A. Roberts, and M. L. Goldstein. Spectral Exponents of Kinetic and Magnetic Energy Spectra in Solar Wind Turbulence. , 664:543–548, July 2007. doi: 10.1086/519211.

John J. Podesta. The need to consider ion bernstein waves as a dissipation channel of solar wind turbulence. *Journal of Geophysical Research: Space Physics*, 117(A7), 2012. doi: 10.1029/2012JA017770. URL `https://agupubs.onlinelibrary.wiley.com/doi/abs/10.1029/2012JA017770`.

Nikolai V. Pogorelov, Edouard Audit, Phillip Colella, Gary Zank, Stefanos Markidis, E. Camporeale, David Burgess, and Gry Hasselbalch Lapenta. Parsek2d: An implicit parallel particle-in-cell code. 2009.

William H. Press, Saul A. Teukolsky, William T. Vetterling, and Brian P. Flannery. *Numerical Recipes in C (2Nd Ed.): The Art of Scientific Computing*. Cambridge University Press, New York, NY, USA, 1992. ISBN 0-521-43108-5.

Jianxian Qiu. and Chi-Wang Shu. Runge–kutta discontinuous galerkin method using weno limiters. *SIAM Journal on Scientific Computing*, 26(3):907–929, 2005. doi: 10.1137/S1064827503425298. URL `https://doi.org/10.1137/S1064827503425298`.

Jing-Mei Qiu and Chi-Wang Shu. Positivity preserving semi-lagrangian discontinuous galerkin formulation: Theoretical analysis and application to the vlasovpoisson system. *J. Comput. Phys.*, 230(23):8386–8409, September 2011. ISSN 0021-9991. doi: 10.1016/j.jcp.2011.07.018. URL `http://dx.doi.org/10.1016/j.jcp.2011.07.018`.

M. A. Riquelme, E. Quataert, and D. Verscharen. Particle-in-cell Simulations of Continuously Driven Mirror and Ion Cyclotron Instabilities in High Beta Astrophysical and Heliospheric Plasmas. *ApJ.*, 800:27, February 2015. doi: 10.1088/0004-637X/800/1/27.

Y. Saad. *Iterative Methods for Sparse Linear Systems*. Society for Industrial and Applied Mathematics, second edition, 2003. doi: 10.1137/1.9780898718003. URL http://epubs.siam.org/doi/abs/10.1137/1.9780898718003.

F. Sahraoui, M. L. Goldstein, G. Belmont, P. Canu, and L. Rezeau. Three dimensional anisotropic k spectra of turbulence at subproton scales in the solar wind. *Phys. Rev. Lett.*, 105:131101, Sep 2010. doi: 10.1103/PhysRevLett.105.131101. URL https://link.aps.org/doi/10.1103/PhysRevLett.105.131101.

C. Salem, A. Mangeney, S. D. Bale, and P. Veltri. Solar Wind Magnetohydrodynamics Turbulence: Anomalous Scaling and Role of Intermittency. , 702:537–553, September 2009. doi: 10.1088/0004-637X/702/1/537.

A. A. Samsonov, M. I. Pudovkin, S. Peter Gary, and Daniel Hubert. Anisotropic mhd model of the dayside magnetosheath downstream of the oblique bow shock. *Journal of Geophysical Research: Space Physics*, 106(A10):21689–21699, 2001. doi: 10.1029/2000JA900150. URL https://agupubs.onlinelibrary.wiley.com/doi/abs/10.1029/2000JA900150.

Karl Schindler. *Physics of Space Plasma Activity*. Cambridge University Press, 2006. doi: 10.1017/CBO9780511618321.

S. J. Schwartz, D. Burgess, and J. J. Moses. Low-frequency waves in the Earthś magnetosheath: present status. *Annales Geophysicae*, 14:1134–1150, November 1996. doi: 10.1007/s00585-996-1134-z.

S. Servidio, F. Valentini, F. Califano, and P. Veltri. Local kinetic effects in two-dimensional plasma turbulence. *Phys. Rev. Lett.*, 108:045001, Jan 2012. doi: 10.1103/PhysRevLett.108.045001. URL https://link.aps.org/doi/10.1103/PhysRevLett.108.045001.

S. Servidio, K. T. Osman, F. Valentini, D. Perrone, F. Califano, S. Chapman, W. H. Matthaeus, and P. Veltri. Proton kinetic effects in vlasov and solar wind turbulence. *The Astrophysical Journal Letters*, 781(2):L27, 2014. URL http://stacks.iop.org/2041-8205/781/i=2/a=L27.

S. Servidio, F. Valentini, D. Perrone, A. Greco, F. Califano, W. H. Matthaeus, and P. Veltri. A kinetic model of plasma turbulence. *Journal of Plasma Physics*, 81 (1):325810107, 2015. doi: 10.1017/S0022377814000841.

Charles W. Smith, Melvyn L. Goldstein, S. Peter Gary, and C. T. Russell. Beam-driven ion cyclotron harmonic resonances in the terrestrial foreshock. *Journal of Geophysical Research: Space Physics*, 90(A2):1429–1434, 1985. doi: 10.1029/JA090iA02p01429. URL https://agupubs.onlinelibrary.wiley.com/doi/abs/10.1029/JA090iA02p01429.

Luca Sorriso-Valvo, Denise Perrone, Oreste Pezzi, Francesco Valentini, Sergio Servidio, Ioannis Zouganelis, and Pierluigi Veltri. Local energy transfer rate and

kinetic processes: the fate of turbulent energy in two-dimensional hybrid vlasov-maxwell numerical simulations. *Journal of Plasma Physics*, 84(2):725840201, 2018. doi: 10.1017/S0022377818000302.

Gilbert Strang. On the construction and comparison of difference schemes. *SIAM Journal on Numerical Analysis*, 5(3):506–517, 1968. doi: 10.1137/0705041. URL `https://doi.org/10.1137/0705041`.

D. W. Swift and Y. Lin. Substorm onset viewed by a two-dimensional, global-scale hybrid code. *Journal of Atmospheric and Solar-Terrestrial Physics*, 63:683–704, May 2001. doi: 10.1016/S1364-6826(00)00188-7.

Daniel W. Swift. Use of a hybrid code for global-scale plasma simulation. *Journal of Computational Physics*, 126(1):109 – 121, 1996. ISSN 0021-9991. doi: https://doi.org/10.1006/jcph.1996.0124. URL `http://www.sciencedirect.com/science/article/pii/S0021999196901242`.

Jeffrey A. Tessein, Charles W. Smith, Benjamin T. MacBride, William H. Matthaeus, Miriam A. Forman, and Joseph E. Borovsky. Spectral indices for multi-dimensional interplanetary turbulence at 1 au. *The Astrophysical Journal*, 692(1):684, 2009. URL `http://stacks.iop.org/0004-637X/692/i=1/a=684`.

Gábor Tóth. Computational mhd: Tutorial. University Tutorial, 2011.

Bruce Tsurutani. Results from ulysses' jupiter flyby. *Eos, Transactions American Geophysical Union*, 73(11):114–115, 1992. doi: 10.1029/91EO00087. URL `https://agupubs.onlinelibrary.wiley.com/doi/abs/10.1029/91EO00087`.

F. Valentini, P. Trvnek, F. Califano, P. Hellinger, and A. Mangeney. A hybrid-vlasov model based on the current advance method for the simulation of collisionless magnetized plasma. *Journal of Computational Physics*, 225(1):753 – 770, 2007. ISSN 0021-9991. doi: https://doi.org/10.1016/j.jcp.2007.01.001. URL `http://www.sciencedirect.com/science/article/pii/S0021999107000022`.

D. Verscharen and B. D. G. Chandran. The Dispersion Relations and Instability Thresholds of Oblique Plasma Modes in the Presence of an Ion Beam. , 764:88, February 2013. doi: 10.1088/0004-637X/764/1/88.

D. Winske and M. M. Leroy. Diffuse ions produced by electromagnetic ion beam instabilities. , 89:2673–2688, May 1984. doi: 10.1029/JA089iA05p02673.

D. Winske and N. Omidi. Electromagnetic ion/ion cyclotron instability: Theory and simulations. *Journal of Geophysical Research: Space Physics*, 97(A10):14779–14799, 1992. doi: 10.1029/92JA00902. URL `https://agupubs.onlinelibrary.wiley.com/doi/abs/10.1029/92JA00902`.

D. Winske and K. B. Quest. Electromagnetic ion beam instabilities: Comparison of one- and two-dimensional simulations. *J. Geophys. Res.*, 91(A8):8789–8797, 1986. ISSN 2156-2202. doi: 10.1029/JA091iA08p08789. URL `http://dx.doi.org/10.1029/JA091iA08p08789`.

Dan Winske, Lin Yin, Nick Omidi, Homa Karimabadi, and Kevin Quest. Hybrid simulation codes: Past, present and future—a tutorial. In Jörg Büchner, Manfred Scholer, and Christian T. Dum, editors, *Space Plasma Simulation*, pages 136–165, Berlin, Heidelberg, 2003. Springer Berlin Heidelberg. ISBN "978-3-540-36530-3". doi: "10.1007/3-540-36530-38". URL "https://doi.org/10.1007/3-540-36530-38".

H.C. Yee. *A Class of High Resolution Explicit and Implicit Shock-capturing Methods*. 1989. URL https://books.google.co.uk/books?id=-B82AQAAMAAJ.

L. Yin, D. Winske, S. P. Gary, and J. Birn. Hybrid and hall-mhd simulations of collisionless reconnection: Dynamics of the electron pressure tensor. *Journal of Geophysical Research: Space Physics*, 106(A6):10761–10775, 2001. ISSN 2156-2202. doi: 10.1029/2000JA000398. URL http://dx.doi.org/10.1029/2000JA000398.

Lin Yin and Dan Winske. Simulations of current sheet thinning and reconnection. *Journal of Geophysical Research: Space Physics*, 107(A12):SMP 39–1–SMP 39–11, 2002. ISSN 2156-2202. doi: 10.1029/2002JA009507. URL http://dx.doi.org/10.1029/2002JA009507. 1485.

J. S. Zhao, Y. Voitenko, M. Y. Yu, J. Y. Lu, and D. J. Wu. Properties of Short-wavelength Oblique Alfvén and Slow Waves. *ApJ.*, 793:107, October 2014. doi: 10.1088/0004-637X/793/2/107.